

# **Optimal Impact Isolation for Minimal Head Injury Criterion (HIC) Using Effective Operating Region (EOR)**

**by**

**Hossein Dehghani**

B. Sc., Amirkabir University of Technology, 2010

Thesis Submitted In Partial Fulfillment of the  
Requirements for the Degree of  
Master of Applied Science

in the

School of Engineering Science  
Faculty of Applied Sciences

**© Hossein Dehghani 2012**

**SIMON FRASER UNIVERSITY**

**Fall 2012**

All rights reserved.

However, in accordance with the *Copyright Act of Canada*, this work may be reproduced, without authorization, under the conditions for "Fair Dealing." Therefore, limited reproduction of this work for the purposes of private study, research, criticism, review and news reporting is likely to be in accordance with the law, particularly if cited appropriately.

# Approval

**Name:** Hossein Dehghani

**Degree:** Master of Applied Science

**Title of Thesis:** *Optimal Impact Isolation for Minimal Head Injury  
Criterion (HIC) Using Effective Operating Region (EOR)*

**Examining Committee:** **Chair:** Dr. Ahmad Rad  
Professor

**Dr. Siamak Arzanpour**  
Senior Supervisor  
Assistant Professor, P. Eng

---

**Dr. Gary Wang**  
Supervisor  
Professor

---

**Dr. Krishna Vijayaraghavan**  
Internal Examiner  
Assistant Professor

---

**Date Defended/Approved:** December 10, 2012

## Partial Copyright Licence



The author, whose copyright is declared on the title page of this work, has granted to Simon Fraser University the right to lend this thesis, project or extended essay to users of the Simon Fraser University Library, and to make partial or single copies only for such users or in response to a request from the library of any other university, or other educational institution, on its own behalf or for one of its users.

The author has further granted permission to Simon Fraser University to keep or make a digital copy for use in its circulating collection (currently available to the public at the "Institutional Repository" link of the SFU Library website ([www.lib.sfu.ca](http://www.lib.sfu.ca)) at <http://summit.sfu.ca> and, without changing the content, to translate the thesis/project or extended essays, if technically possible, to any medium or format for the purpose of preservation of the digital work.

The author has further agreed that permission for multiple copying of this work for scholarly purposes may be granted by either the author or the Dean of Graduate Studies.

It is understood that copying or publication of this work for financial gain shall not be allowed without the author's written permission.

Permission for public performance, or limited permission for private scholarly use, of any multimedia materials forming part of this work, may have been granted by the author. This information may be found on the separately catalogued multimedia material and in the signed Partial Copyright Licence.

While licensing SFU to permit the above uses, the author retains copyright in the thesis, project or extended essays, including the right to change the work for subsequent purposes, including editing and publishing the work in whole or in part, and licensing other parties, as the author may desire.

The original Partial Copyright Licence attesting to these terms, and signed by this author, may be found in the original bound copy of this work, retained in the Simon Fraser University Archive.

Simon Fraser University Library  
Burnaby, British Columbia, Canada

revised Fall 2011

## **Abstract**

The high incidence of human impact-induced injuries is a serious public health issue that can reduce the quality of life, often leading to chronic pain, dependence on others for daily activities, disability, and even death. The medical and recovery expenses of these injuries impose significant economic and social burdens on the patient and the healthcare system. Such injuries may occur in different groups of people who are most vulnerable and require more attention than others in society, including children, the elderly wheelchair users, and those who are involved in high-risk activities such as construction, transportation and sports. As a result, there is an urgent need for the design and development of an effective impact protection safety device. Injury criteria, such as head injury criterion (HIC) and neck injury criterion (NIC), are metrics by which to identify, compare, and improve the effectiveness of impact isolators. Head Injury Criterion (HIC) is one of the most globally adapted measures of injury analysis. In recent years, many researchers have investigated HIC Optimization by applying both traditional and novel methodologies and algorithms.

In this thesis, the concept of "Effective Operating Region (EOR)" is introduced as a potential element in impact isolator. The concept has been analytically established and then applied in order to show the feasibility of generating near-square waveform impact impulse using linear springs and dampers. The functionality of the proposed approach has been examined by conducting properly designed experiments and by applying the approach in tangible examples of impact isolators such as airbags. A novel self-inflated foam airbag was eventually developed and experimentally verified. The tests results for this airbag have shown that the proposed EOR concept is effective in practice.

**Key Words** —Impact-related injury, Injury criteria, HIC, Square waveform, Effective Operating Region (EOR), Self inflated foam airbag

## **Acknowledgements**

It is with immense gratitude that I acknowledge the support and help of my Supervisor Dr. Arzanpour throughout my research. His patience and kindness, as well as his academic experience, have been invaluable to me and his encouragements refreshed me in desperate moments. His confidence on me was a great source of motivation during the years I worked with him. I would also like to thank Dr. Vijayaraghavan and Dr. Wang for kindly reviewing the thesis. I would like to extend my gratefulness to Dr. Rad for his time and energy as my session defence chair.

Over last two years, I have benefited greatly from the support of my friends in Canada and particularly in Vancouver. I am indebted to my roommates Soheil Sadeqi and Arash Tavassoli as well as my trusted friends Mehran Ahmadi and Maryam Yazdanpour who were always there for me. I would also like to thank Amir Maravandi, Kambiz Haji, Fattaneh Nadimi, Mehran Shirazi, Ehsan Asadi, Reza Harirforoush, Vahid Zakeri, Maryam Soleymani, Esmaeil Tafazzoli and Arina Aboonabi who treated me as a family and made Vancouver a convivial place for me to live. Particularly, I would like to thank my old and best friend Hamid Rafiei who has been always there for me during last ten years.

Last but not least I owe my deepest gratitude to my family, Imaneh, Amir and specially my parents Ali and Shahin for their unflagging love and support throughout my life. If there is any honor in this degree it belongs to them. It is my dream to return part of their pure love and favour that they dedicated to me during every single moment of my life.

# Table of Contents

Approval.....	ii
Abstract.....	iii
Acknowledgements.....	iv
Table of Contents.....	v
List of Tables .....	vii
List of Figures .....	viii
Nomenclature .....	xiv
<b>1. Introduction .....</b>	<b>1</b>
1.1. Thesis Objective.....	9
1.2. Research Novelty .....	9
<b>2. Head Injury criterion (HIC) Optimization for Passive Impact Attenuator as a Single-Degree of Freedom Mass-Spring-Damper System .....</b>	<b>11</b>
2.1. Introduction .....	11
2.2. Optimization Problem .....	12
2.2.1. Case I- Impact Isolator Consisting Independent Spring and Damper Elements .....	13
2.2.2. Case II- Impact Isolator Consisting of Independent Gas Spring and Damper Elements .....	19
2.2.2.1. Gas-Spring Model .....	19
2.2.2.2. Effect of Parameter $L1$ .....	25
2.2.3. Case III- A Self-damped Gas Spring with Initial Pressure of $P_0$ and Auxiliary Reservoir .....	26
2.2.3.1. Effect of Parameter $\mu R$ .....	32
2.3. Chapter Summary .....	34
<b>3. Optimal Impact Attenuator Feasibility by Applying “Effective Operating Region (EOR)” for the Spring Element .....</b>	<b>36</b>
3.1. Introduction .....	36
3.2. Head Injury Criterion Function .....	36
3.3. Optimal Impact Waveform and Its Comparison with Other Waveforms.....	38
3.3.1. Optimal Impact Pulse.....	38
3.3.2. Other Simplified Waveforms .....	39
3.4. Feasibility of Optimal Deceleration Curve (constant acceleration) using Passive Spring Elements.....	48
3.4.1. Effective Operating Region (EOR) of a Spring .....	49
3.4.2. HIC Minimization Subject to a Maximum Displacement $d_{max}$ for a Gas-spring System Applying EOR.....	52
3.4.3. HIC Minimization Subject to a Maximum Displacement $d_{max}$ for a Mass-spring System with Linear Spring Applying EOR .....	55
3.4.4. Effect of EOR on a Linear Spring .....	59
3.4.5. Effective Operating Region of a Spring in a Mass-spring damper System.....	64
3.5. Chapter Summary .....	68

<b>4.</b>	<b>Venting Implementation into the Airbag with the Aim of Applying EOR Concept in Optimal Impact Energy Management.....</b>	<b>69</b>
4.1.	Introduction .....	69
4.2.	Optimum HIC during Impact using Airbag with Venting Implementation .....	73
4.3.	Airbag Impact Dynamics Modelling .....	73
4.3.1.	Impact Attenuation from Standpoint of Thermodynamics .....	73
4.3.2.	System Dynamics Equation .....	77
4.3.2.1.	Change in Airbag Contact Area and Volume .....	77
4.3.2.2.	Gas Dynamics Equations [44] .....	78
4.4.	Integration of Gas-dynamics and System Dynamics for Airbag during Impact.....	82
4.5.	Test Apparatus.....	82
4.5.1.	Test Apparatus Trouble-Shooting .....	84
4.6.	Comparing Experimental Results with Simulation Results.....	86
4.7.	Chapter Summary .....	96
<b>5.</b>	<b>Self-Inflator Foam Airbag.....</b>	<b>98</b>
5.1.	Introduction .....	98
5.2.	Analytical Modelling of Open-Cell Foam.....	99
5.3.	Foam Airbag Deployment Time and Injury Protection.....	108
5.3.1.	Expansion Time .....	108
5.3.1.1.	Testing Apparatus .....	108
5.3.1.2.	Simulation Results.....	109
5.3.1.3.	Deployment Time Improvement.....	114
5.3.2.	Impact Attenuation of Foam Airbag.....	117
5.3.2.1.	Experimental Results.....	120
5.4.	Chapter Summary .....	126
<b>6.</b>	<b>Conclusion and Future Work.....</b>	<b>127</b>
	<b>References .....</b>	<b>129</b>
	<b>Appendices .....</b>	<b>135</b>
Appendix A.	MADYMO Simulations .....	136
Appendix B.	MATLAB Code for Airbag Impact Response .....	138
Appendix C.	Further Refinements to Drop-test Apparatus.....	146

## List of Tables

Table 1-1: Major types of incident in workplaces in BC, 2011 [6].....	2
Table 1-2: Probability of Head Injury Relative to HIC Score .....	6
Table 3-1. Comparison of Waveforms efficiency with respect to square waveform .....	46
Table 3-2: Comparing optimum HIC scores for different combination of linear spring-damper with/without preload .....	61
Table 3-3. Comparison of a standard damper dimensions for a specific stroke length [37] .....	63
Table 3-4. Design specifications of a spring manufactured by Leespring [38] .....	63
Table 3-5. Effect of preload on optimum HIC in existence of damping .....	66
Table 5-1. Physical parameters of open cell foam sample used .....	112



## List of Figures

Figure 1-1: Percent of All Injury Hospitalizations for Seniors Related to a Fall, Age 65+, 2008/09 [4] .....	2
Figure 1-2: Distribution of injury categories in workplaces in BC, 2002-2011 [6].....	3
Figure 1-3: Distribution of short term disabilities, long term disabilities and fatal claims in workplaces in BC by type of incident, 2011 [6].....	3
Figure 1-4: Wayne State University tolerance curve for head injury .....	6
Figure 2-1. Impact of mass on a spring-damper system.....	14
Figure 2-2. Range of achievable maximum displacement for certain natural frequencies and a range of damping ratios for impact input .....	15
Figure 2-3. Range of achievable maximum displacement for certain damping ratios and a range of natural frequency values for impact input.....	16
Figure 2-4 Range of achievable maximum displacement for certain natural frequencies and a range of damping ratios for unit step input .....	16
Figure 2-5. Peak acceleration vs. maximum displacement for different natural frequencies and damping ratios for impact isolator, Case I.....	17
Figure 2-6 HIC vs. maximum displacement for different natural frequencies and damping ratio's for impact isolator, Case I .....	17
Figure 2-7. HIC values vs. peak acceleration for different natural frequencies and damping ratio's for impact isolator Case I .....	18
Figure 2-8 HIC values vs. maximum Displacement for a few natural frequencies and a range of damping ratio's for impact isolator Case I .....	19
Figure 2-9 Schematic of a gas-spring system .....	19
Figure 2-10. Comparison of adiabatic and isothermal models of gas spring [34] ....	22
Figure 2-11. Comparison of impact isolators Case I and Case II, a) Maximum displacement vs. frequency, b) HIC vs. frequency .....	24
Figure 2-12. Optimal damping ratio variation for airbags Case I and Case II .....	25
Figure 2-13. Effect of parameter $L_0$ for impact isolator Case II, $L_0 = 33$ cm, a) displacement comparison, b) HIC comparison.....	27
Figure 2-14. A model of the air spring [35] .....	28

Figure 2-15.	An equivalent dynamic model of the air spring [29] .....	28
Figure 2-16.	Comparison of impact isolators Case I and Case III, a) maximum displacement vs. frequency, b) HIC vs. frequency .....	31
Figure 2-17.	Effect of parameter $\mu R$ for impact isolator Case III, L, a) displacement comparison , b) HIC comparison .....	33
Figure 2-18.	Effect of parameter $\mu R$ on optimal damping ratio values for airbag of Case III.....	33
Figure 2-19.	Comparing $\xi_{optimal}$ values for HIC and peak acceleration for airbag of Case III when $\mu R = 500$ .....	34
Figure 3-1.	Optimal head impact acceleration for minimal HIC.....	39
Figure 3-2.	Comparison of head impact waveforms with $v_0 = 3\text{ m/s}$ ; a) acceleration, b) velocity, c) displacement .....	45
Figure 3-3.	Comparison of $Eff_{HIC}$ and $Eff_{Ap}$ for different waveforms .....	46
Figure 3-4.	HIC vs. Acceleration for different waveforms with $v_0 = 3\text{ m/s}$ ; a) peak acceleration, b) 3 ms Acceleration .....	47
Figure 3-5.	Discretized-type of waveform efficiency for impact attenuation. Black line corresponds to square wave and red line corresponds to ramp-down waveform.....	48
Figure 3-6.	Single degree of freedom mass spring system .....	49
Figure 3-7.	Schematic design applying Effective Operating Region of a spring during impact absorption .....	52
Figure 3-8.	Force-displacement curve for a linear spring with initial pre-load and operating in its effective region ( $x_{s2} = x_s$ in Figure 3-7) .....	52
Figure 3-9.	Schematic display of effective operating region of different types of springs subject to minimal distance of $x_s$ .....	53
Figure 3-10.	Schematic display of applying effective operating region for a gas spring a) implementation of a pressure relief valve b) pressure change within gas spring during the impact. — corresponds to sufficiently large size valve, — corresponds to medium size valve, -- corresponds to small valve.....	54
Figure 3-11.	Optimum stiffness vs. Preload value for minimal HIC, $v_0 = 3\text{ m/s}$ , $d_{max} = 16\text{ cm}$ .....	57
Figure 3-12.	Optimum HIC scores for various preload values, $v_0 = 3\text{ m/s}$ , $d_{max} = 16\text{ cm}$ .....	57

Figure 3-13. Optimum HIC vs. Stiffness for different preloads, $v_0 = 3 \text{ m/s}$ , $d_{max} = 16 \text{ cm}$ .....	58
Figure 3-14. Optimum HIC vs. Maximum displacement for different stiffness and preload values, $v_0 = 3 \text{ m/s}$ , $d_{max} = 16 \text{ cm}$ .....	58
Figure 3-15. Convergence history in GA for case of linear spring (no Preload), $v_0 = 3 \text{ m/s}$ , $d_{max} = 16 \text{ cm}$ .....	59
Figure 3-16. Convergence history in GA for case of linear spring-damper (no preload), $v_0 = 3 \text{ m/s}$ , $d_{max} = 16 \text{ cm}$ .....	60
Figure 3-17. Convergence history in GA for case of linear spring (with preload), $v_0 = 3 \text{ m/s}$ , $d_{max} = 16 \text{ cm}$ .....	60
Figure 3-18. Convergence history in GA for case of linear spring-damper (with preload), $v_0 = 3 \text{ m/s}$ , $d_{max} = 16 \text{ cm}$ .....	61
Figure 3-19. Comparison of reactive force in spring and damper with the corresponding ideal forces, $v_0 = 3 \text{ m/s}$ , $d_{max} = 16 \text{ cm}$ .....	62
Figure 3-20. Schematic of standard damper made by AVM manufacturer [37].....	63
Figure 3-21. Convergence history in GA for case of linear spring-damper (without preload) $v_0 = 3 \text{ m/s}$ , $d_{max} = 16 \text{ cm}$ , $c = 35 \text{ N.s/m}$ .....	67
Figure 3-22. Convergence history in GA for case of linear spring-damper (with preload) $v_0 = 3 \text{ m/s}$ , $d_{max} = 16 \text{ cm}$ , $c = 35 \text{ N.s/m}$ .....	67
Figure 3-23. Comparison of reactive forces in spring and damper with and without preload, $v_0 = 3 \text{ m/s}$ , $d_{max} = 16 \text{ cm}$ , $c = 35 \text{ N.s/m}$ .....	68
Figure 4-1. Implementation of airbags in different locations interior of a vehicle [ <a href="http://www.whyhighend.com/airbags.html">http://www.whyhighend.com/airbags.html</a> ].....	70
Figure 4-2. Implementation of seatbelt based airbags in automotive and aircraft [ <a href="http://chrisescars.com/ford-designs-new-airbag-seatbelt/">http://chrisescars.com/ford-designs-new-airbag-seatbelt/</a> ] .....	70
Figure 4-3. Implementation of airbag within the cabin of motorcycle and helicopter [ <a href="http://www.motorcycleinfo.co.uk">http://www.motorcycleinfo.co.uk</a> ],[ <a href="http://tractors.wikia.com/wiki/Airbag">http://tractors.wikia.com/wiki/Airbag</a> ] .....	70
Figure 4-4. Implementation of airbag for CST-100 spacecraft designed and developed by Boeing [ <a href="http://eandt.theiet.org">http://eandt.theiet.org</a> ].....	71
Figure 4-5. Implementation of airbag exterior to the vehicle's cabin for pedestrian safety, developed by Volvo [ <a href="http://www.spiegel.de">http://www.spiegel.de</a> ].....	71
Figure 4-6. Implementation of human airbags a) protection against human fall, b) protection against wheelchair overturn [42] .....	72

Figure 4-7. Schematic display of different stages for airbag compression during impact	74
Figure 4-8. Schematic diagram of integrated model of airbag accounting for the gas dynamics, head dynamics and changes in airbag shape .....	76
Figure 4-9. Airbag shape alteration during the compression .....	78
Figure 4-10. Definition of upstream and downstream pressure for the airbag model	80
Figure 4-11. Experimental data for calculating discharge coefficient $C_d$ [44] .....	81
Figure 4-12. Airbag test apparatus developed to measure the head acceleration during the impact.....	83
Figure 4-13. Airbag test apparatus designed in Solidworks .....	84
Figure 4-14. Electric circuit used to suppress inductive noise due to voltage variations in solenoid coil.....	85
Figure 4-15. Experimental results vs. Simulation results at $h_0=70\text{cm}$ , a) $P_0 = 101\text{Kpa}$ , b) $P_0 = 103\text{Kpa}$ , c) $P_0 = 115\text{Kpa}$ .....	87
Figure 4-16. Experimental results vs. Simulation results at $P_0 = 101\text{Kpa}$ , a) $h_0 = 10\text{cm}$ , b) $h_0 = 48\text{cm}$ , c) $h_0 = 80\text{cm}$ .....	88
Figure 4-17. Acceleration vs. Time, effect of dropping height.....	89
Figure 4-18. Acceleration vs. Time, effect of impacting mass.....	90
Figure 4-19. Acceleration vs. Time, effect of initial impact energy .....	91
Figure 4-20. Acceleration vs. <i>Aorifice</i> for different drop heights .....	91
Figure 4-21. HIC vs. <i>Aorifice</i> for different drop heights .....	92
Figure 4-22. Velocity of head at the end stroke of airbag vs. <i>Aorifice</i> .....	93
Figure 4-23. Modified values of HIC vs. <i>Aorifice</i> .....	93
Figure 4-24. Acceleration vs. <i>Aorifice</i> for values of orifice area section close to optimum value .....	94
Figure 4-25. HIC vs. <i>Aorifice</i> for different initial pressure in airbag, $h_0 = 70\text{ cm}$ .....	94
Figure 4-26. HIC vs. <i>Aorifice</i> for different values of opening pressure; a) $h_0 = 20\text{ cm}$ , b) $h_0 = 40\text{ cm}$ .....	96
Figure 5-1. The schematic display of the reactive elements in flexible foam during compression.....	101
Figure 5-2. Fluid-filled structure of open cell foam developed in [52].....	101

Figure 5-3. A lumped model for open-cell foam [54].....	102
Figure 5-4. A simple mechanical model for foam dynamic behaviour [55].....	102
Figure 5-5. Typical Stress-strain curve for open-cell foam a) schematic display of different regimes of compression, b) experimental result.....	103
Figure 5-6. A single-degree-of-freedom system with nonlinear viscoelastic elements [60]	104
Figure 5-7. Experimental results showing “hysteric” as well as “strain-rate dependency” behaviour of foam.....	105
Figure 5-8. Experimental test setup for measuring frequency response of open-cell foam	106
Figure 5-9. Softening-hardening behaviour of foam in frequency response.....	107
Figure 5-10. Frequency hysteresis for nonlinear open cell foam .....	107
Figure 5-11. Test apparatus for measuring expansion time of open-cell foam.....	108
Figure 5-12. Compression of fluid-filled block of open cell foam.....	109
Figure 5-13. Schematic of the experimental test setup for measuring foam stiffness, b) experimental test setup .....	111
Figure 5-14. Expansion time of square shape foam sample given in Table 5-1 .....	112
Figure 5-15. Test setup for measuring foam permeability and inertial coefficient, a) Experimental setup, b) a sealed isolated chamber containing the porous sample.....	113
Figure 5-16. Measurement of permeability and inertia coefficient of open cell foam	114
Figure 5-17. Different foam sample patterns for improved expansion time .....	115
Figure 5-18. a) Stiffness of foam samples a, b and f in Figure 5-17, b) Expansion time of each sample .....	116
Figure 5-19. Schematic model of an air spring .....	118
Figure 5-20. A foam airbag with single cavity, a) schematic display, b) the fabricated foam airbag .....	119
Figure 5-21. A foam airbag with sectional cavity, a) schematic display, b) the fabricated foam airbag.....	120
Figure 5-22. a) foam airbag structure, b) a complete 9 section air cavity sample, c) 1, 4 and 9 section samples of ½ and 3 inch height .....	121
Figure 5-23. A drop test setup for measuring impact isolation performance of foam airbag samples .....	122

Figure 5-24.	Comparison of Mylar effect on a sealed foam airbag with a simple foam sample, $h_0 = 30\text{cm}$ .....	123
Figure 5-25.	Effect of sectional design for foam airbags with 3" thickness, a) $h_0 = 10\text{ cm}$ , b) $h_0 = 30\text{cm}$ , c) $h_0 = 40\text{cm}$ .....	125
Figure 5-26.	Comparison of foam reduction in foam samples with different thicknesses, $h_0 = 30\text{cm}$ .....	126

## Nomenclature

$A$	cylinder cross-section area for a gas spring ( $\text{m}^2$ )
$a_p$	peak acceleration during impact ( $\text{m s}^{-2}$ )
$A_{p\{sw\}}$	peak acceleration during impact for a square waveform ( $\text{m s}^{-2}$ )
$A_c$	airbag contact area during impact ( $\text{m}^2$ )
$A_{orifice}$	cross-sectional area of orifice ( $\text{m}^2$ )
$A_z$	rate of change in cross-sectional area of foam airbag ( $\text{m}^2 \text{s}^{-1}$ )
$A_v$	rate of change in volume of foam airbag ( $\text{m}^3 \text{s}^{-1}$ )
$B_0$	fluid inertia of porous structure at zero deformation (m)
$C_D$	discharge coefficient
$D$	airbag diameter (m)
$f^*$	ideal force of spring for effective operating region (N)
$F_0$	preload force for spring (N)
$g$	gravity acceleration ( $\text{m s}^{-2}$ )
$h$	foam thickness (m)
$K_0$	permeability of porous structure at zero deformation ( $\text{m}^2$ )
$m$	mass of striking object (kg)
$P$	pressure, (Pa)
$T$	temperature (K)
$T_{p\{sw\}}$	period of impact for a square waveform (s)
$u_{out}$	velocity of gas released from airbag during impact ( $\text{m s}^{-1}$ )
$h_{out}$	enthalpy of gas released from airbag during impact (J)
$m_{out}$	mass of gas released from airbag during impact (kg)
$U_{gas}$	internal energy of gas inside airbag (J)
$V$	gas volume inside the gas spring ( $\text{m}^3$ )
$w$	mass of gas in airbag (kg)
$W_b$	boundary work in airbag compression
$x_p$	maximum displacement during impact (m)

## Greek symbols

$\zeta$	damping coefficient
$\omega_n$	natural frequency (rad/s)
$\omega_d$	damped natural frequency (rad/s)
$\theta$	phase shift between displacement and velocity for mass spring damper
$\gamma$	ratio of specific heat in polytrophic process
$\rho$	gas density (kg m <sup>-3</sup> )
$\phi$	Volume fraction of open cells in foam structure

## Abbreviations

<i>HIC</i>	Head Injury Criterion
EOR	Effective Operating region



# 1. Introduction

Injuries caused by impact to the body are a frequent occurrence across society. In fact, human impact-induced injury is one of the major public health challenges facing the world today. In particular, trauma caused by impacts causes millions of human deaths yearly. Such impact-induced injuries may occur in vehicle collisions, at industrial or construction sites, in sports, in military activities, and fall-related accidents including falls from high altitude and falls from beds or wheelchairs. According to National Safety Council statistics, after heart disease, cancer, and stroke, accidents are the fourth-leading cause of death among all age groups [1]. Among all accidents, car crashes are ranked first at 49%, falls are 28%, while motorcycle and work-related accidents are other sources of fatalities. In addition, these accidents are a major cause of a wide range of injuries and short- and long-term disabilities that affect functionality, normal life activities, and independence of those who injured. These injuries lower the quality of life and impose significant financial burden on patients and healthcare services [2].

The seriousness of this problem is highlighted by reports and statistics available for fall-related injuries. Approximately one-third of elderly people experience falls at least once a year [3]. This statistic translates to nearly 1.4 million seniors in Canada having fallen at least once in 2005. Elderly people's falls are a growing source of injury, and it is estimated that by 2031 nearly \$4.4 billion will be needed to cover the medical costs of falls [4]. And even if a fall does not lead to injury, it can cause psychological trauma and renewed fear of falls in seniors, and restrict seniors' participation in daily activities [5].

Falls, and being struck by or against objects, are also reported as the main causes of injuries at workplaces. According to WorkSafeBc, these are responsible for nearly 50% of all the short- and long-term disabilities and fatal claims reported in 2011 [6]. This analysis also indicates that 43% of the serious injury claims were related to these types of accidents. It is important to mention that in 2011, WorkSafeBC paid more than \$1 billion for medical claims, and a considerable portion of that was related to fall and collision-related injuries [6].

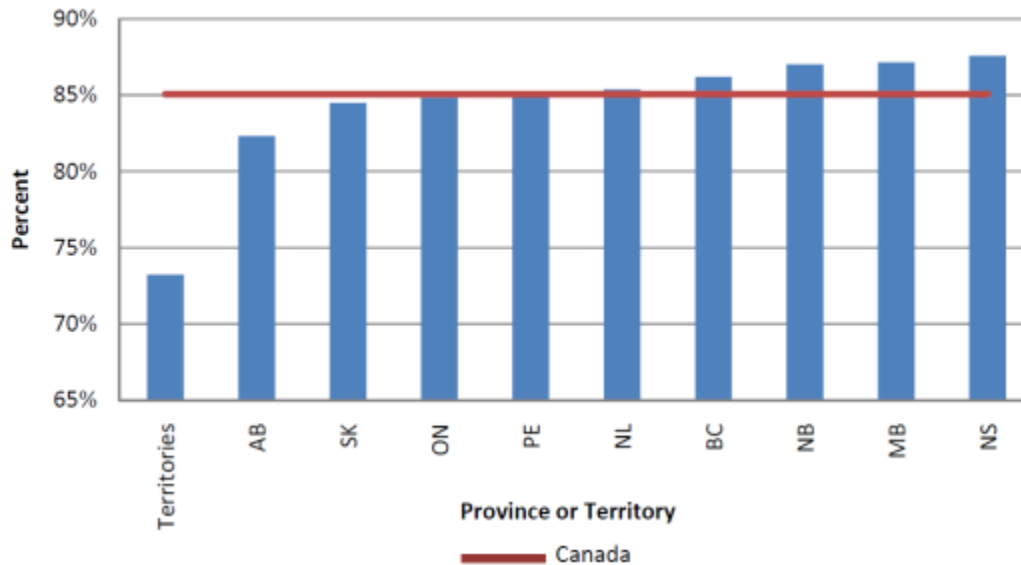


**Figure 1-1: Percent of All Injury Hospitalizations for Seniors Related to a Fall, Age 65+, 2008/09 [4]**

**Table 1-1: Major types of incident in workplaces in BC, 2011 [6]**

Major type of incidents	Older workers	Younger workers	Percentage of injuries occurring to older workers
Ergonomic	38%	42%	11%
Falls	27%	19%	17%
Struck	21%	28%	10%
Noise exposure	4%	0.2%	80%
Other	10%	11%	12%
Total	100%	100%	

Wheelchair-related accidents are also reported in the literature as a source of injury for the users. In the United States, an average of 36,559 non-fatal, wheelchair related accidents that require an emergency department visit occur annually [7]. Wheelchair falls can cause injuries to the head 41%, neck/spine 26.8%, shoulder, and hip 17.1% [8]. Some of these injuries, such as fracture, are serious, and an extended hospital stay (estimated at 4 to 8 weeks) and the inevitable loss of strength due to immobilization may result [9]. Wheelchair-related falls often cost between \$25,000 and \$75,000 to cover the bills for Medicare, insurance companies, and hospitals [10].

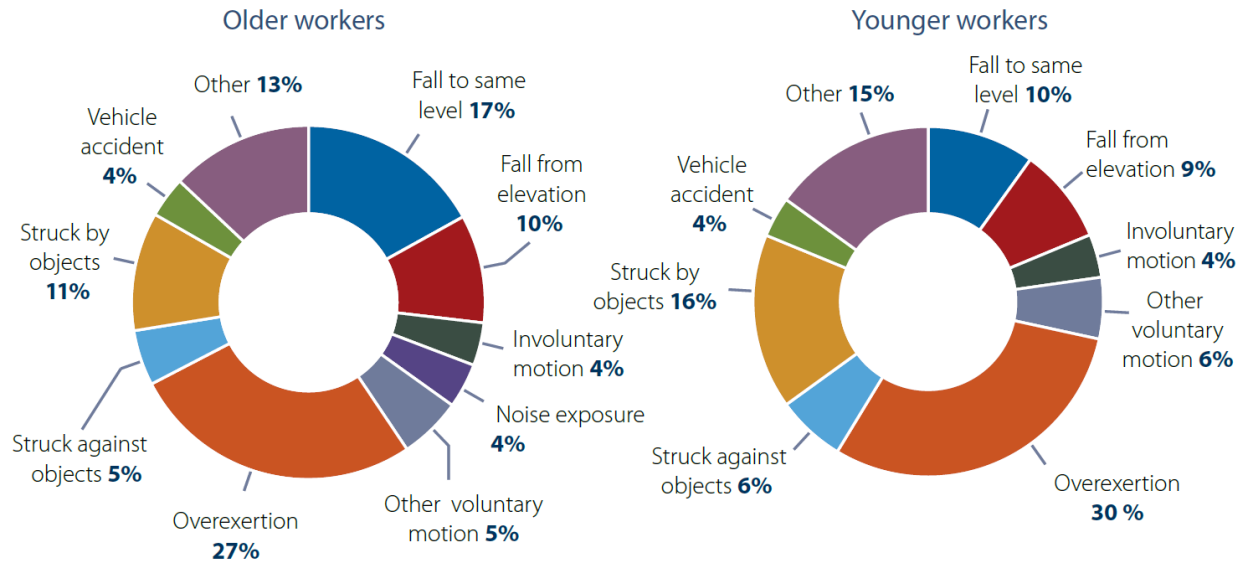


**Figure 1-2: Distribution of injury categories in workplaces in BC, 2002-2011 [6]**

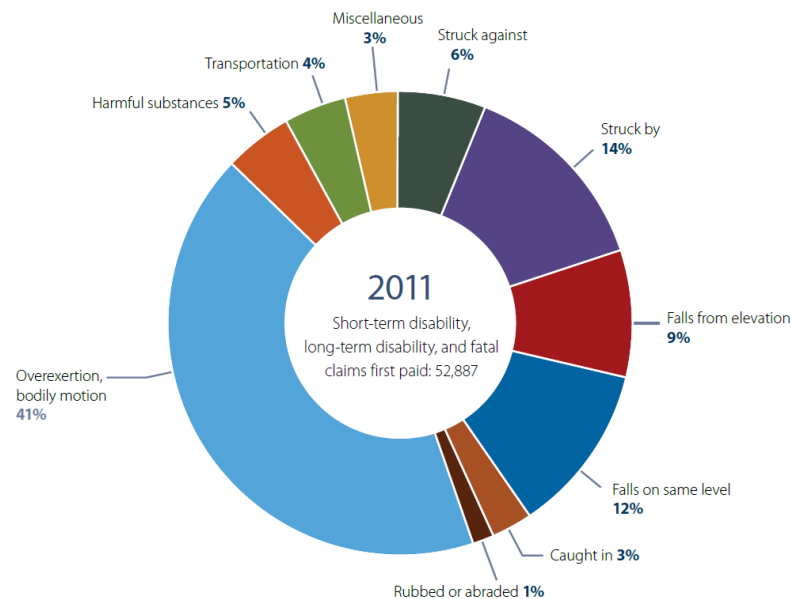


**Figure 1-3: Distribution of short term disabilities, long term disabilities and fatal claims in workplaces in BC by type of incident, 2011 [6]**

To protect against those injuries, specialized shock isolation techniques need to be developed. Systematic application of optimal control for shock isolation was originally used to protect engineering equipments from intensive shock loads, and the method was soon extended to problems associated with impact-related accidents for humans. Protecting a person from

impact-related injuries requires the introduction of a device known as impact isolator to absorb the impact energy and reduce the force transmitted to the body. Depending on the situation, the impact isolator can include devices such as helmets, seat belts, and airbags. To evaluate the impact isolation performance of these devices, several injury criteria are defined. These criteria are quantitative response metrics indicating the severity of injury in terms of mechanical quantities such as displacements, velocities, accelerations, forces and energy. Head Injury Criterion (HIC), Thoracic Trauma Index (TTI), Femur Injury, and Neck Injury are a few of the well-known criteria described in the injury assessment literature. Federal Motor Vehicle safety Standards (FMVSS) No. 208 specifies guidelines and formulae to calculate each criterion. The acceptable thresholds for each injury type are obtained from Hybrid II anthropometric test dummies (ATD) that are instrumented with a variety of sensors and body parts to measure the impact characteristics. Additional performance criteria, including geometric characteristics/restrictions such as maximum allotted space design, may also be considered to evaluate the isolation performance of the safety device. The optimum design of different safety devices based on various performance criteria has received increasing attention among many researchers. For the optimum design of impact isolators, it is enticing to lower the values of all performance criteria as far as possible. However, there are usually conflicting trends between different criteria, and therefore, it is impossible to obtain a global optimum point.

Head injury tolerance is a rough approximation of a complex living biological system being damaged by external impact [11]. The location, magnitude, direction and duration of impact all influence the response of the brain and skull, and can result in skull fracture if the impact is above tolerable range of the human head. Among all injury criteria, HIC is the most globally used criterion for measuring the severity of injury in the cases where the human head is engaged as the impacted mass. The HIC was first introduced by Gurdjian and his collaborators ([12], [13], [14]) and evolved with experiments measuring the effects of acceleration on the intracranial pressure of dogs. By measuring the energy required to cause concussive effects, Gurdjian succeeded to attain a limit between impact intensities causing fatal and non-fatal injuries. The results obtained in their experiments were interpreted as a correlation between a tolerable level of acceleration and the impact time duration, which is known as “Wayne State tolerance curve” (WSTC), shown in Figure 1-4. The analytical expression for HIC, later established by Versac [15], was derived from this curve and is expressed by formula:

$$HIC = \left\{ \left[ \frac{1}{t_2 - t_1} \int_{t_1}^{t_2} a(t) dt \right]^{2.5} (t_2 - t_1) \right\}_{max}$$

where  $a(t)$  is the magnitude of the acceleration of the centre of mass of the brain, and  $t_1$  and  $t_2$  are the initial and final times at which the HIC attains a maximum value. Based on ASTM-F1292-04 Standard, this time interval is restricted to a maximum of 15 milliseconds, and  $HIC < 1000$  is known as a critical value for avoiding fatal injuries to the head. This equation as well as WSTC reflects the dependency of the severity of the injury on both the mean magnitude of the acceleration of the head induced by an impact pulse and the duration of this pulse. Indeed, this implies that very high head acceleration is tolerable for a brief short time. The probability of brain injury at different HIC scores is documented in ASTM-F1292-04 Standard, and summarized in

Table 1-2. It is worth noting that even falls from less than a one-meter height correspond to HIC values higher than 1000.

Various means are available to compute the value of HIC for post-analysis of the data gathered during an impact. Algorithms that employ a direct method of computation involve all possible interval combinations and yield the exact value of HIC. Hutchinson et al. [16] study mathematical features of the HIC analytical expression and present necessary conditions for optimal solution and critical points of HIC function. These conditions are represented through a few theorems and lemmas, forming a basis for various algorithmic strategies to provide a more efficient means of calculating HIC [17]. By applying the theorems described there, an explicit closed-form solution for HIC is obtained for the class of functions  $a(t)$  that can be encountered in practice [18]. Furthermore, a few researchers have contributed to finding an analytical model of head impacts with an object. Such analytical expressions, if properly validated, eliminate the need for excessive experimental tests as well as huge computational effort to produce a HIC calculation. Young [19] models the head by means of a fluid-filled spherical shell of inconstant thickness impacted by a solid elastic sphere. In such a model, the explicit closed-form expression for impact duration, the peak force transmitted to the head, and the head injury criterion are derived. Moreover, Heydari et al. [20] propose a more realistic model of the head as an ellipsoid, and the corresponding equations are derived. In these modelling efforts, the geometric and material properties of human head are considered.

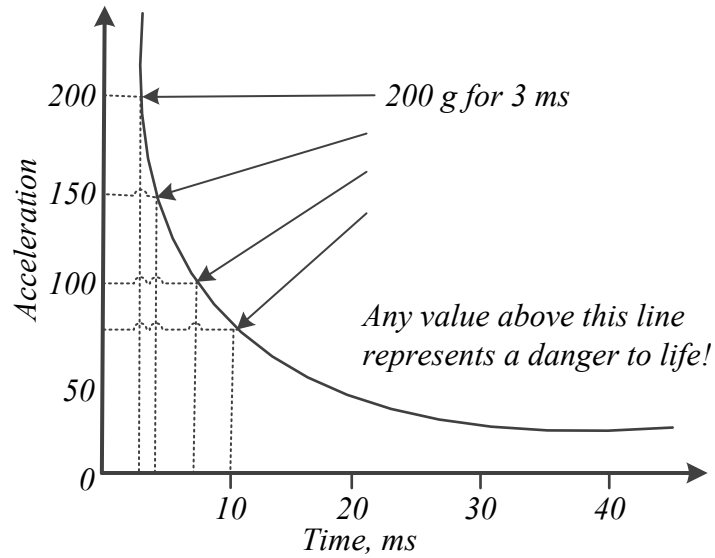


**Figure 1-4: Wayne State University tolerance curve for head injury**

**Table 1-2: Probability of Head Injury Relative to HIC Score**

HIC Score	Minor Injury	Moderate Injury	Critical Injury	Fatal
0	0%	0%	0%	0%
250	40%	20%	0%	0%
500	80%	40%	2%	0%
750	95%	70%	4%	0%
1000	98%	90%	8%	2%
1250	100%	95%	10%	2%
1500	100%	98%	20%	4%
1750	100%	100%	45%	10%
2000	100%	100%	70%	30%
2250	100%	100%	90%	70%
2500	100%	100%	95%	90%
2750	100%	100%	98%	95%
3000	100%	100%	100%	100%

Most researchers over the past few decades have acknowledged the significance of HIC optimization from an engineering point of view for designing safety devices. One of the basic

problems associated with the criterion of impact isolation is that of determining minimal HIC, provided that it is constrained to a maximum allowable design space. For example, design parameters of interior structures of cars such – as dashboard, steering wheel, and seat – are normally optimized (to absorb the energy of a head impact) to achieve minimum HIC [17]. Etman et al. [20], consider the optimization of airbag and belt restraint systems in frontal crashes for minimal HIC achievement, subject to constraints by other performance criteria like the distance between head and steering wheel to avoid the direct contact. They utilize MADYMO software for the simulations and find the solution for the optimization problem, considering airbag diameter, airbag vent diameter and inflator gas mass as design variables. A similar analysis has been undertaken for helmets: Deck et al. [21] examine the influence of the helmet shell and foam properties on the human head by coupling the helmet model with the finite element model of the human head and simulating a frontal impact with standard helmet mechanical properties. The simulation results are then applied to numerically optimize the helmet mechanical parameters against biomechanical criteria such as intra-cerebral stress and HIC. In the case of a helmet, additional constraints such as comfort and proper ventilation should also be satisfied within any enhanced design [22] that might compromise its isolation performance. Motorcycle drivers' safety improvement is also considered by implementing modification in devices, such as placing guardrails along the roadsides [23]. Although the guardrails are traffic barriers constructed to protect the vehicles, they can be extremely dangerous by causing severe injuries for motorcycle passengers. Vieira et al. [23] develop an additional energy-absorbing system to be placed on the guardrails; they numerically simulate that using LS-DYNA in order to find the minimal HIC experienced by motorcyclists when implementing the proposed energy absorber. For incidents arising from a fall on playground surfaces, Shorten et al. [24] survey the shock-attenuating characteristics of loose-fill and unitary playground surfaces with the intention to determine optimal properties such as coating thickness and mechanical properties for unitary surface systems. They test the impact attenuation of playground surface samples using a free-falling headform with an instrumented accelerometer. Peak impact deceleration ( $a_{max}$ ) and  $HIC$  are recorded at specific drop heights, and the experimental results are used for the optimization analysis. The same design optimization approaches can be adopted for other safety equipment developed to protect the human body from impacts due to falls, that is, human airbags [25], [26]. Generally speaking, any interior structure/safety device that is impacted by the occupant/falling person is susceptible to numerical or experimental optimization in order to enhance the impact isolation performance.

Despite the many efforts discussed earlier to provide equipment with optimal injury protection, little focus has been placed on the basics of the mechanism of injury. Indeed, after establishing the impact model of the isolator, either experimentally or analytically, they have just been applied to various optimization approaches to find the best combination of design variables to minimize the injury criteria. Hence, the outcomes of most studies are valid for particular situations but have limited advantage for other applications, mainly because the key injury mechanism as a common factor denominator among all impact applications has not been fully identified.

More recently, some studies have explored the essence of the design specifications that should be incorporated into the impact isolator if the “ideal” isolation is to be attained. The ideal isolation in the related literature terminology is assigned to the hypothetically flawless design of an impact isolator that is superior to any real isolator with any engineering configuration, even if it is hardly practical. Pilkey et al. [27] develop optimal control laws for deceleration trend during the impact. They explore two optimized problems and corresponding control laws. In the first problem, the minimal HIC is optimized, provided with displacement of impacting mass to be a constraint, and in the second, minimal displacement is sought subject to the constraint that the HIC score lies below the prescribed thresholds that cause serious injury. However, it is generally unrealistic to anticipate the deceleration curve as having a very sharp rise at the very beginning as developed in their investigation, and therefore, alternative control laws including constant force and power law deceleration are considered instead [27]. Furthermore, Wu et al. [18] propose a new ramp-down triangle waveform to be considered as a baseline for a more realistic ideal deceleration during the impact, and the efficiency of other cited waveforms in the literature is defined in respect of the proposed head impact pulse. They also apply the new-developed optimal waveform to the case of a pedestrian impact with a vehicle bonnet, in line with new stringent requirements set by the European Parliament as part of their pedestrian protection. Although their work is demonstrated to be more effective than square waveform in terms of minimal HIC, the optimality of the proposed impact pulse might be challenged if minimal peak acceleration is also considered as a performance criterion. Besides, to the best of my knowledge, no attempt has been made so far to examine the practicality of an ideal waveform using a simple passive isolator, such as linear springs and dampers.



## **1.1. Thesis Objective**

The goal of this study is first, to establish a conceptual design for generating a near-square waveform impact impulse using linear springs and dampers, and then, to demonstrate the functionality of the proposed approach by conducting suitable experiments and assessing its applicability in tangible examples of impact isolators such as airbags.

In Chapter 2, the HIC optimization problem provided with the maximum allowable displacement, as commonly occurs in real-life situations, is considered for a cushioning system. Three simplified and primary models of impact isolator with natural frequency and damping coefficient as the main design variables are introduced. In each case, the optimal values for design variables are obtained, and these form the design charts as a baseline for primary design of the impact isolator.

In Chapter 3, the new concept of Effective Operating Region (EOR) for the spring element is introduced and analytically established. This concept is then applied to the linear spring-damper examined in Chapter 2, to study the feasibility of generating a near-square waveform that results in optimal HIC.

In Chapter 4, the performance of an airbag with the implementation of venting mechanism is studied. The experimental test equipment is designed and built to validate the existent impact model of airbag. Moreover, the influence of a venting mechanism on impact isolation is discussed in terms of EOR concept explained in Chapter 3.

In Chapter 5, the novel self-inflated foam airbag is introduced. The design and challenges associated with this are studied, and design enhancements are proposed as a solution. Experimental tests along with the numerical simulations are also conducted to verify the efficiency of the proposed designs. The test results reveal how the proposed foam airbag is applying the EOR concept explained in Chapter 3 in order to improve impact attenuation.

## **1.2. Research Novelty**

The conceptual design approach for optimal impact isolator is analytically established based on the “Effective Operating Region” concept for an elastic element. The implementation

of the new design concept has led in design and development of the innovated novel self-inflator foam-airbag that has been recently patented.

## **2. Head Injury criterion (HIC) Optimization for Passive Impact Attenuator as a Single-Degree of Freedom Mass-Spring-Damper System**

### **2.1. Introduction**

To avoid serious injury to the head during an impact, safety devices like airbags (cushioning system) are of crucial importance, but they must be well designed to prevent fatal injury. The Head Injury Criteria (HIC) is defined as a measure of the severity of an impact on the occupant's head and is related to both the deceleration magnitude and its duration. The ASTM-F1292-04 Standard recommends a threshold value of HIC of 1000, while a HIC value of 700 is recommended for ensuring occupant safety. A device as simple as a mechanical spring-damper or a cushioning system can therefore act as an impact isolator. Peters [28] tries to find the optimum stiffness and damping for a mass-spring-damper system during impact that minimizes transmitted force. As the commonly used criterion, however, it is suggested that the optimization problem for impact isolator design be defined based on HIC rather than the force or peak acceleration, and therefore, our primary simulations are focused on finding optimized stiffness and damping values for minimal HIC. In our simulations, the maximum permissible displacement of impacting mass due to the physical limitations of the protective device is considered a constraint.

The primary objective of this chapter is to perform a systematic investigation of optimal impact energy management by considering three simplified one-degree-of-freedom cushioning systems: 1) simple mass-spring-damper (MSD), 2) gas spring with initial pressure of  $P_0$  in parallel with a dashpot, and 3) gas spring with initial pressure of  $P_0$  and auxiliary reservoir. These cases can adequately model the realistic situations for the primary analysis while avoiding the complexity associated with multiple degree-of-freedom isolation systems. These models cover a large spectrum of isolations systems, including air springs in vehicles [29], and have been recently adopted to model hip protector devices [30]. They can serve, therefore, as a

basis for identifying the main parameters affecting impact attenuator performance. In each case, we analyzed fundamental vibration concepts by changing stiffness and damping characteristics to seek effective impact isolation.

This chapter outlines a number of fundamental considerations that the designer should consider when selecting the components of protective devices, such as an airbag. It is expected that the outcome of this section can be easily extended to more sophisticated and modified impact isolation systems.

## 2.2. Optimization Problem

In mechanical vibration isolators like suspension systems, engine mounts, or railroad vehicle air springs, the reduction of the absolute acceleration is usually the most important goal in optimization ([31], [32]). A vibration isolator reduces absolute acceleration by permitting higher relative deflection of the isolator. The relative deflection, on the other hand, is subject to the physical design constraints, and therefore, optimal suspension is a tradeoff between the acceleration and relative motion.

To prevent head injury by safety devices, minimal HIC is of more interest than minimal acceleration as a widely accepted score of head injury evaluation. Although higher peak acceleration during impact implies higher HIC scores, based on our simulations the optimal values for acceleration minimization differ from values in HIC minimization.

In any optimization problem, the choice of both objective function and constraints is dependent on the practical considerations of the specific application. For the specific case of head protector device, the objective function may include the HIC score constrained to a maximum relative displacement, which can be related to the design parameters  $\omega_n$  (natural frequency) and  $\xi$  (damping coefficient). Moreover, other limitations on the upper and lower bounds of  $\omega_n$  and  $\xi$  (perhaps of crucial importance particularly in impact isolator of case III) may manipulate design parameters. For the simplified isolation systems considered in this chapter, it is generally desired to select  $\omega_n$  and  $\xi$  such that the HIC score of the system is minimized and the relative displacement does not exceed a prescribed level. An obvious solution is to set up a matrix of the admissible values of  $\omega_n$  and  $\xi$  and solve the equation of motion for the isolated mass (head) to determine both the HIC and maximum displacement. In this chapter, three

simple models for the cushioning system have been adopted, the optimization problem is investigated individually, and the results in each case are compared with those in other cases.

### **2.2.1. Case I- Impact Isolator Consisting Independent Spring and Damper Elements**

The cushion system can be modelled as a spring-dashpot system (Figure 2-1). Assuming the head is the impacting mass, the governing equation for the mass-spring-damper system is given in Equation (2-1), with  $v_0$  as initial velocity, which incorporates the initial impact energy as,

$$\ddot{x} + 2\xi\omega_n\dot{x} + \omega_n^2x = 0 \quad (2-1)$$

$$x(0) = 0 \quad \dot{x}(0) = v_0$$

where  $\omega_n$  is the natural frequency and  $\xi$  is the damping ratio, which varies from 0 to 1 for the under-damped situation.

This system has the well-known solution for the under-damped case ( $\xi < 1$ ) given by,

$$x(t) = \frac{v_0}{\omega_d} e^{-\xi\omega_n t} \sin(\omega_d t) \quad (2-2)$$

$$\omega_d = \omega_n \sqrt{1 - \xi^2}$$

The corresponding acceleration obtained from Equation (2-1) is,

$$a = \ddot{x}(t) = \frac{v_0 \sqrt{1 + \omega_d^2}}{\sqrt{1 - \xi^2}} e^{-\xi\omega_n t} \sin(\omega_d t + \theta + \gamma) \quad (2-3)$$

$$\theta = \tan^{-1}\left(\frac{\sqrt{1-\xi^2}}{-\xi}\right), \gamma = \tan^{-1}(\omega_d)$$

The peak values of the displacement and absolute acceleration are,

$$x_p = -\frac{v_0}{w_d} e^{\xi \frac{\theta}{\sqrt{1-\xi^2}}} \sin(\theta) \quad (2-4)$$

$$a_p = -\frac{v_0 \sqrt{1+\omega_d^2}}{\sqrt{1-\xi^2}} e^{\xi \frac{\theta+2\gamma}{\sqrt{1-\xi^2}}} \sin(\gamma) \quad (2-5)$$

which occur where  $\dot{x}(t) = 0$  and  $\ddot{x}(t) = 0$ , accordingly.

Knowing the acceleration experienced by the head during the impact, the corresponding HIC can be calculated from,

$$HIC = \left\{ \left[ \frac{1}{t_2 - t_1} \int_{t_1}^{t_2} a(t) dt \right]^{2.5} (t_2 - t_1) \right\}_{max} \quad (2-6)$$

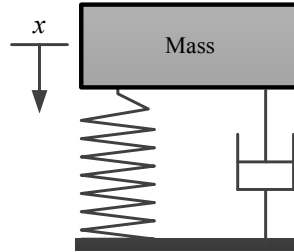


**Figure 2-1. Impact of mass on a spring-damper system**

Based on analytical expressions given in Equations (2-1), (2-5) and (2-6), peak values of acceleration and HIC for the impact input are the function of both the natural frequency and the damping ratio. As a result, in each simulation given in this chapter, a pair of natural frequency and damping ratio is chosen, and the peak values for displacement, acceleration and HIC are measured within the impact duration. In the simulations conducted, the natural frequency was

changed from 1 Hz to 25 Hz as a working frequency domain, and the damping ratio was varied from .1 to 1. The natural frequencies higher than 25 Hz are disregarded since the average impact duration for our experimental tests with airbag was close to 50 ms which is associated with natural frequency of 20 Hz. The initial velocity of 3 m/s (associated with fall from a standing height [33] ) also has been considered for the whole simulations in this chapter. The initial velocity can vary remarkably for different impact scenarios and should be identified accordingly for accuracy of results.

The range of maximum displacement achieved for a fixed value of  $\omega_n$  and for the whole range of damping ratio is plotted in Figure 2-2. As is apparent, increasing  $\omega_n$  decreases displacement, while higher damping ratio further contributes to this reduction. Note that for the impact response of MSD system, the desired displacement range might occur for only certain values of  $\omega_n$ , while for unit step response for any  $\omega_n$ , the whole (and same) range of displacement can be achieved by selecting a proper damping ratio (Figure 2-3, Figure 2-4). This directly indicates the complicated nature of impact response compared with other vibration excitation sources such as step functions or steady-state excitations. Upon comparing Figure 2-3 and Figure 2-4, one might find that the effect of  $\omega_n$  on displacement adjustment is more considerable than the effect of damping ratio. This provides the designer with the opportunity to keep the damping ratio at its optimal value and vary  $\omega_n$  to obtain desired tradeoff between HIC and maximum displacement.

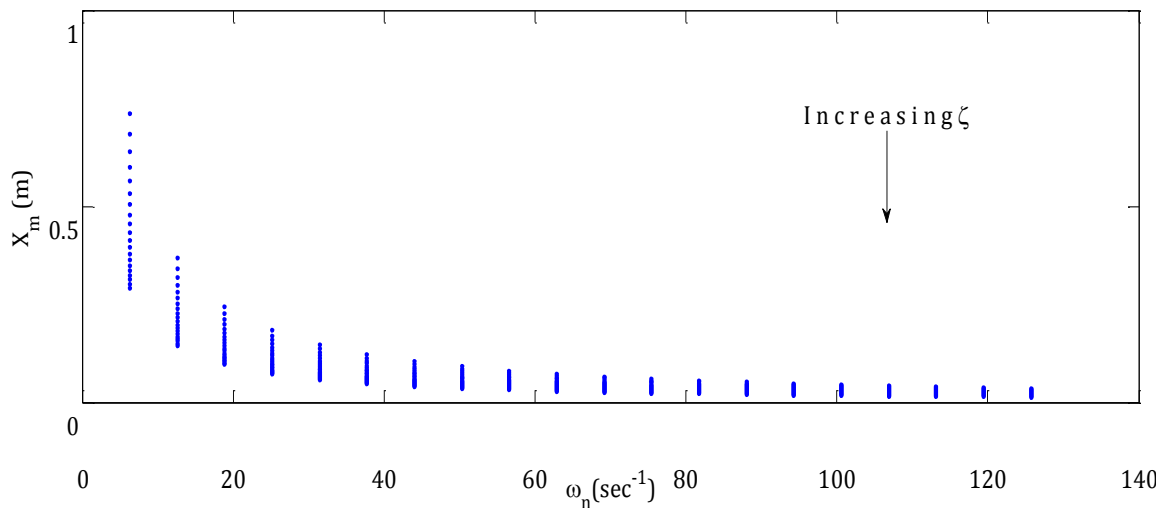


**Figure 2-2. Range of achievable maximum displacement for certain natural frequencies and a range of damping ratios for impact input**

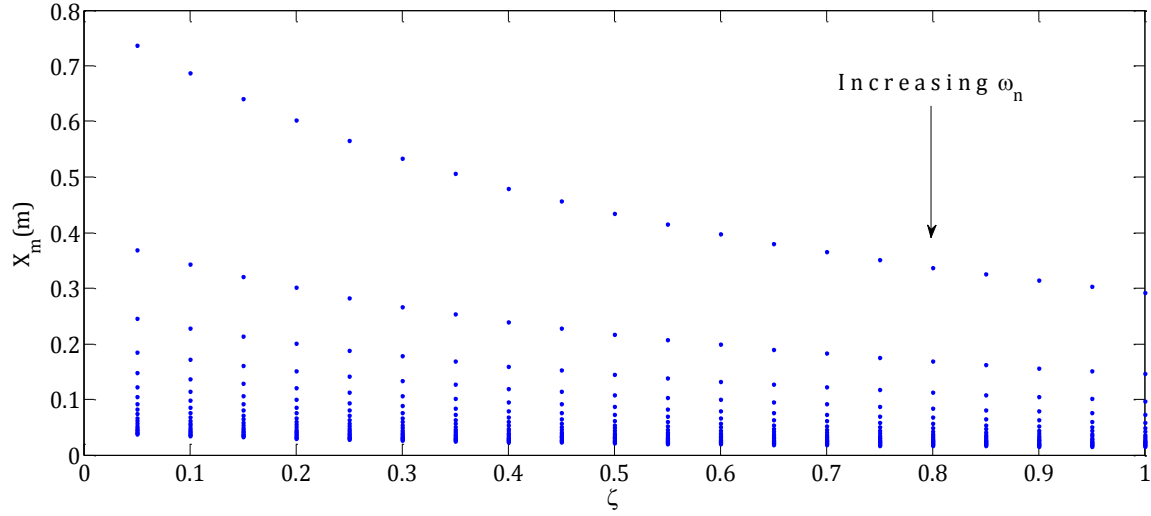


**Figure 2-3.** *Range of achievable maximum displacement for certain damping ratios and a range of natural frequency values for impact input*

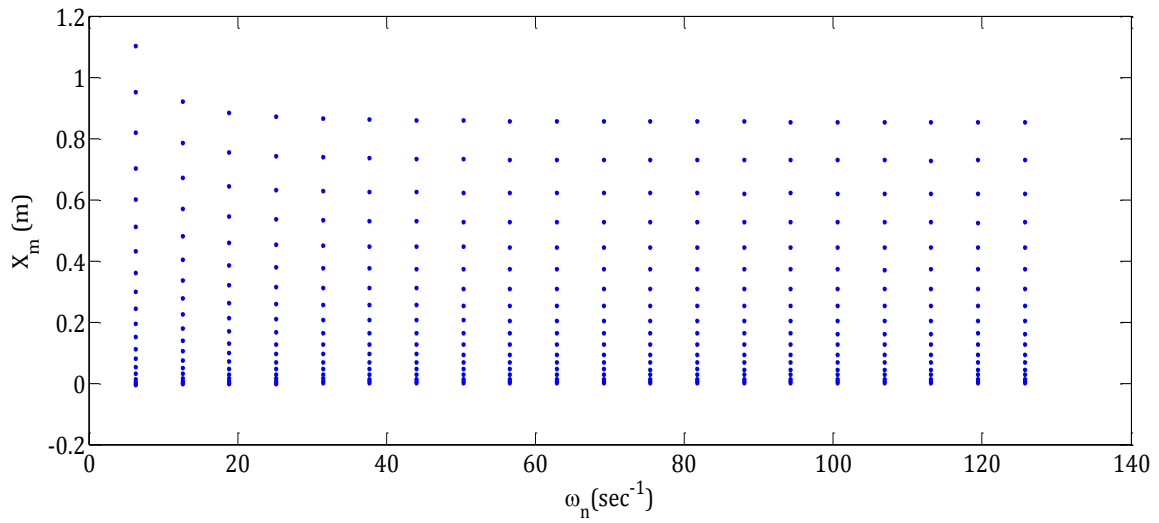


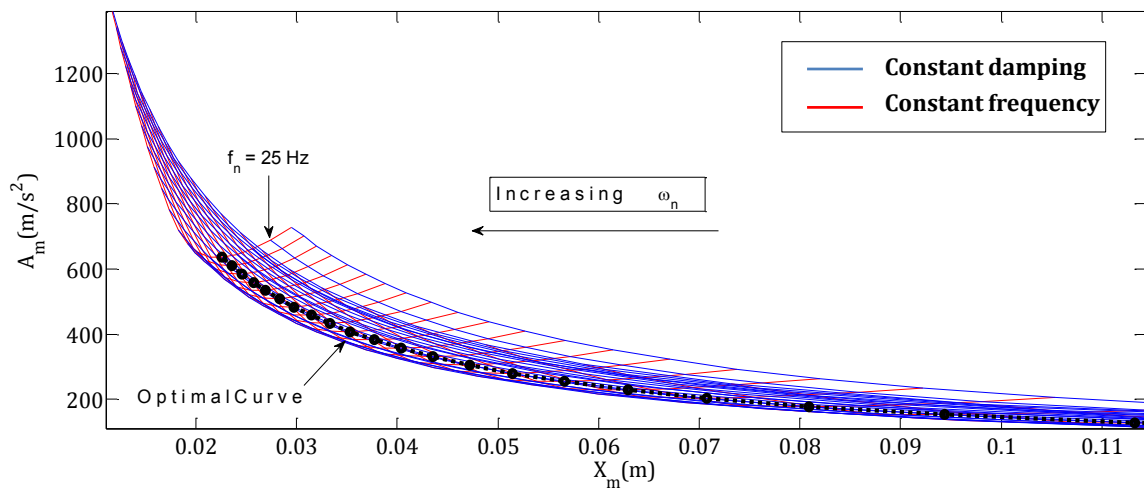
**Figure 2-4** *Range of achievable maximum displacement for certain natural frequencies and a range of damping ratios for unit step input*

In

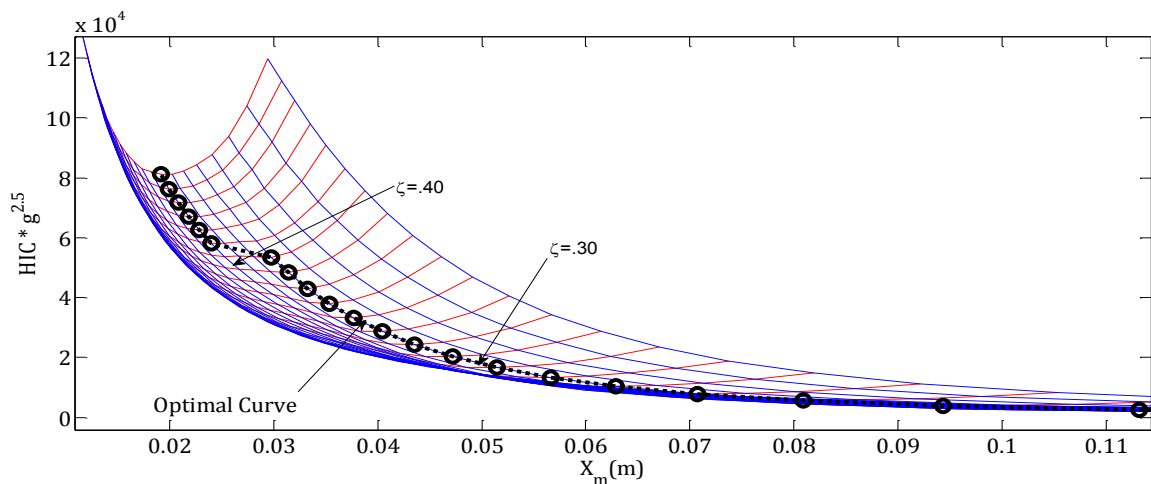
Figure 2-5 the peak acceleration is plotted against the maximum displacement for different values of  $\omega_n$  and  $\xi$ . The red lines in the graph correspond to the responses with fixed values of  $\omega_n$  and the blue lines represent those with fixed values of  $\xi$ .



Figure 2-5 shows that for any certain value of  $\omega_n$  there is an optimal damping ratio where the minimum peak acceleration occurs. For higher values of  $\omega_n$ , the displacement decreases; however, the maximum acceleration tends to increase substantially. In Figure 2-6 the same graph is plotted for the HIC. The optimal curve for either peak acceleration or HIC can be obtained by connecting the points of minima in either  $A_m - X_m$  or  $HIC - X_m$  planes. The utmost feature of this curve is that the sensitivity of HIC (or acceleration) with respect to the maximum displacement is minimal at any point on the optimal curve.



**Figure 2-5.** *Peak acceleration vs. maximum displacement for different natural frequencies and damping ratios for impact isolator, Case I*



**Figure 2-6** *HIC vs. maximum displacement for different natural frequencies and damping ratio's for impact isolator, Case I*

In Figure 2-7, the HIC values are plotted against the peak acceleration values. As illustrated, for lower frequencies, the minimum of both HIC and peak acceleration occurs at  $\xi = .3$ ; however, for higher natural frequencies (lower displacement), the optimal damping ratio for minimum HIC changes to  $\xi = .4$ , where it differs from the optimal  $\xi$  for minimum acceleration which still remains at  $\xi = .3$ . This phenomenon, which implies weaker correlation of optimal peak acceleration and HIC, highlights the importance of choosing HIC as the objective function rather than acceleration for minimal head injury. This significance is even more magnified when one considers that the sensitivity of HIC changes may be too sharp in the vicinity of design parameter values where minimal acceleration occurs. In fact, according to Figure 2-7, for higher  $\omega_n$  values, the sensitivity of HIC with respect to peak acceleration near  $\xi = .3$  (where minimum peak acceleration happens) is substantial for damping ratios less than .3. Therefore, if HIC is intended to be minimal during the impact, selecting a lower limit for damping ratios can be prescribed to ensure that the system never enters the sensitive region and that the peak acceleration is still close to its minimal point.

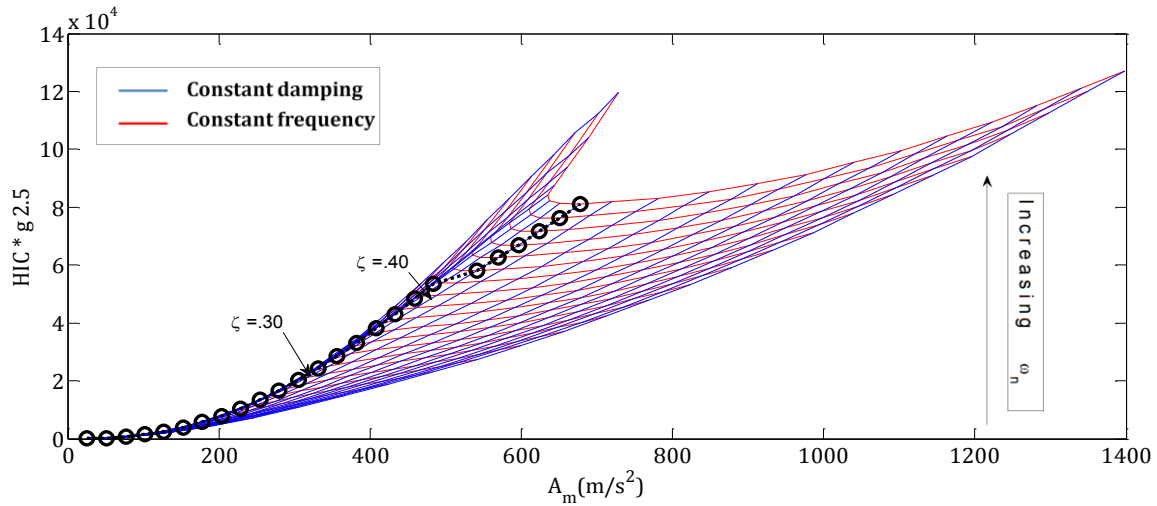


**Figure 2-7. HIC values vs. peak acceleration for different natural frequencies and damping ratio's for impact isolator Case I**

Another interesting observation in Figure 2-8 is that the HIC is plotted against the maximum displacement for just a few selected natural frequencies. The figure clearly shows that the rate of variation in HIC values with respect to  $X_m$  in the vicinity of minimum HIC becomes more significant as  $\omega_n$  increases, while the rate of changes in HIC for lower natural frequencies becomes almost negligible around the point of minima. For lower natural frequencies, therefore,

it may be more reasonable to pick the maximum damping ratio rather than optimal value to further reduce the  $X_m$  (e.g., from .25 m to .15 m, for  $f_n = 2\text{Hz}$ ) at the expense of a lower possibility of the HIC increase.

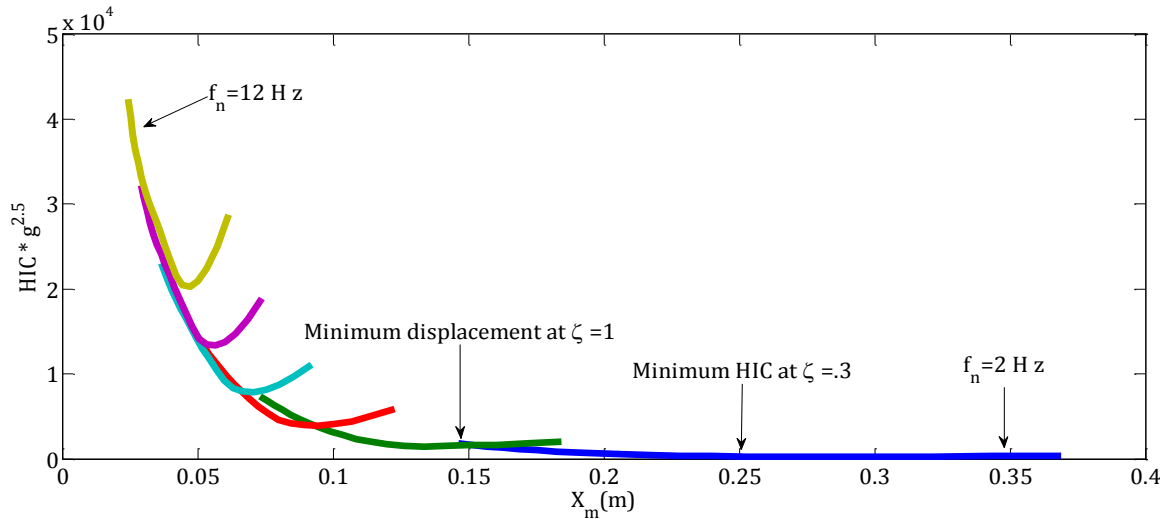


**Figure 2-8** *HIC values vs. maximum Displacement for a few natural frequencies and a range of damping ratio's for impact isolator Case I*

## 2.2.2. Case II- Impact Isolator Consisting of Independent Gas Spring and Damper Elements

### 2.2.2.1. Gas-Spring Model

A gas-spring mechanism, shown schematically in Figure 2-9, is simply a cylinder and piston filled with air or nitrogen gas.

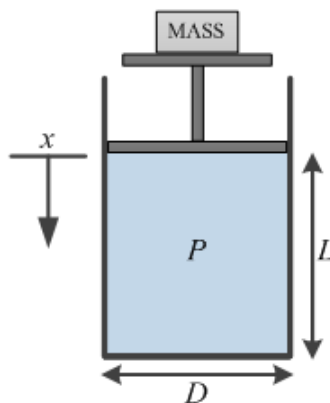


**Figure 2-9** *Schematic of a gas-spring system*

Given that the initial conditions of the system under the external force  $F_1$  are  $P_1$  (initial pressure),  $V_1$ , (initial volume),  $A_1$ , (cylinder cross section area), and  $L_1$  (initial position) , then,

$$P_1 \times A_1 = F_1 \quad (2-7)$$

If the piston is forced to move an absolute displacement,  $x$ , then in this new equilibrium point, the governing equation will be,

$$P_1 \times A_1 + P_2 \times A_2 = F_1 + F_2 \quad (2-8)$$

where  $P_2$  is the gas pressure due to the external force  $F_2$ , and  $A_2$  is the cross section area of the contact surface between mass and gas spring.

Assuming ideal gas properties and, therefore, the perfect gas law, from thermodynamics theory, the following equation will govern,

$$P_1 V_1^\gamma = P_2 V_2^\gamma \quad (2-9)$$

where  $\gamma$  is the ratio of specific heat, which is 1 for an isothermal process and 1.42 for an adiabatic process. In fact, if the process is very slow, the system can exchange heat with the environment and the temperature remains constant (isothermal). On the other hand, if the process is very fast, the system does not have sufficient time to exchange energy with the environment and, therefore, the process is closer to adiabatic.

Relating the pressure inside the cylinder to displacement of piston through Equation (2-9), the equivalent spring force of the gas spring for the isothermal case is,

$$F_2(\text{Isothermal}) = \frac{P_1 \times A_1 \times x}{L_1 - x} \quad (2-10)$$

and for the adiabatic case, the equivalent spring force is,

$$F_2(Adiabatic) = \frac{(P_1 \times A_1) \times ((L_1)^{1.42} - (L_1 - x)^{1.42})}{(L_1 - x)^{1.42}} \quad (2-11)$$

where  $L_1 = \frac{V_1}{(\pi D^2/4)}$

Therefore, the governing dynamic equation during the impact can be expressed as,

$$m\ddot{x} + c\dot{x} + F_2(x) = 0 \quad (2-12)$$

#### **A) Impact Isolator Modelled as Gas-spring and Damper Elements (Isothermal Assumption)**

Assuming the isothermal process occurring in gas-spring during the impact and modelling of the damper side as a linear dashpot, and also assuming the linearizing of the gas-spring force term with the assumption  $\frac{x}{L_1} \ll 1$ , the governing equation for the impacting mass can be derived as,

$$m\ddot{x} + c\dot{x} + \frac{P_1 A_1}{L_1} x = 0 \quad (2-13)$$

Equation (2-13) can be treated exactly the same as the MSD system discussed in case I. However, since during the impact, the system can undergo relatively large displacement, assuming  $\frac{x}{L_1} \ll 1$  might not be valid. Nonlinear terms in the gas-spring force must therefore be included. Moreover, according to experiments conducted by Eslaminasab [34], the reactant force generated in gas-spring during the compression shows a higher order of nonlinearity for greater displacement range, which supports the inclusion of nonlinear terms in Equation (2-10). By expanding Equation (2-10) using Taylor series and extracting first terms, this equation can be written as,

$$\frac{P_1 \times A_1 \times x}{L_1 - x} = \frac{P_1 A_1}{L_1} x + \frac{P_1 A_1}{L_1^2} x^2 + \frac{P_1 A_1}{L_1^3} x^3 + \dots \quad (2-14)$$

Substituting Equation (2-14) in Equation (2-12) and assuming  $\omega_n = \frac{P_1 A_1}{m L_1}$ , and also replacing  $\xi = c/2m\omega_n$ , Equation (2-13) can be rewritten as,

$$\ddot{x} + 2\xi\omega_n\dot{x} + \omega_n^2 x + \frac{\omega_n^2}{L_1} x^2 + \frac{\omega_n^2}{L_1^2} x^3 = 0 \quad (2-15)$$

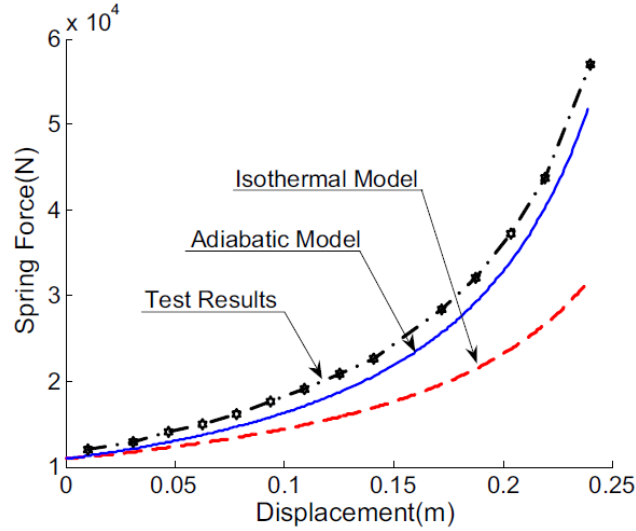


**Figure 2-10. Comparison of adiabatic and isothermal models of gas spring [34]**

In Equation (2-15),  $\omega_n$  is the natural frequency and  $\xi$  is the damping ratio of the gas-spring. However, this equation has an extra parameter,  $L_1$ , which can be tuned independent of  $\omega_n$  and  $\xi$  to achieve the desired level of isolation. This additional parameter could offer a wider range of design parameters to achieve the minimal HIC for a specific maximum displacement, as will be discussed later.

## B) Impact Isolator Modelled as Gas-spring and Damper Elements (Adiabatic Assumption)

Since we are experiencing an impact process, isothermal assumption may not reveal the best results. The study performed by Eslaminasab [34] suggests that considering adiabatic process for gas spring matches the experimental tests better than the isothermal model (Figure 2-10). To improve the accuracy of governing equation for the impacting mass, the term  $F_2$  in Equation (2-12) is replaced with the corresponding force for adiabatic process, and again, the nonlinear terms are included for higher accuracy. In this case, therefore, similar to the isothermal case, the governing equation can be written as,

$$\ddot{x} + 2\xi\omega_n\dot{x} + \omega_n^2x + 1.71\frac{\omega_n^2}{L_1}x^2 + 1.95\frac{\omega_n^2}{L_1^2}x^3 = 0 \quad (2-16)$$

To understand how the model in Case II differs from that of Case I, the minimal HIC and associated maximum displacement are plotted against natural frequency for each pair of  $(\omega_n, \xi_{optimal})$ , as shown in Figure 2-11.

Comparing the results for Case I and Case II in Figure 2-11 we find negligible change in HIC values between two cases for the whole range of natural frequencies. On the other hand, there is a change in maximum displacement for lower natural frequencies, but this difference between two cases vanishes quickly as natural frequency is increased (Figure 2-11 (a)). The reason is that the nonlinear term (Equation (2-15)) is more effective for higher values of  $x$ , which corresponds to lower natural frequencies. In other words, as the  $\omega_n$  increases the displacement drops and, therefore, the nonlinear term contribution is no longer dominant. In addition, Figure 2-11(a) indicates that the abovementioned phenomenon is more obvious in an adiabatic process than in an isothermal one since the corresponding nonlinear terms are of higher orders of magnitude (Compare Equations (2-15) and (2-16) ). However, the decrease in maximum displacement for low frequency region is dependent on initial length of gas spring ( $L_1$ ), which will be briefly explained in section 2.2.2.2. Indeed, as discussed in that section, the proper choice of  $L_1$  is important for displacement reduction even for lower frequencies, since, for some  $L_1$  values, there is no overall reduction in safety device travelling space compared with Case I.

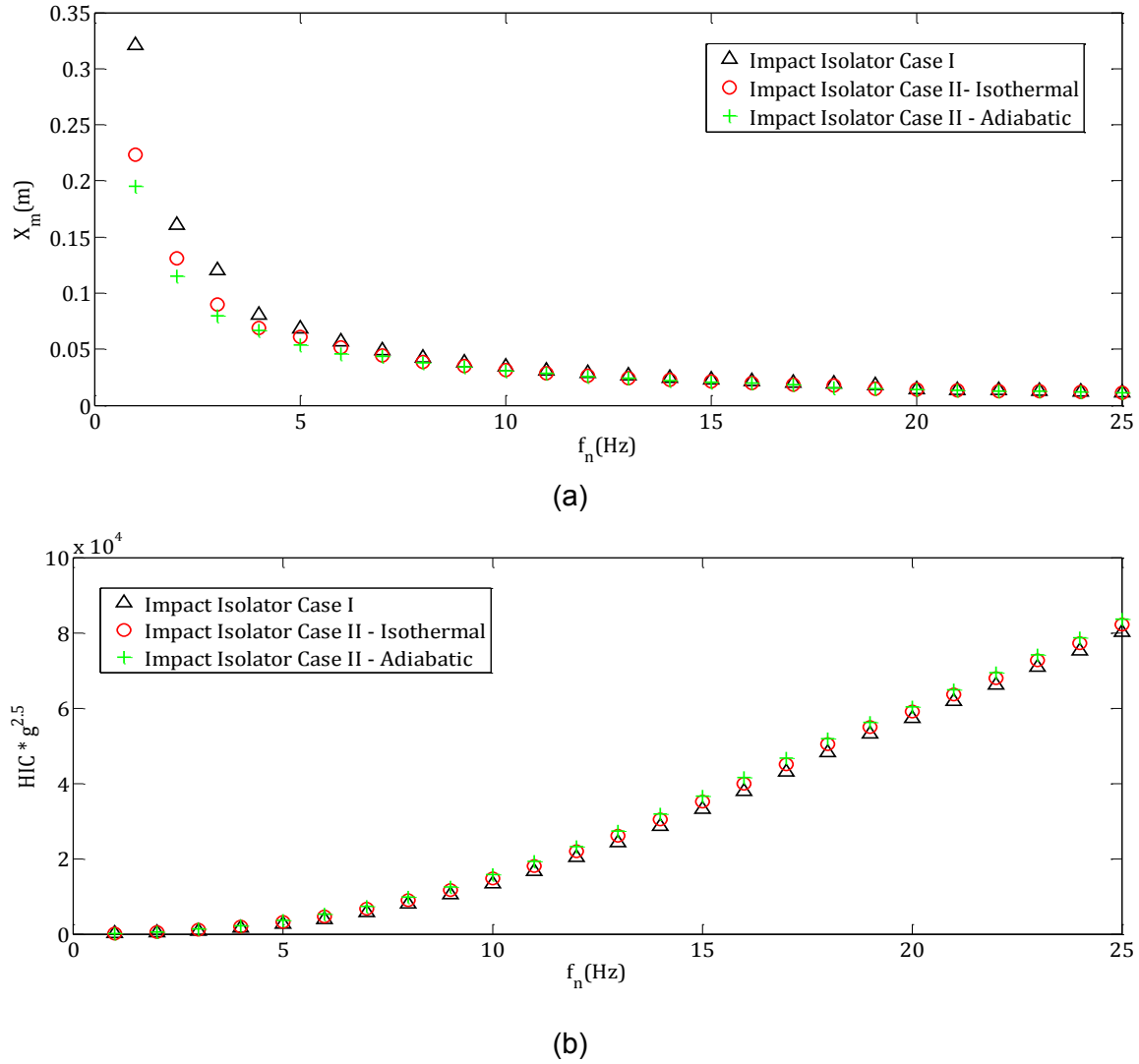


**Figure 2-11. Comparison of impact isolators Case I and Case II, a) Maximum displacement vs. frequency, b) HIC vs. frequency**

Another difference between the two cases being considered concerns the greater dependency of optimal damping values on the natural frequency for the impact isolator of Case II. Therefore, design of the impact isolator in Case II needs more caution in selecting proper damping, which, along with the desired natural frequency, will result in optimum HIC. In other words, in this case the optimum damping values are remarkably different for two different natural frequencies, particularly for lower frequencies. Hence, if the natural frequency of the impact isolator is assumed to be chosen first, then the appropriate damping value should be picked based on that natural frequency. However, if there is any miscalculation in the value of the natural frequency of the designed isolator, that selected damping no longer results in



minimal HIC. In contrast, the variation in optimal damping value as a function of natural frequency in Case I was bounded in a narrower range. Thus, the minimal result was more secure for any value of damping close to its optimum value, which is almost fixed for any natural frequency. This is especially obvious for lower frequencies, as shown in Figure 2-12.

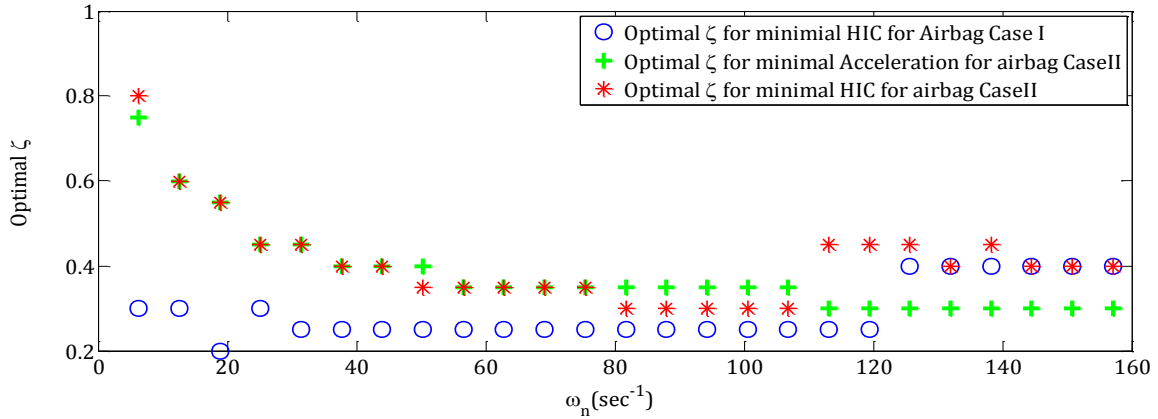


**Figure 2-12. Optimal damping ratio variation for airbags Case I and Case II**

#### 2.2.2.2. Effect of Parameter $L_1$

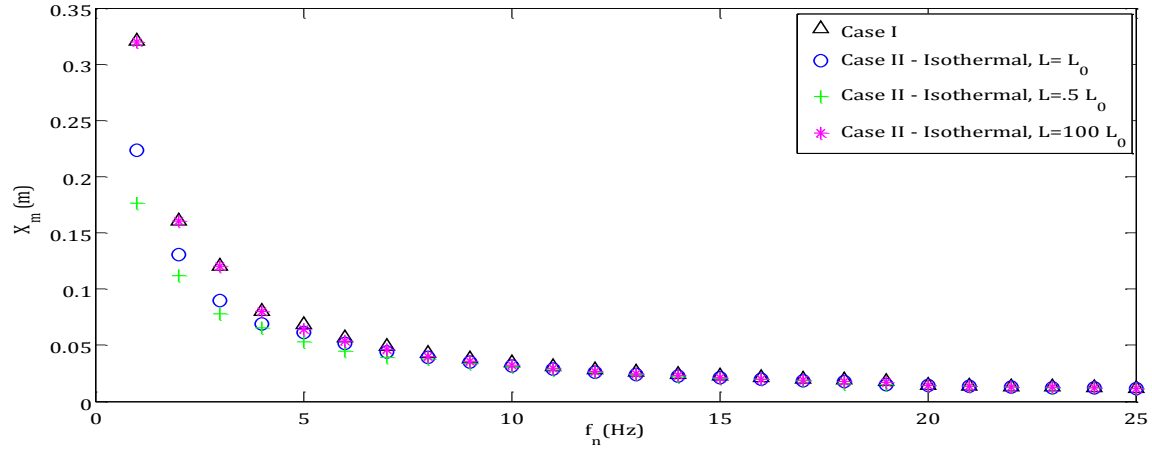
As was mentioned previously, for the impact isolator model adopted in Case II, there is an additional parameter  $L_1$  which can be tuned independently of  $\omega_n$  and  $\xi$ , which may demonstrate better isolation capability for this model. The effect of parameter  $L_1$  is shown in Figure 2-13. It is clear that by decreasing  $L_1$ , the maximum displacement for lower frequencies is significantly reduced, while the changes in HIC values can be neglected. Note that in the air spring, the  $L_1$  determines the overall working space needed for the impact isolator. For example, suppose the initial length is  $L_1 = 33$  cm for the air spring, then, although the maximum displacement of impacting mass is 22 cm at  $f_n = 1$  Hz, we need overall space of 33 cm in order to place the air spring in the system. The same working space is required for the MSD system at  $f_n = 1$  Hz to absorb the same impact (see Figure 2-13 (a)). Therefore, the lower displacement of impacting mass achieved in this situation for Case II does not result in an improvement compared with the impact isolator of Case I. However, as  $L_1$  is reduced, the overall working space required for the impact isolator is also reduced to the point where the maximum displacement of impacting mass coincides exactly with the initial length of the air spring. This situation is to our utmost advantage since the whole available space is used to absorb the impact energy as opposed to cases with higher initial lengths where only a portion of available

space is used. Such a phenomenon occurs here at  $L_1 = 17$  cm, as shown in Figure 2-13 (a). By further decreasing  $L_1$ , the bottoming down phenomenon may occur in a real-life situation. For example, by reducing  $L_1$  to 11 cm, the maximum displacement resulting from our simulations would be around 14 cm, which is higher than the length of the air spring, implying that the impacting mass bottoms out. This corresponding simulation result is not included in Figure 2-13 since it is not a valid design for impact isolator. Therefore, the optimum value for  $L_1$  can be found such that the overall performance of the impact isolator for lower frequencies is improved compared with the MSD system. On the other hand, further increasing  $L_1$  for the low frequency region increases the maximum displacement of impacting mass; however, compared with Case I, this value is smaller but it asymptotically approaches a similar level.

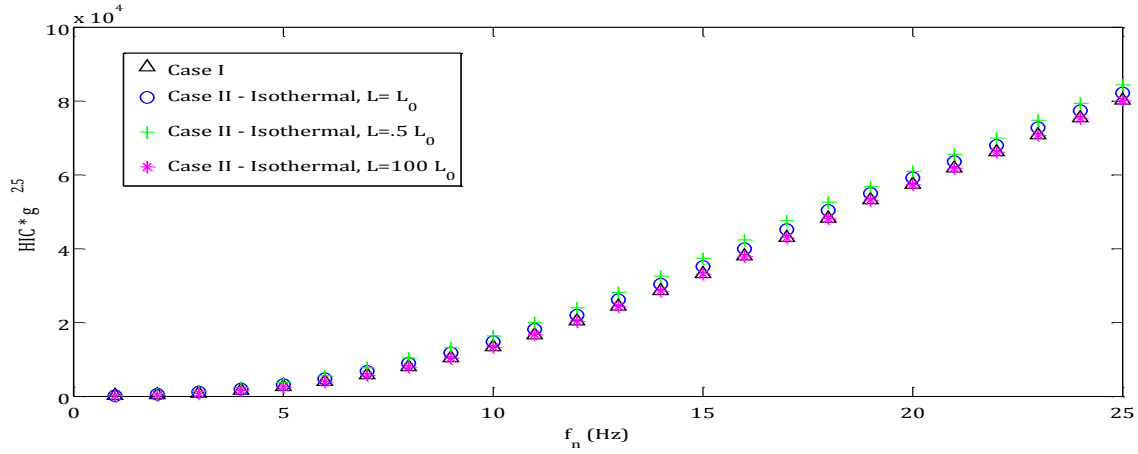
### **2.2.3. Case III- A Self-damped Gas Spring with Initial Pressure of $P_0$ and Auxiliary Reservoir**

It is well known that in addition to acting as a spring, air springs are self-damping elements. The self-damping action in the air spring can be modelled by placing an orifice between the air spring and the auxiliary reservoir, or by placing it on a partition which divides the interior of the air spring as shown in Figure 2-14 [35]. This kind of self-damping air spring is widely adopted for air suspensions in railroad vehicles; however, the concept underlying the impact isolation performance of the model used here can be adopted for any impact isolation application, and its results can be compared with those obtained in Case I and Case II.

The self-damped air spring studied here is illustrated by a simple linear mechanical model presented in [29]. In order to properly compare this model with those represented in Case I and Case II, the natural frequency and damping ratio of the proposed system is calculated and the transient response due to impact is analyzed.



(a)



(b)

**Figure 2-13. Effect of parameter  $L_0$  for impact isolator Case II,  $L_0 = 33$  cm, a) displacement comparison, b) HIC comparison**

Assuming adiabatic process during the impact, the dynamic model for the air spring can be obtained by examining the energy dissipation due to flow pass through the orifice, as follows [29],

$$\begin{cases} m\ddot{x} + (K_1 + K_2)x - K_1y = 0 \\ c\dot{y} + (1 + \lambda)K_1y = K_1x \end{cases} \quad (2-17)$$

where,

$$k_1 = \gamma A_e^2 \frac{P_0}{V_a}, \quad k_2 = (P_0 - P_a) \frac{dA_e}{dx}$$

$$c = R A_e^2 W_0, \quad \lambda = \frac{V_a}{V_b}$$
(2-18)

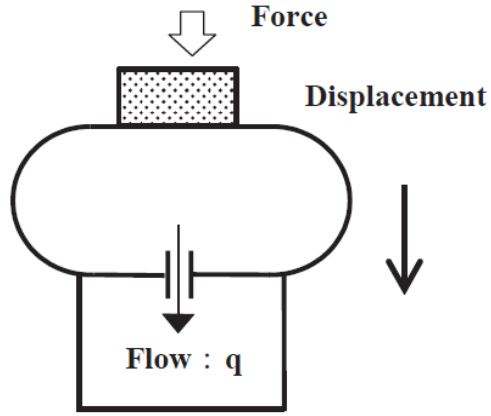


**Figure 2-14.** A model of the air spring [35]

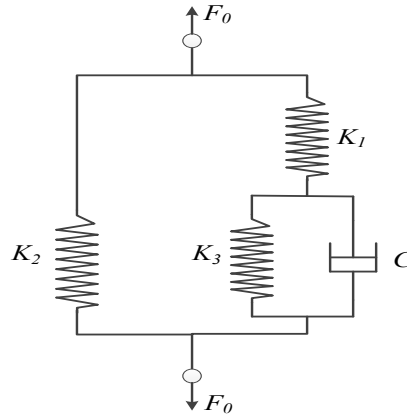


**Figure 2-15.** An equivalent dynamic model of the air spring [29]

Eliminating  $y$  in Equation (2-17) gives,

$$m\ddot{x} + \frac{mk_1}{c}(1 + \lambda)\ddot{x} + (k_1 + k_2)\dot{x} + \frac{k_1}{c}(\lambda k_1 + \lambda k_2 + k_2)x = 0$$
(2-19)

Therefore, the characteristic equation of this ordinary differential equation is,

$$\mu^3 + \left(\frac{k_1}{c}\right)(1 + \lambda)\mu^2 + \frac{(k_1 + k_2)}{m}\mu + \frac{k_1}{mc}(\lambda k_1 + \lambda k_2 + k_2) = 0 \quad (2-20)$$

If  $k_1$  is not extremely large, Equation (2-20) has two sets of solution; one is a non-vibratory solution,  $\mu = -\mu_R$ , and the other is a vibratory solution with damping,  $\mu = \mu_{CR} \pm \mu_{CI}$ , which are equivalent to the roots of equation  $\ddot{x} + 2\xi\omega_n\dot{x} + \omega_n^2x = 0$ . Therefore, the natural frequency and damping ratio of the proposed system can be explicitly incorporated into the system's governing equations using Equation (2-21).

$$(\mu + \mu_R)(\mu^2 + 2\xi\omega_n\mu + \omega_n^2) = 0 \quad (2-21)$$

$$\mu^3 + (2\xi\omega_n + \mu_R)\mu^2 + (2\xi\omega_n\mu_R + \omega_n^2)\mu + \mu_R\omega_n^2 = 0$$

By comparing Equation (2-20) with Equation (2-21), the governing equation can be rewritten as,

$$\ddot{x} + (2\xi\omega_n + \mu_R)\dot{x} + (2\xi\omega_n\mu_R + \omega_n^2)x = 0 \quad (2-22)$$

where the airbag model's parameters are related to  $\omega_n$ ,  $\xi$  and  $\mu_R$  by,

$$\left\{ \begin{array}{l} k_1 = m(2\xi\omega_n\mu_R + \omega_n^2) \\ \lambda = \frac{m\mu_R\omega_n^2}{k_1(2\xi\omega_n + \mu_R) - m\mu_R\omega_n^2} \\ c = \frac{\lambda k_1^2}{m\mu_R\omega_n^2} \end{array} \right. \quad (2-23)$$

The Equation (2-22) has the well-known solution as described by,

$$x = C_1 e^{-\mu_R t} + e^{-\zeta \omega_n t} (C_2 \cos \omega_d t + C_3 \sin \omega_d t) \quad (2-24)$$

and where in Equation (2-24), by applying initial velocity  $v_0$ , the coefficients  $C_1$ ,  $C_2$  and  $C_3$  can be obtained as,

$$C_1 = \frac{2\zeta \omega_n v_0}{\mu_R^2 - 2\zeta \omega_n \mu_R + \omega_n^2} \quad (2-25)$$

$$C_2 = -C_1$$

$$C_3 = \frac{v_0}{\omega_d} - \frac{(-\mu_R + \zeta \omega_n)}{\omega_d} C_1$$

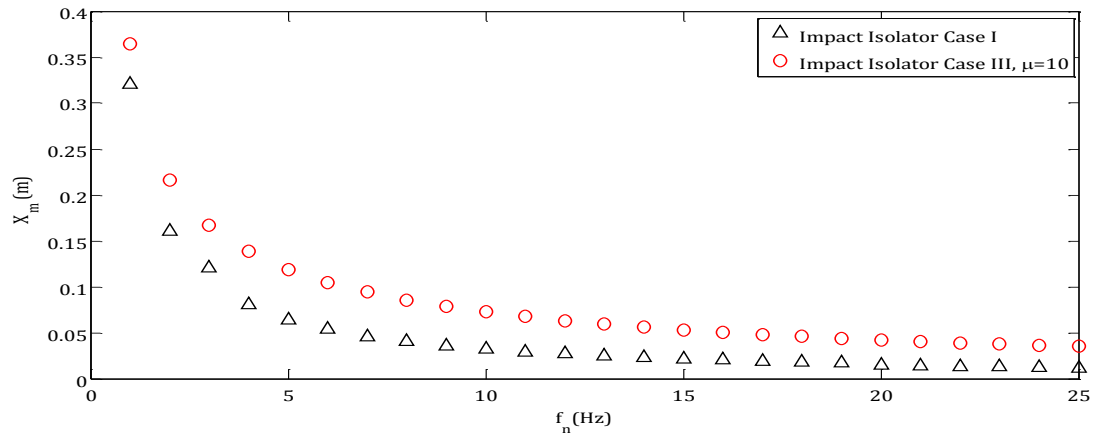
By derivating twice from Equation (2-25), the equation for acceleration during the impact can be expressed with the general form of Equation (2-26),

$$\ddot{x} = C_1 \mu_R^2 e^{-\mu_R t} + e^{-\zeta \omega_n t} (A_c \cos \omega_d t + A_s \sin \omega_d t) \quad (2-26)$$

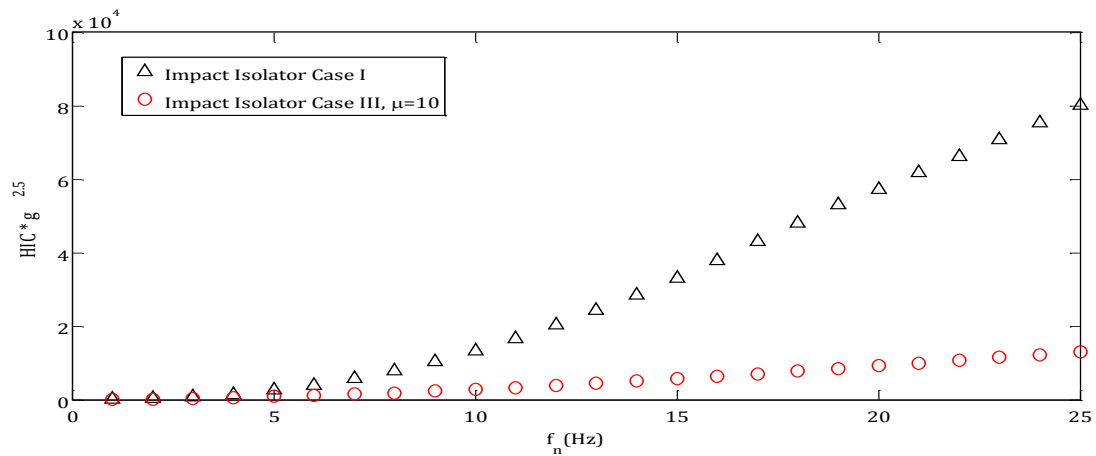
where  $A_c$  and  $A_s$  are functions of  $C_1, C_2, C_3, \zeta$  and  $\omega_n$  and can be calculated using Equation (2-24).

The similar analysis done in Cases I and II can be conducted here to find the minimal HIC against maximum displacement based on  $\omega_n$  and  $\xi$  variation. As shown in Figure 2-16, for the low-frequency region, at a certain natural frequency and almost the same HIC, the maximum displacement is increased by a small order of magnitude compared with that in Case I. Meanwhile, for the high-frequency region, the HIC value for small change in maximum displacement is noticeably reduced in Case III compared with that in Case I. For example, at  $f_n = 25\text{Hz}$ , there is a huge reduction in HIC value from  $8 \times 10^4$  to  $1.3 \times 10^4$ , while the displacement increases from  $.02(m)$  to  $.04(m)$ . In addition, for higher natural frequencies, the rate of increase in HIC for Case I is far more than that in Case III. This behaviour ensures a safer impact isolator design when the maximum permissible displacement is slightly reduced.

Therefore, the results obtained in Case III can be seen as a significant improvement, especially if there is a constraint on minimum natural frequency of the impacting system in addition to the maximum allowable displacement range.



(a)



(b)

**Figure 2-16. Comparison of impact isolators Case I and Case III, a) maximum displacement vs. frequency, b) HIC vs. frequency**

Eventually, when the desired values for design parameters have been selected, the physical parameters of the impact isolator should be calculated according to Equations (2-18) and (2-23), and the validity of the values should be confirmed for a viable solution.

### 2.2.3.1. Effect of Parameter $\mu_R$

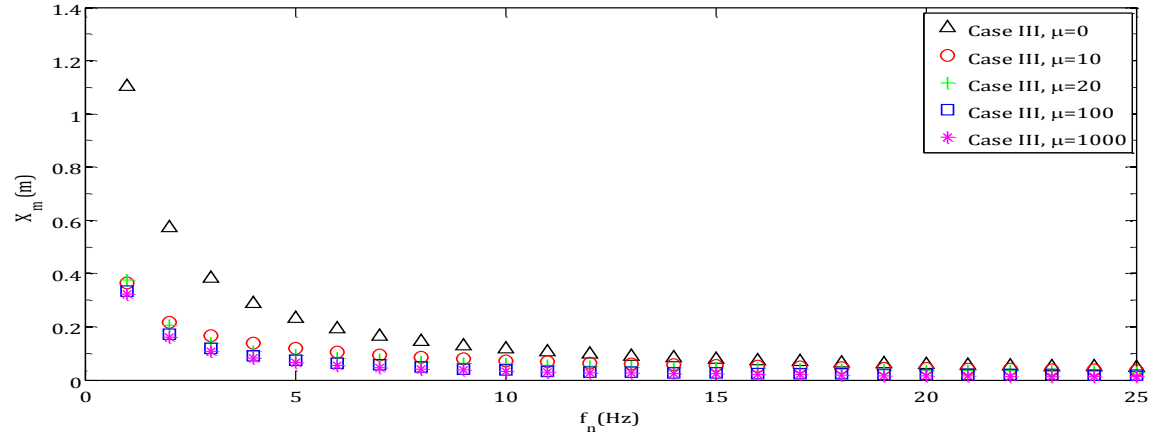
The parameter  $\mu_R$  in Equation (2-22) demonstrates the non-vibratory part of the response to impact input; and similar to parameter  $L_1$  in Case II, it can be tuned independently from  $\omega_n$  and  $\xi$ . The direct effect of parameter  $\mu_R$  on the simulation results can be seen in three distinct ways:

1) For lower range of frequencies, increasing  $\mu_R$  reduces the maximum displacement for a constant natural frequency. However, the rate of decrease in maximum displacement is reduced for higher range of frequencies, and eventually it becomes insensitive to  $\mu_R$  for very high frequencies. Besides, for very low natural frequencies, by increasing  $\mu_R$ , the maximum displacement of the impacting mass in Case III asymptotically approaches the displacement obtained for the same natural frequency from the MSD system discussed as Case I.

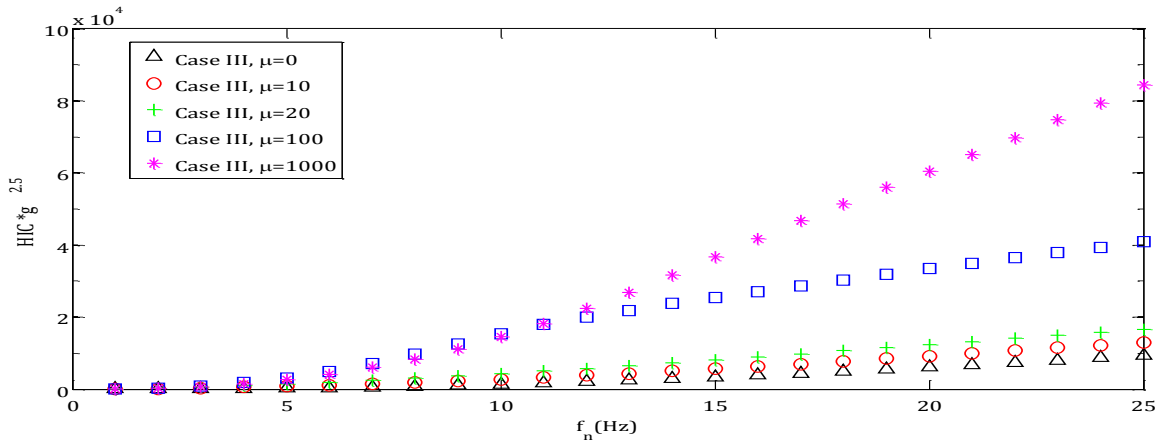
2) For the fixed value of  $\omega_n$ , in the region corresponding to higher frequencies, the HIC value is substantially increased by further increasing the value of parameter  $\mu_R$ , while eventually the change in maximum displacement associated with that frequency can be almost neglected for different values of  $\mu_R$ . Similar to what was discussed in section 2.2.2.2, the optimum value for parameter  $\mu_R$  can be found such that minimal possible HIC is achieved for the whole range of natural frequencies at the expense of negligible changes in maximum displacement experienced by the impacting mass. 3) Finally, as indicated in Figure 2-18, for small values of  $\mu_R$ , the minimal HIC for any  $\omega_n$  is achieved for  $\xi = 1$ , which lies on the upper bound for  $\xi$  parameter. However, as  $\mu_R$  increases, more variation in optimal damping as a function of frequency is observed.

Note again that the deviation in optimal damping values for minimal HIC is more obvious than that for minimal peak acceleration. Apparently, this makes the impact isolator design procedure more complicated due to its higher dependency on the system situation and different parameters. This re-emphasizes that in crashworthiness optimization, the peak acceleration minimization should not be mistakenly used as an indication of HIC minimization. The variation in optimal damping values based on both HIC and peak acceleration is shown in Figure 2-19 for self-damped isolator of Case III when  $\mu_R = 500$ .





(a)



(b)

**Figure 2-17. Effect of parameter  $\mu_R$  for impact isolator Case III, a) displacement comparison , b) HIC comparison**

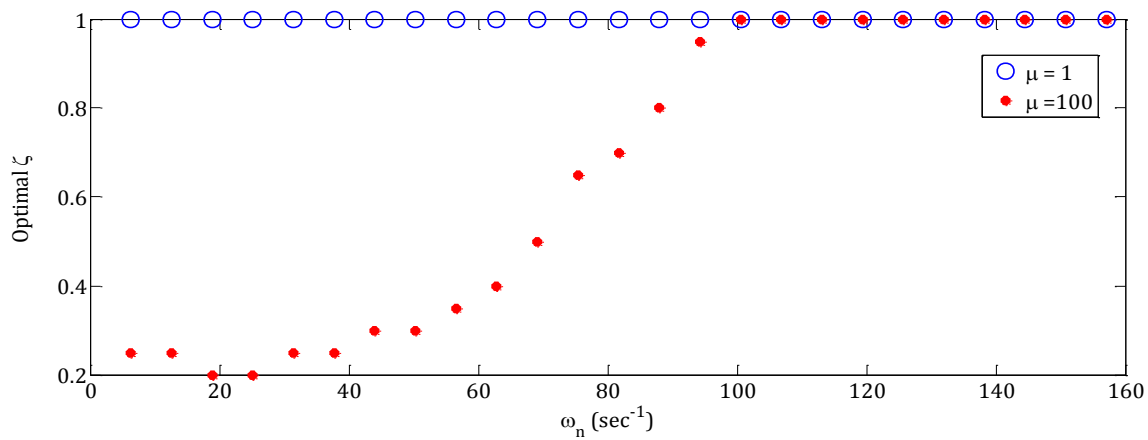


**Figure 2-18. Effect of parameter  $\mu_R$  on optimal damping ratio values for airbag of Case III**

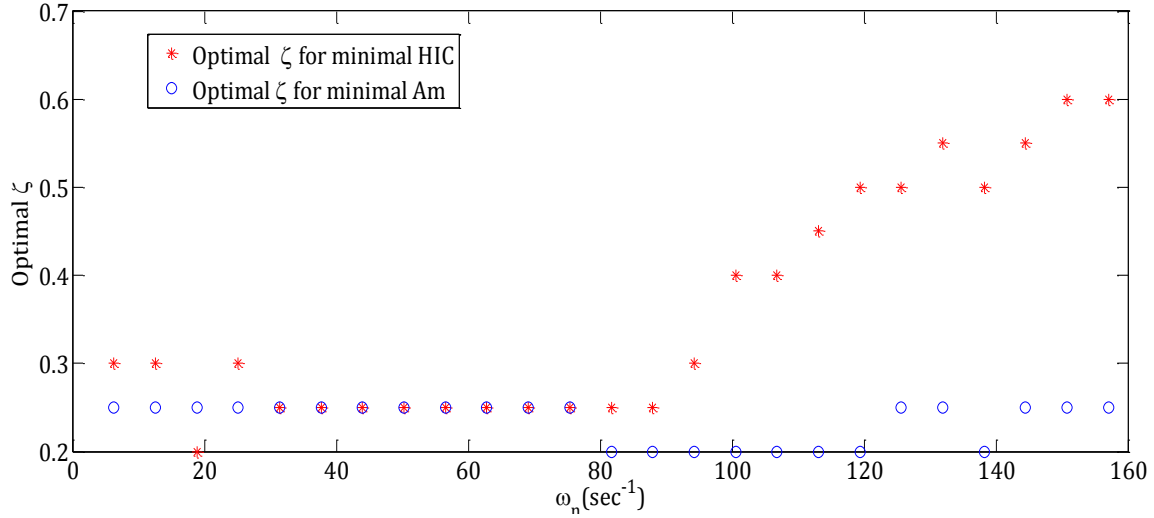


**Figure 2-19. Comparing  $\xi_{optimal}$  values for HIC and peak acceleration for airbag of Case III when  $\mu_R = 500$**

## 2.3. Chapter Summary

In this chapter, the HIC optimization problem was conducted in a single degree-of-freedom passive impact isolator configuration, while the maximum displacement is considered the constraint. To find the schematic isolator design procedure for head injury prevention application, three simplified impact isolator models were examined: 1) simple mass-spring-damper (MSD), 2) gas spring with initial pressure of  $P_0$  in parallel with a dashpot, and 3) gas spring with initial pressure of  $P_0$  and auxiliary reservoir. In each case, the physical parameters of the system were represented in terms of  $\omega_n$  and  $\xi$  as main design parameters. Then the optimal damping for both peak acceleration and HIC, subject to a maximum displacement, was calculated, and the corresponding design graphs were developed for the optimized problem. It was found that the HIC score is increasing monotonically with increasing natural frequency, while maximum displacement is decreasing. Note that in Cases II and III, an additional design parameter independent of  $\omega_n$  and  $\xi$  appears in the governing equations, providing more flexibility for optimizing the performance of the impact isolator system. The best results were obtained from the impact isolator of Case III where, for almost a negligible decrease in maximum displacement, the 80% reduction in HIC was achieved compared with the MSD isolator. Such a substantial improvement occurred due mainly to the optimization flexibility

associated with additional parameter  $\mu_R$  in Case III. However, the physical interpretation of parameter  $\mu_R$  is required to be understood in order to find the optimum design of impact isolator.

### **3. Optimal Impact Attenuator Feasibility by Applying “Effective Operating Region (EOR)” for the Spring Element**

#### **3.1. Introduction**

In the previous chapter, the impact attenuation characteristic of a single degree of freedom was studied. The natural frequency and damping coefficient were selected as the key design parameters to find the optimum HIC subject to the constraint of maximum permissible displacement.

In this chapter, the characteristic of the HIC function is first briefly reviewed and then the several deceleration strategies are investigated to identify an ideal candidate for the HIC optimization problem. Next, the feasibility of creating a system to implement such a deceleration curve by means of springs and dampers is studied. The concept of “Effective Operating Region” is defined as an approach for the optimal impact isolator design for the elastic (spring) component. The use of the new design concept is also illustrated through a few examples.

#### **3.2. Head Injury Criterion Function**

In an impact environment, it is difficult to measure forces and moments. Load cells are generally large and difficult to implement in human impacts. Moreover, they are usually placed between the body and surface, possibly altering the magnitude of the contact force. On the other hand, acceleration of a body segment is relatively easy to

measure. Therefore the accelerometer is a common type of sensor which is instrumented in a dummy's head in crash/drop tests for measuring and analyzing the intensity of impact, and consequently, many isolation performance criteria are defined based on acceleration of the moving head during the impact. Acceleration (deceleration) is the rate at which the speed of motion changes. The greater this rate the higher acceleration (deceleration), and therefore, a more severe injury is expected. Deceleration in the case of a fall can be abrupt; however, energy-absorber mechanisms (such as air bags and other mechanical safety structures) provide a more gradual and smooth deceleration curve. The efficiency of an impact absorber used in head protection is usually assessed by the Head Injury Criterion (HIC), which is defined as,

$$HIC = \left\{ \left[ \frac{1}{t_2 - t_1} \int_{t_1}^{t_2} a(t) dt \right]^{2.5} (t_2 - t_1) \right\}_{max} \quad (3-1)$$

In Equation (3-1) the magnitude of the linear acceleration observed at the head's centre of mass is described by  $a(t)$  (measured in g), while  $t_1$  and  $t_2$  are two time points (measured in seconds) during the impact,  $0 < t_1 < t_2$ . The time interval  $[t_1, t_2]$  is not fixed and is identified as the pair that will maximize the integral function of the acceleration. This time interval is restricted however to a maximum of 15 milliseconds.  $HIC = 1000$  is known as a threshold for fatal head injuries. In the *HIC* optimization problem, usually two different cases are investigated. In the first, minimum head displacement during deceleration is desired, provided that the *HIC* is lower than the threshold by a prescribed value, and vice versa; in the second case, *HIC* is minimized provided that the displacement of the head does not exceed a prescribed maximum allowable quantity. Wu et al. [18] develop optimal control laws corresponding to both cases in the *HIC* optimization problem which will gain the ideal deceleration trend during the impact. Ideal decelerations have infinite values at the instant when impact initially occurs. However, it is generally unrealistic to expect the deceleration curve to show a very sharp rise at the beginning, and therefore, alternative control schemes including constant force and power-law deceleration are considered instead. All *HIC* optimization problems should also consider an additional constraint imposed by a maximum

allowable 3 ms acceleration criterion. This criterion is defined as the maximum acceleration experienced by a head lasting for 3 ms, which, according to the US standard FMVSS No. 201, shall not exceed 80 g's. In the following section, some typical deceleration waveforms are examined and compared in terms of HIC, maximum allowable head displacement, and peak acceleration.

### **3.3. Optimal Impact Waveform and Its Comparison with Other Waveforms**

#### **3.3.1. Optimal Impact Pulse**

As stated previously, the most effective approach for reducing head injury is to reduce the *HIC* score. Before designing the safety device, therefore, the shape of an ideal acceleration curve which minimizes the *HIC* score should be found. The formula shows *HIC* as the average of acceleration over an interval  $t_1 - t_2$  for the head acceleration  $a(t)$ . This leads to the prediction of the two extreme cases that may cause injury: 1) short-duration, high acceleration; and 2) long-duration, low acceleration. However, our numerical analysis shows that the HIC is more sensitive to the acceleration magnitude (it has power of 2.5) than the time duration. Ignoring the constraint imposed by the 3-ms criterion, Wu and Beaudet [18] show that  $a(t) = ct^{-4}$  is the optimal deceleration function resulting in minimum HIC within the allowable range of head displacement. The proposed  $a(t)$  function (Figure 3-1) inherently results in a constant HIC for any interval of  $\Delta T$ . In addition, since the area (or velocity change) under the acceleration curve at any time  $t$  is larger than that under other candidate acceleration curves with a same *HIC*, therefore the head travel associated with the proposed curve is the smallest. They also compare their proposed optimal curve with a square waveform for the acceleration which has the same HIC score; they conclude that, with the square waveform, the head needs 33% more travel space.

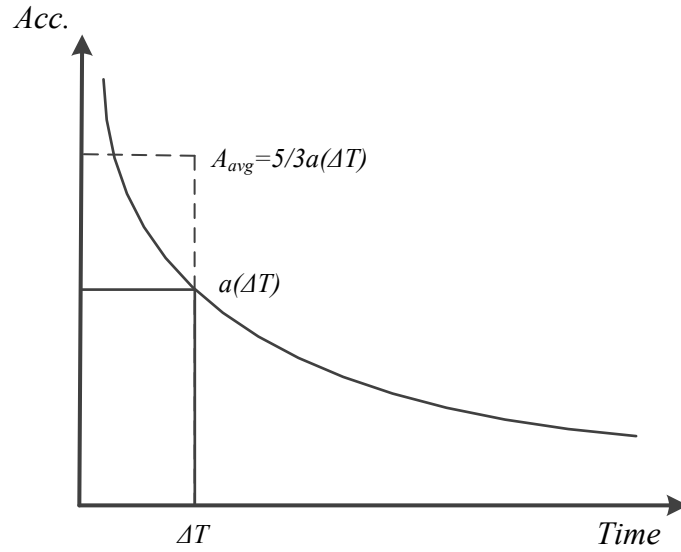


**Figure 3-1. Optimal head impact acceleration for minimal HIC**

In real-life situations, however, the head acceleration cannot be infinite as proposed by the optimal curve, and more importantly, the square waveform is more attractive if the maximum peak acceleration or 3-ms criterion is considered.

### **3.3.2. Other Simplified Waveforms**

For comparison, some other waveforms more likely to be encountered in practice are also examined. In our analysis, for simplicity and comparison it is assumed that impacts have no rebound. Also, for each waveform, peak acceleration and impact duration are such that the total head travel is the same by the end of the impact. The waveforms studied under these conditions are plotted in Figure 3-2, and the governing equations in each case are as follows,

For sine wave,

$$a(t) = A \sin\left(\frac{t}{T} \pi\right) \quad (3-2)$$

$$HIC = .4146 A^{2.5} T$$

$$d = 13.13 \cdot 10^{-3} \frac{v_0^{\frac{2}{3}}}{HIC^{\frac{2}{3}}}$$

$$A_{p\{sine\}} = \pi A_{p\{sw\}}$$

$$T_{\{sine\}} = .5 T_{\{sw\}}$$

$$A_{\{3ms\_sine\}} = \int_{\frac{T_{\{sine\}}}{2} - 1.5 \cdot 10^{-3}}^{\frac{T_{\{sine\}}}{2} + 1.5 \cdot 10^{-3}} a(t) dt$$

For haversine wave,

$$a(t) = \frac{A}{2} \left( 1 - \cos \left( \frac{2\pi}{T} t \right) \right) \quad (3-3)$$

$$HIC = .3029 A^{2.5} T$$

$$d = 15.92 \cdot 10^{-3} \frac{v_0^{\frac{2}{3}}}{HIC^{\frac{2}{3}}}$$

$$A_{p\{hsine\}} = 2 A_{p\{sw\}}$$



$$T_{\{hsine\}} = T_{\{sw\}}$$

$$A_{\{3ms\_hsine\}} = \int_{\frac{T_{\{hsine\}}}{2} - 1.5 \cdot 10^{-3}}^{\frac{T_{\{hsine\}}}{2} + 1.5 \cdot 10^{-3}} a(t) dt$$

For isosceles triangle waveform with peak acceleration  $A$  and duration  $\Delta T$ ,

$$a(t) = \begin{cases} \frac{2A}{T} t, & 0 < t < \frac{T}{2} \\ 2A - \frac{2A}{T} t, & \frac{T}{2} < t < T \end{cases} \quad (3-4)$$

$$HIC = .2464 A^{2.5} T$$

$$d = 13.87 \cdot 10^{-3} \frac{v_0^{\frac{2}{3}}}{HIC^{\frac{2}{3}}}$$

$$A_{p\{tr\}} = 2A_{p\{sw\}}$$

$$T_{\{tr\}} = T_{\{sw\}}$$

$$A_{\{3ms\_tr\}} = \int_{\frac{T_{\{tr\}}}{2} - 1.5 \cdot 10^{-3}}^{\frac{T_{\{tr\}}}{2} + 1.5 \cdot 10^{-3}} a(t) dt$$

For ramp-down wave,

$$a(t) = A - \frac{A}{T}t \quad (3-5)$$

$$HIC = .2464 A^{2.5} T$$

$$d = 9.247 \cdot 10^{-3} \frac{v_0^{\frac{2}{3}}}{HIC^{\frac{2}{3}}}$$

$$A_{p\{rd\}} = \frac{4}{3} A_{p\{sw\}}$$

$$T_{\{rd\}} = \frac{3}{2} T_{\{sw\}}$$

$$A_{\{3ms_{rd}\}} = \int_0^{3 \cdot 10^{-3}} a(t) dt$$

For ramp-up wave,

$$a(t) = \frac{A}{T}t \quad (3-6)$$

$$HIC = .2464 A^{2.5} T$$

$$d = 18.49 \cdot 10^{-3} \frac{v_0^{\frac{2}{3}}}{HIC^{\frac{2}{3}}}$$

$$A_{p\{ru\}} = \frac{8}{3} A_{p\{sw\}}$$

$$T_{\{ru\}} = \frac{3}{4} T_{\{sw\}}$$

$$A_{\{3ms_{ru}\}} = \int_{T_{\{ru\}} - 3 \cdot 10^{-3}}^{T_{\{ru\}}} a(t) dt$$

For square wave,

$$a(t) = A \quad (3-7)$$

$$HIC = A^{2.5} T$$

$$d = 11.12 \cdot 10^{-3} \frac{v_0^{\frac{2}{3}}}{HIC^{\frac{2}{3}}}$$

$$A_{\{3ms_{sw}\}} = A$$

and for optimal wave proposed in [18],

$$a(t) = .6 \left( \frac{HIC}{t} \right)^{.4} \quad (3-8)$$

$$d = 8.342 \cdot 10^{-3} \frac{v_0^{\frac{2}{3}}}{HIC^{\frac{2}{3}}}$$

where

$$A_{p\{sw\}} = \frac{v_0^2}{2d_{max}} \quad (3-9)$$

$$T_{\{sw\}} = \frac{2d_{max}}{v_0}$$

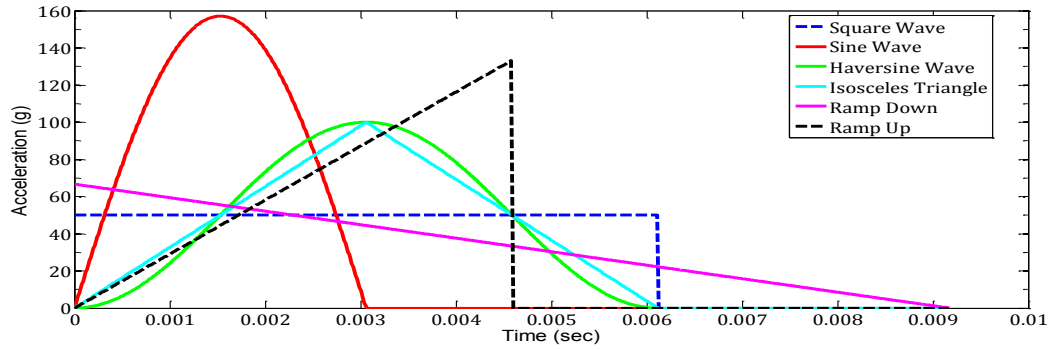
Taking  $A_{\{3ms\}}$  into account as a critical design constraint for head impact, the waveform efficiency is defined as the combination of the HIC and peak acceleration under a similar impact velocity and with a similar head travel ( $d_{max}$ ),

$$Efficiency = \frac{2}{\left(\frac{1}{Eff_{HIC}}\right)^2 + \left(\frac{1}{Eff_{A_p}}\right)^2} \quad (3-10)$$

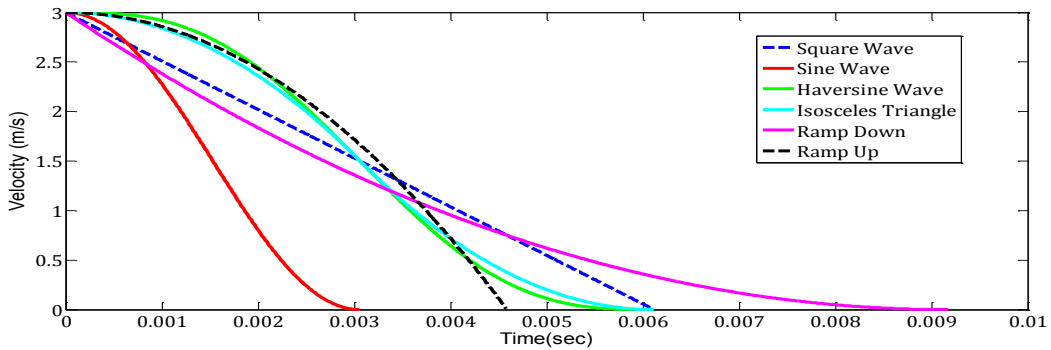
where  $Eff_{HIC} = HIC/HIC_{sw}$  and  $Eff_{A_p} = A_p/A_{p_{sw}}$  for each waveform.

This criterion makes more sense because it is important to find the least HIC that occurs when both the peak acceleration and maximum allowable displacement do not exceed limits. With this definition, if two wave forms for the same impact velocity result in the same  $d_{max}$ , then that with the smaller combined  $HIC$  and  $A_p$  ratio is said to be more efficient. To be more precise,  $A_p$  in Equation (3-10) should be replaced by the corresponding  $A_{\{3ms\}}$ . For waveforms studied here, however, assuming  $T \gg 3ms$  for each waveform, the peak acceleration value can be simply used instead of  $A_{\{3ms\}}$ . The ratio defined here can be calculated using Equation (3-10) and by substituting  $HIC$  and  $A_p$ . The efficiency of the waveforms is calculated relative to that of the square waveform

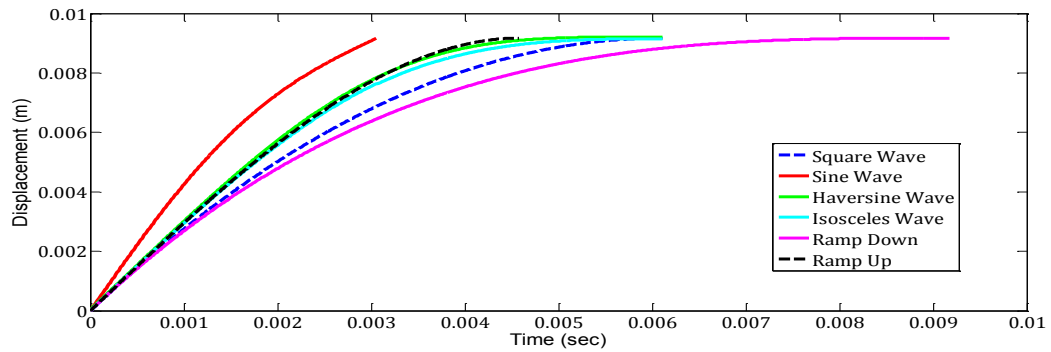
using Equations (3-2) through (3-9), which is listed in Table 3-1 and also shown graphically in Figure 3-3.



(a)



(b)



(c)

**Figure 3-2. Comparison of head impact waveforms with  $v_0 = 3 \frac{m}{s}$ ; a) acceleration, b) velocity, c) displacement**

**Table 3-1. Comparison of Waveforms efficiency with respect to square waveform**

Impact Waveforms	$Eff_{HIC}$	$Eff_{A_p}$	Efficiency
Square	1	1	100%
Ramp-down triangle	1.31	.75	85%
Isosceles triangle	.72	.5	34%
Haversine	.584	.5	29%
Sine	.78	.32	17.5%
Ramp_up triangle	.467	.375	17%

In Figure 3-4 the  $HIC$  versus peak accelerations for the five waveforms of Figure 3-2(a) are shown under the same impact situation. It is clear that with a similar  $HIC$ , the square pulse would have less peak acceleration than for other waveforms. In Figure 3-4(b), when the  $HIC$  is plotted against  $A_{\{3ms\}}$ , instead of peak acceleration there is a slight shift in the order of other waveforms, but the square wave still has the least  $A_{\{3ms\}}$ . This indicates that the square wave is the correct choice for minimum  $HIC$  when  $A_{\{3ms\}}$  limitation is also considered.

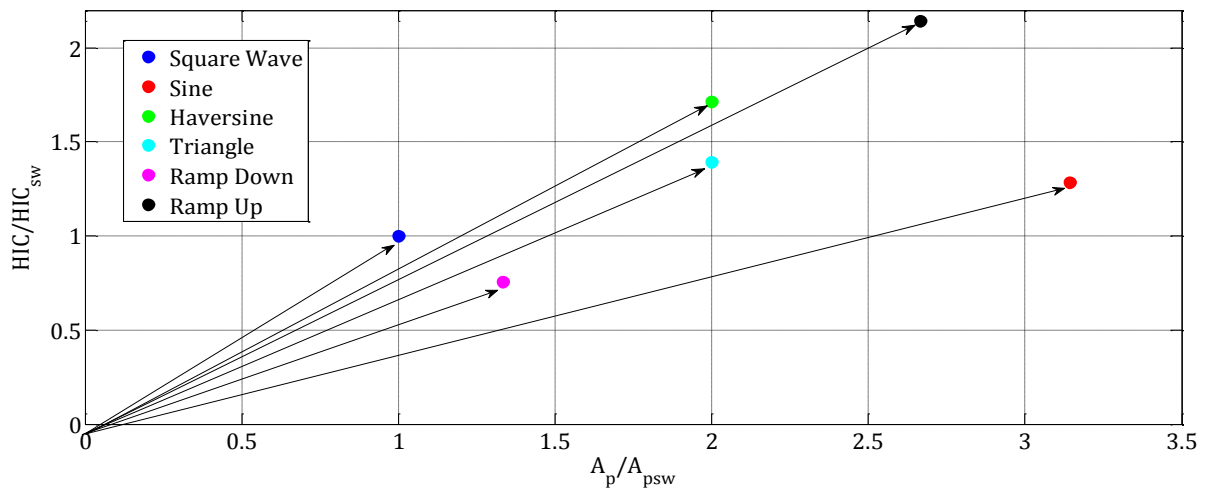
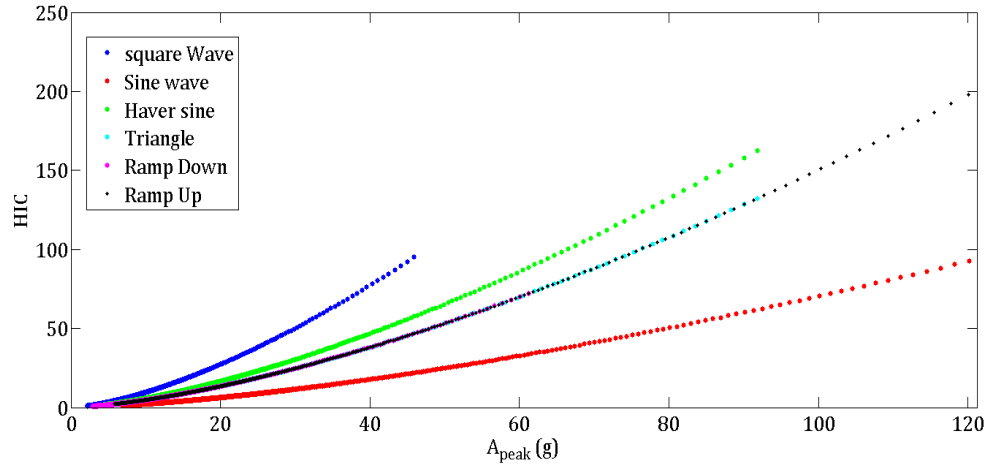
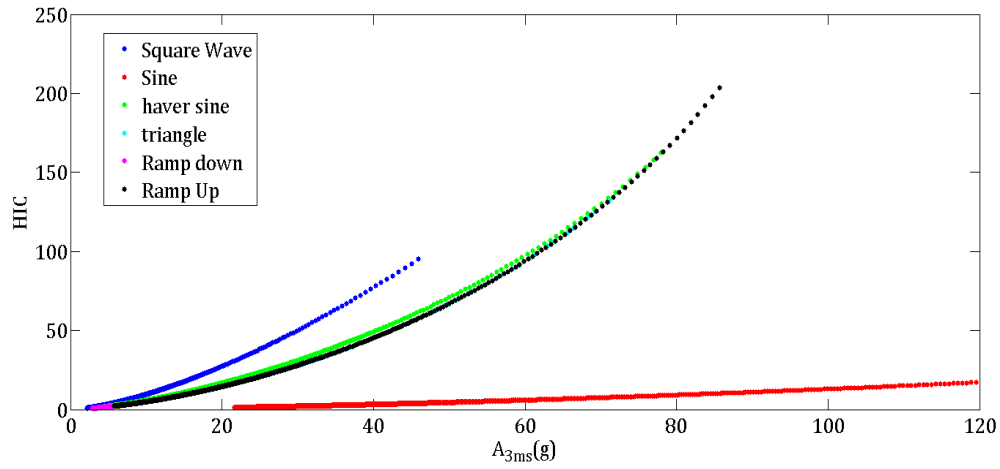


**Figure 3-3. Comparison of  $Eff_{HIC}$  and  $Eff_{A_p}$  for different waveforms**



(a)



(b)

**Figure 3-4. HIC vs. Acceleration for different waveforms with  $v_0 = 3 \text{ m/s}$ ; a) peak acceleration, b) 3 ms Acceleration**

Finally, considering the HIC optimization as tuning of the design variables problem for a given maximum space and  $A_{\{3ms\}}$ , the efficiency of each waveform can be better illustrated by Figure 3-5. In this figure,  $d^*$  represents the minimum displacement where the associated waveform meets the  $A_{\{3ms\}}$  criterion (for  $d < d^*$  there is no valid

point for that waveform to meet problem constraints). In other words, instead of using Equation (3-10) to find the efficiency of a specific waveform, the discretized-type efficiency of each waveform is defined. Given this definition, the efficiency of the waveform is zero if  $A_{\{3ms\}}$  constraint is not satisfied ( $d < d^*$ ), and it is equal to  $Eff_{HIC}$  in Table 3-1 if  $d > d^*$ . In fact, this definition of efficiency of an impact pulse is more logical because it ignores the displacement ranges that the problem has no valid solution. It is clear that the square wave has the minimum  $d^*$  value since it has a lower level of peak acceleration for a certain displacement than other forms. However, according to this new definition, the efficiency of some waveforms could be greater than that of square wave if a higher maximum displacement is permitted. Square wave can, however, still be considered as the most efficient waveform because lower displacement for the safety devices is generally preferred.

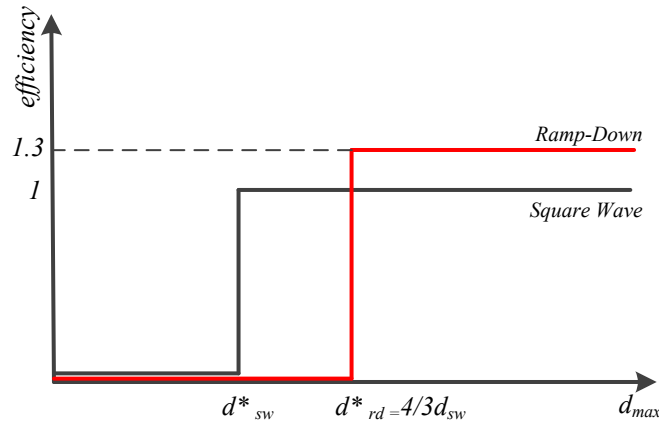


**Figure 3-5.** *Discretized-type of waveform efficiency for impact attenuation. Black line corresponds to square wave and red line corresponds to ramp-down waveform*

### 3.4. Feasibility of Optimal Deceleration Curve (constant acceleration) using Passive Spring Elements

As stated previously, the square wave deceleration is the most effective waveform for the HIC optimization problem. The practicality of developing a system that can generate this waveform during the impact using passive spring elements will be



discussed in the following sections. To achieve this, the concept of "Effective Operating Region (EOR)" for a spring element is introduced and analytically demonstrated. Some feasible examples are also provided to illustrate this concept.

### 3.4.1. *Effective Operating Region (EOR) of a Spring*

Before introducing the EOR concept for a spring, it is useful to relate a system's energy to HIC. For this purpose, consider a single degree-of-freedom, mass-spring system as shown in Figure 3-6. Upon impact, the differential equation of motion and the total energy of the system at any instant  $t$  are given as:

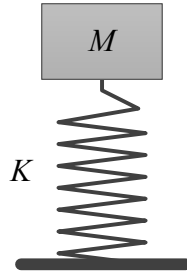


**Figure 3-6. Single degree of freedom mass spring system**

$$m\ddot{x} + F(x) = 0 \quad (3-11)$$

$$E_{system} = E_{kinetic} + E_{potential} \quad (3-12)$$

As the upward force applied to the body by the spring increases, the kinetic energy reduces until the mass comes to a complete stop. Due to the conservation of energy, the kinetic energy converts to potential energy such that the total system's energy remains constant. According to the potential energy definition, the rate of change in potential energy stored in the spring (elastic component) is directly related to the force applied to the body by the spring within a certain range of motion (potential energy is the area under force-displacement curve),

$$E_p = \int F(x)dx \rightarrow F = \frac{dE_p}{dx} \quad (3-13)$$

In the simple case of a linear spring, as the rate of potential energy changes of the elastic element (called “potential element” during this study) increases, more resistance (force) from the spring (potential element) is applied to the head mass. In fact, the rate of potential energy stored in the system is proportional to the force applied, and based on Equations (3-11) and (3-13), even a small variation in that produces an instantaneous effect on the force (acceleration) transmitted to the body. As discussed in the previous section, with the aim of having maximum energy absorbed within the specific range of motion, the constant deceleration curve was shown to be the most effective for obtaining minimum HIC and  $A_{\{3ms\}}$  while meeting the other design limitations. In Figure 3-8, the optimum value for constant force for a certain impact energy is shown by  $f^*$  under the circumstance that the system comes to a complete stop at  $d_{max}$ . Any value greater or smaller than  $f^*$  is not the ideal choice since in the former case the higher HIC and  $A_{\{3ms\}}$  values are the result, while in the latter case not enough energy is absorbed by the time it reaches  $d_{max}$ . With this in mind, one might conclude that it would be ideal for the spring force to have the least possible deviation from  $f^*$  provided that it guarantees enough energy absorption in that specific region (that is, maximum possible energy absorption). Therefore, the “Effective Operating Region” or EOR for such a spring can be defined as,

$$EOR = \left\{ \frac{\int_{x_1}^{x_2} (f(x) - f^*(x))^2 dx}{\int_{x_1}^{x_2} f(x) dx} \right\}^{min} \quad (3-14)$$

where  $x_1$  and  $x_2$  are any displacement points on the force-displacement graph of the spring, and the interval  $[x_1, x_2]$  is searched to minimize the EOR value in Equation (3-14). Fundamentally, the EOR value for an interval of  $[x_1, x_2]$  measures the closeness of the spring force to the ideal value  $f^*$  while assuring the maximum possible energy absorption by the spring. After finding the optimum range for EOR score, it would be more efficient if

the spring element could release any excessive potential energy at the appropriate instant in order to remain within the Effective Operating Region that results in minimum HIC and maximum possible energy absorption (partly energy dissipation). This potential energy release is schematically illustrated in Figure 3-7. In this design, the bottom end of the spring is connected to a plate and has the chance to move till the next step underneath after it reaches a certain amount of force required to break the first step. In this way, the spring releases the excessive potential energy (by breaking the steps) in order to always deform in its effective region without going to high-level force regimes. In fact, such a system is piecewise linear in any segment but not in the whole range of motions. Also, giving the spring an initial displacement to provide adequate preload, the system would have sufficient  $E_0$  (initial potential energy) to be adequately close to the described region as the impact is occurring. It is also important to note that the distance between two successive steps, designated by  $x_{s2}$ , can impose a restriction on the minimum operating clearance for the spring because it might not be physically feasible to have the steps extremely close to each other. Therefore, Equation (3-14) for EOR evaluation can be modified to

$$EWR = \left\{ \frac{\int_{x_1}^{x_2} (f(x) - f^*(x))^2 dx}{\int_{x_1}^{x_2} f(x) dx} \right\}_{min} \quad (3-15)$$

subject to

$$x_2 - x_1 > x_{smin}$$

where the  $[x_1, x_2]$  is searched to minimize the EOR for  $x_2 - x_1 > x_{s2}$ . The latter form of Equation (3-15) is very similar to the HIC formula, where the time interval  $[t_1, t_2]$  was found to maximize the HIC value upon the restriction  $t_2 - t_1 < 15$  ms.

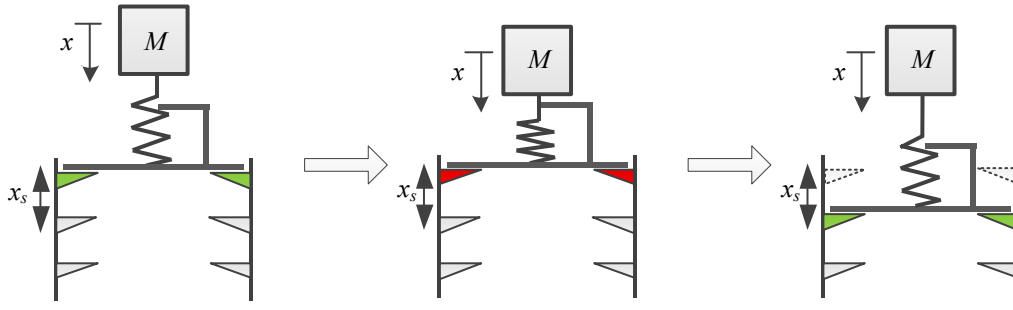


**Figure 3-7. Schematic design applying Effective Operating Region of a spring during impact absorption**

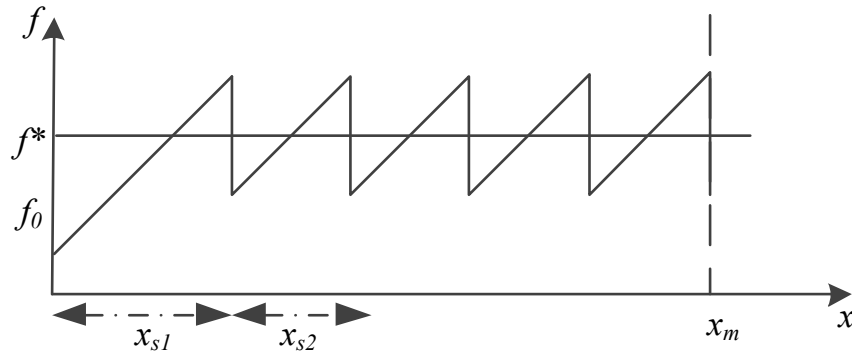


**Figure 3-8. Force-displacement curve for a linear spring with initial pre-load and operating in its effective region ( $x_{s2} = x_s$  in Figure 3-7)**

Once the minimum clearance associated with the design limitations is known, the concept of EOR can be further adopted to any nonlinear springs, as seen in Figure 3-9, by seeking the proper preload value (the initial point of effective region on the force-displacement curve) and opting for an appropriate range that shall be greater than the minimum specified clearance  $x_s$  for the spring.

### **3.4.2. HIC Minimization Subject to a Maximum Displacement $d_{max}$ for a Gas-spring System Applying EOR**

One practical example of a spring to implement the effective operating region concept for enhanced impact isolation is the gas spring system described in Chapter 2.

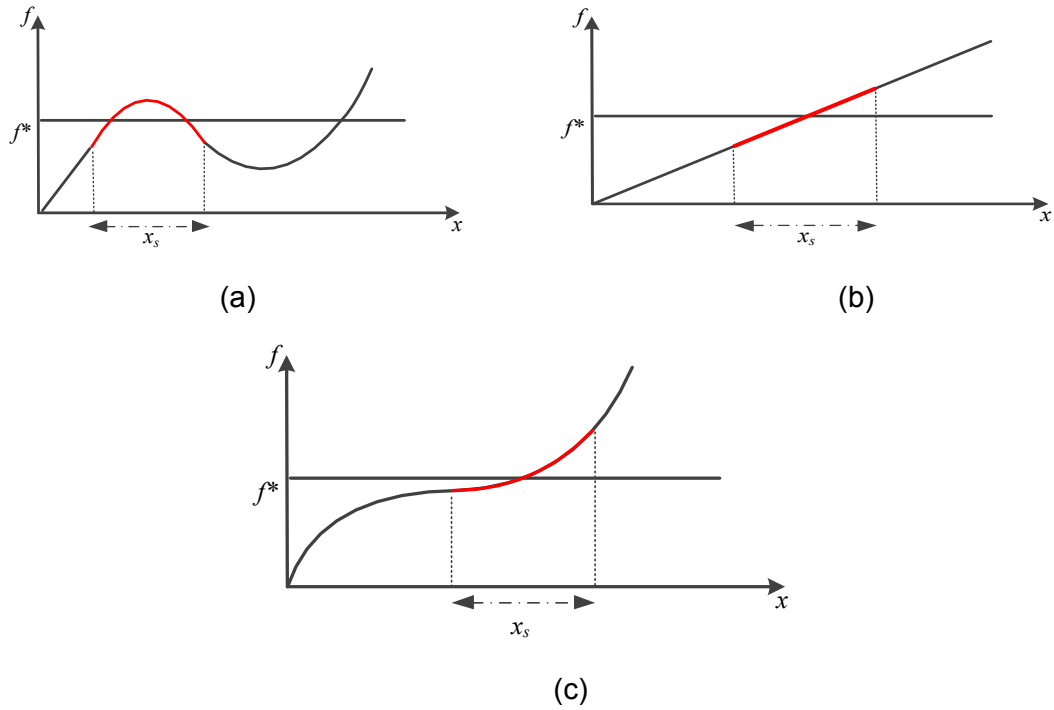


**Figure 3-9. Schematic display of effective operating region of different types of springs subject to minimal distance of  $x_s$**

The gas spring includes a piston moving inside a cylinder, with initial pressure of  $p_0$  and initial length of  $L_0$  and with the force applied to the mass proportional to the changes in internal pressure – which can be assumed to go through an adiabatic process during the impact. To manage effectively the gas spring potential energy so as to keep it within its EOR, a pressure relief valve can be designed and placed at the venting outlet. By defining the HIC optimization problem, therefore, and determining the ideal  $p^*$  associated with ideal  $f^*$ ,  $P_{burst}$  at which the valve opens can be set. As soon as the pressure exceeds this value, the excessive potential energy is discharged through mass flow of pressurized air to the atmosphere. This pressurized air usually has very high internal energy such that even a small mass of it contains enough energy to be removed from the system. One difference between the gas spring system and the piecewise linear spring (Figure 3-8) is that the force transition at the moment of energy release does not occur instantaneously but depends on the valve (orifice) sectional area, which determines the exhausting capacity of the valve. As a matter of fact, in a gas spring with venting, one might expect a gradual decrease in pressure rather than the immediate

drop, an issue shown schematically in Figure 3-10. Moreover, every time potential energy is released (by the end of each segment), the spring becomes stiffer. This is mainly because the initial pressure increases and the initial length decreases at the new state, so they both contribute to the increase in spring rate (Equation (2-14) ). The stiffness of the gas spring with this design asymptotically goes to infinity as the piston reaches the end-stroke, but it can be assumed that by then, the whole impact energy is absorbed.

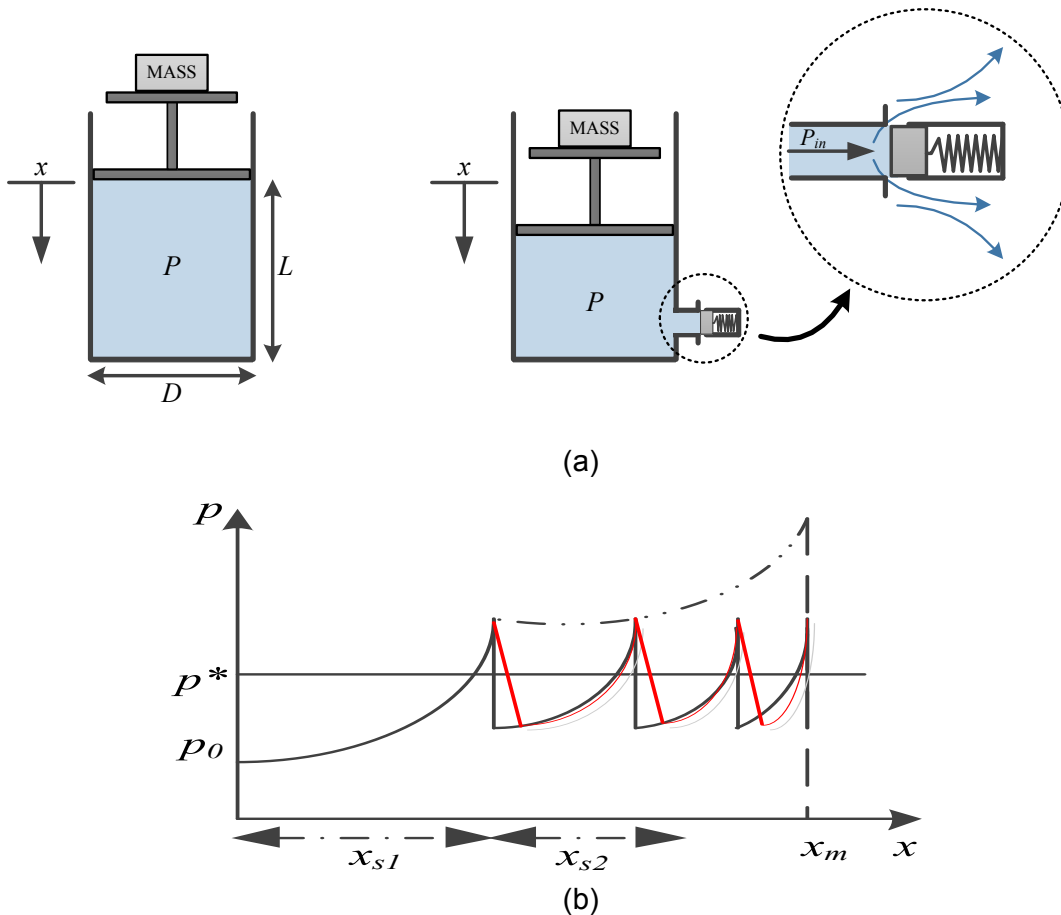


**Figure 3-10. Schematic display of applying effective operating region for a gas spring a) implementation of a pressure relief valve b) pressure change within gas spring during the impact. — corresponds to sufficiently large size valve, - - corresponds to medium size valve, . . corresponds to small valve.**

### 3.4.3. **HIC Minimization Subject to a Maximum Displacement $d_{max}$ for a Mass-spring System with Linear Spring Applying EOR**

Consider the simple mass-spring system shown in Figure 3-6 such that for the specified  $d_{max}$ , the spring with stiffness  $k_0$  can absorb the whole impact energy (that is,  $\frac{1}{2}K_0d_{max}^2 = \text{Impact Energy}$ ). Findings in Chapter 2 show that by reducing the stiffness below  $k_0$ , the spring needs more displacement than  $d_{max}$  to absorb the same impact energy, while increasing the stiffness above  $k_0$ , results in higher values of HIC, which is not desired. However, by applying the EOR concept for the linear spring, a proper preload can be applied such that the spring deforms within its most effective operating region and, therefore, lower values of HIC are achieved. To find the optimum preload, Equation (3-15) can be used as:

$$EOR = \left\{ \frac{\int_0^{x_m} (F_0 + kx - f^*(x))^2 dx}{\int_0^{x_m} (F_0 + kx) dx} \right\}_{min} \quad (3-16)$$

where  $f^* = k_0 * \frac{d_{max}}{2}$ ,  $f = f_0 + k * x$ , and  $x_m$  is the maximum displacement ( $x_m \leq d_{max}$ ), and is calculated from the following energy equation:

$$\int_0^{x_m} (F_0 + kx) dx = F_0 x_m + \frac{1}{2} k x_m^2 = f^* x_m \quad (3-17)$$

In this case study the whole impact energy is supposed to be absorbed during *one segment of energy absorption* rather than during the multi-stage energy release depicted in Figure 3-7. By taking the derivative with respect to  $f_0$  and  $k$ , Equations (3-18) to (3-20) are obtained to find the relation between the optimum preload and stiffness  $k$ .

$$H = \int_0^{x_m} (F_0 + kx - f^*(x))^2 dx = (F_0 - f^*)^2 x_m + \frac{1}{3} k^2 x_m^3 + (F_0 - f^*) k x_m^2 \quad (3-18)$$

$$\frac{\partial H}{\partial F_0} = 0 \xrightarrow{\text{yields}} 2(F_0 - f^*) + kx_m = 0 \quad (3-19)$$

$$\frac{\partial H}{\partial k} = 0 \xrightarrow{\text{yields}} \frac{2}{3}x_mk + (F_0 - f^*) = 0 \quad (3-20)$$

If there is a lower/upper bound to limit the minimum/maximum stiffness of available springs, the optimization problem is treated as a constrained-type problem rather than an unconstrained problem, an issue discussed in optimization textbooks [36].

Solving Equations (3-18) to (3-20) for a maximum displacement of  $d_{max}=16\text{cm}$  and initial velocity of  $v_0= 3 \text{ m/s}$  yields the following optimum results for the impact isolator,

$$K_{opt} = 0$$

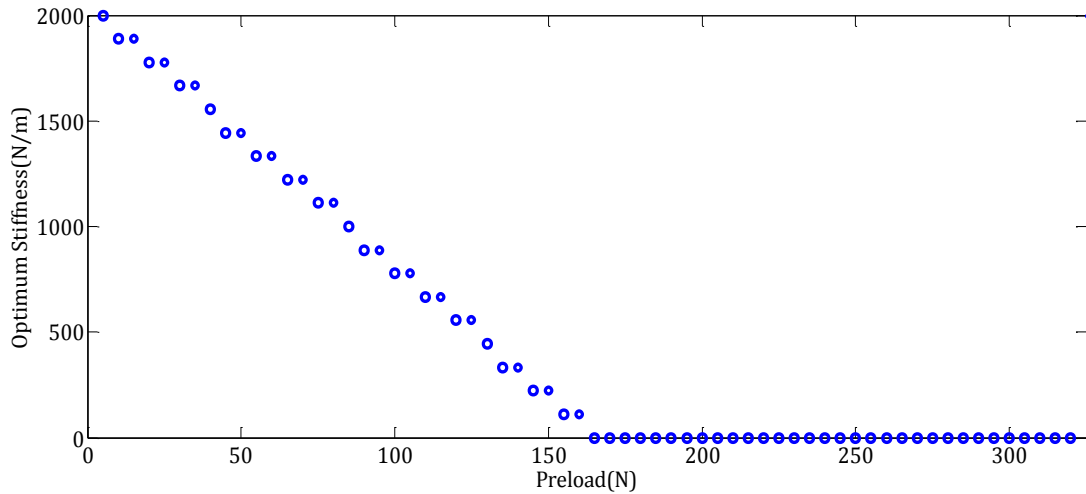
$$f_{0opt} = f^* = 161.6$$

$$HIC_{opt} = 61$$

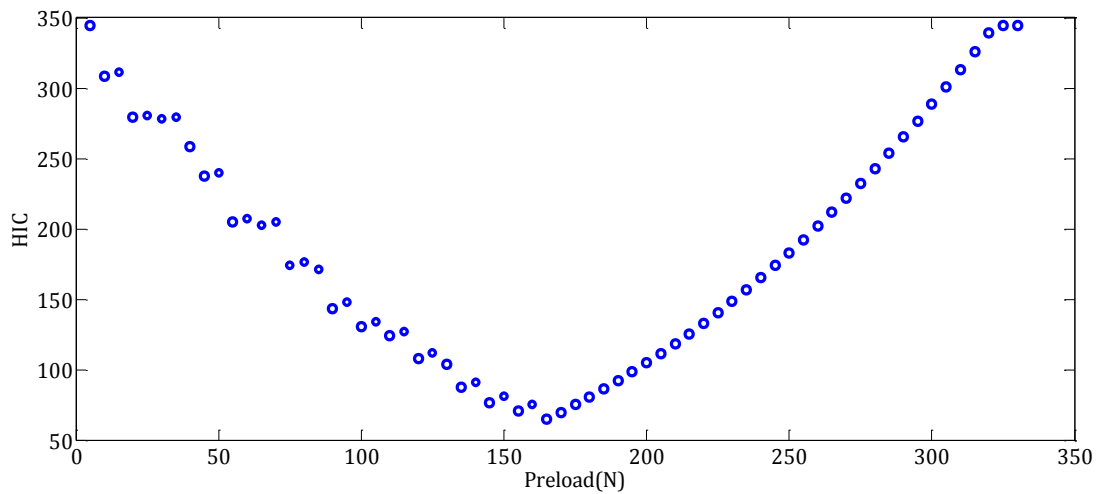
The results from Equations (3-18) to (3-20) are shown in Figure 3-11, where the spring stiffness versus its corresponding optimum preload ( $f_0$ ) is plotted. As the figure shows, if the stiffness decreases, the optimum preload increases to ensure that sufficient energy absorption is accomplished with the least possible deviation from  $f^*$ . The decrease in stiffness will continue until the optimum preload is equivalent to  $f^*$ , the point at which no change in the force would be perfect. This implies zero stiffness of the spring, and it culminates in the minimum HIC value as shown in Figure 3-12 which is the expected outcome (square wave form for acceleration/force). Above this point, further increasing  $f_0$ (denoting preload) results in more deviation from  $f^*$ , increasing in turn the HIC value up to the point where the score is higher than the initial value obtained by spring  $k_0$  without preload.



Figure 3-13 plots the  $HIC$  scores for any spring rate at different preloads. The figure demonstrates that although many combinations of preloads can result in acceptable  $HIC$ , there exists a minimum for each spring rate that minimizes  $HIC$ . Again, this highlights the fact that when the spring is in its effective operating region, we can lower the  $HIC$  values.



**Figure 3-11. Optimum stiffness vs. Preload value for minimal  $HIC$ ,  $v_0 = 3 \text{ m/s}$ ,  $d_{max} = 16 \text{ cm}$**



**Figure 3-12. Optimum  $HIC$  scores for various preload values,  $v_0 = 3 \text{ m/s}$ ,  $d_{max} = 16 \text{ cm}$**

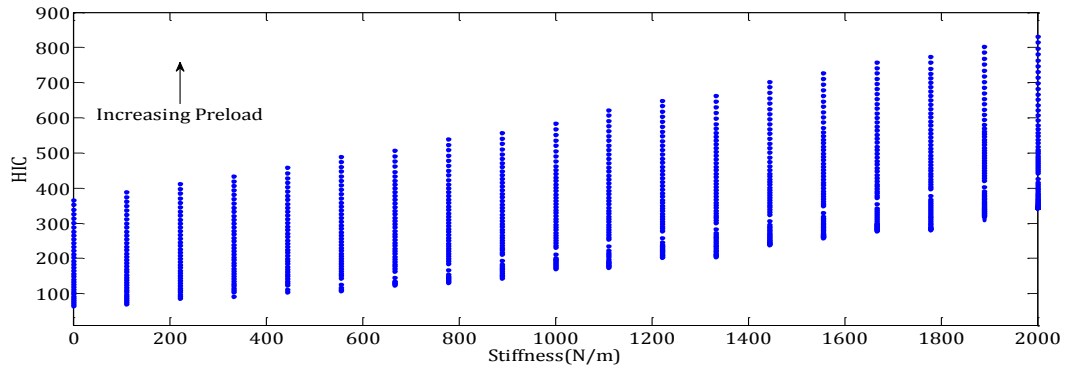


**Figure 3-13. Optimum HIC vs. Stiffness for different preloads,  $v_0 = 3 \text{ m/s}$ ,  $d_{max} = 16 \text{ cm}$**

Figure 3-14 shows the *HIC* values against maximum displacement for any combination of stiffness and its corresponding preload. This plot can be used as a design chart that applies the *EOR* concept for an optimum spring that minimizes the *HIC* for a specific maximum displacement for a single mass-spring system.

Finally, it should be mentioned again that in this case the spring was aimed to absorb the whole impact energy in only one shot. The *EOR* could be different (and more efficient) if energy absorption was allowed to occur in multiple stages (that is, potential energy releasing was allowed in multiple segment design) like the design illustrated in Figure 3-7.

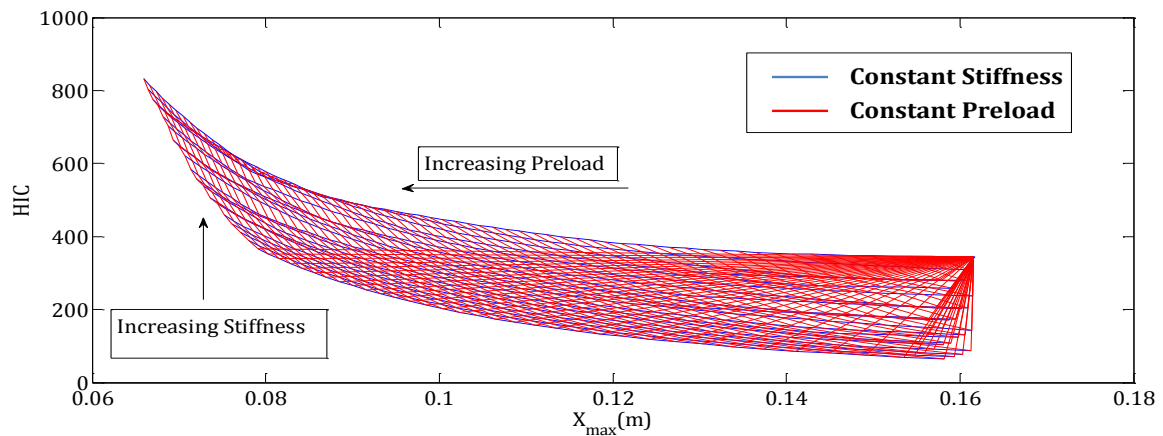


**Figure 3-14. Optimum HIC vs. Maximum displacement for different stiffness and preload values,  $v_0 = 3 \text{ m/s}$ ,  $d_{max} = 16 \text{ cm}$**

### 3.4.4. Effect of EOR on a Linear Spring

Table 3-2 compares the optimum values for damping and stiffness obtained for the case study examined in section 3.4.3. For this purpose, four different configurations are considered: a) spring without applying *EOR*, b) spring-damper without applying *EOR*, c) spring with preload (applying *EOR* concept), and d) combination of a damper and spring with preload. The optimization problem is solved for  $d_{max} < 16$  cm as maximum displacement, and the *HIC* is chosen as the objective function. The Genetic Algorithm optimization toolbox in MATLAB is used as a solver. The convergence history plots obtained by GA are shown in Figure 3-15 through Figure 3-18 for each case of interest.

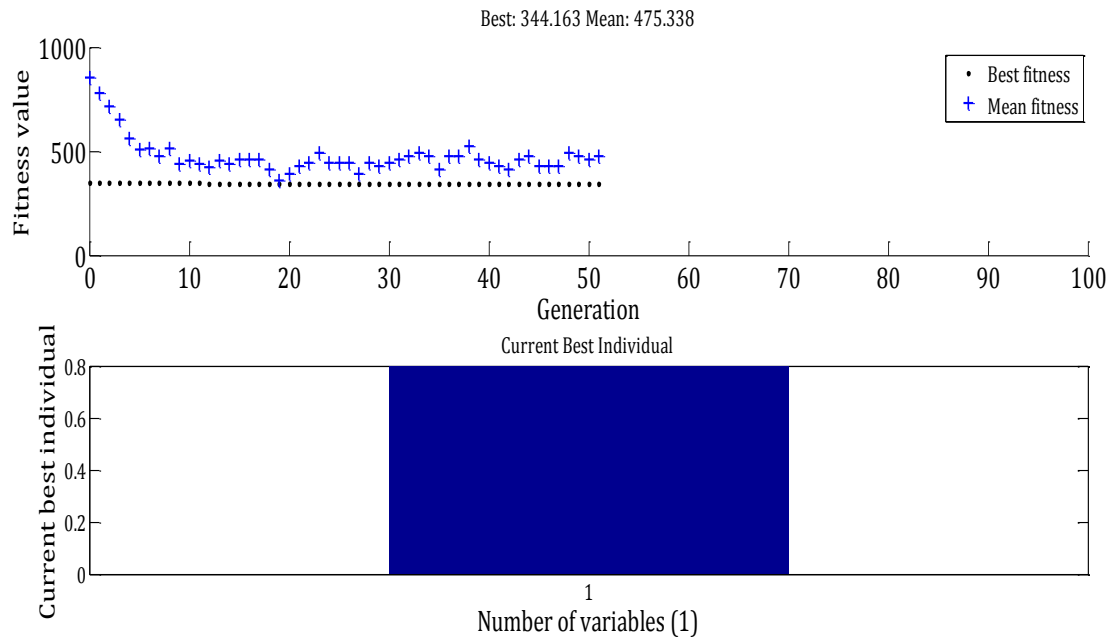


**Figure 3-15. Convergence history in GA for case of linear spring (no Preload),  $v_0 = 3$  m/s ,  $d_{max} = 16$  cm**

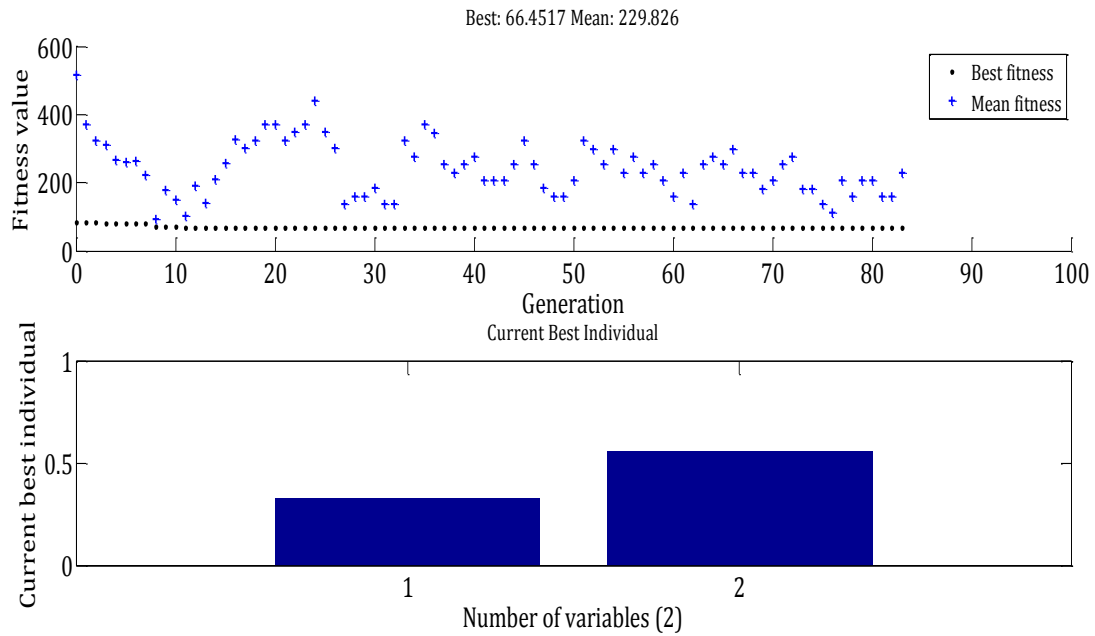


**Figure 3-16. Convergence history in GA for case of linear spring-damper (no preload),  $v_0 = 3 \text{ m/s}$ ,  $d_{max} = 16 \text{ cm}$**

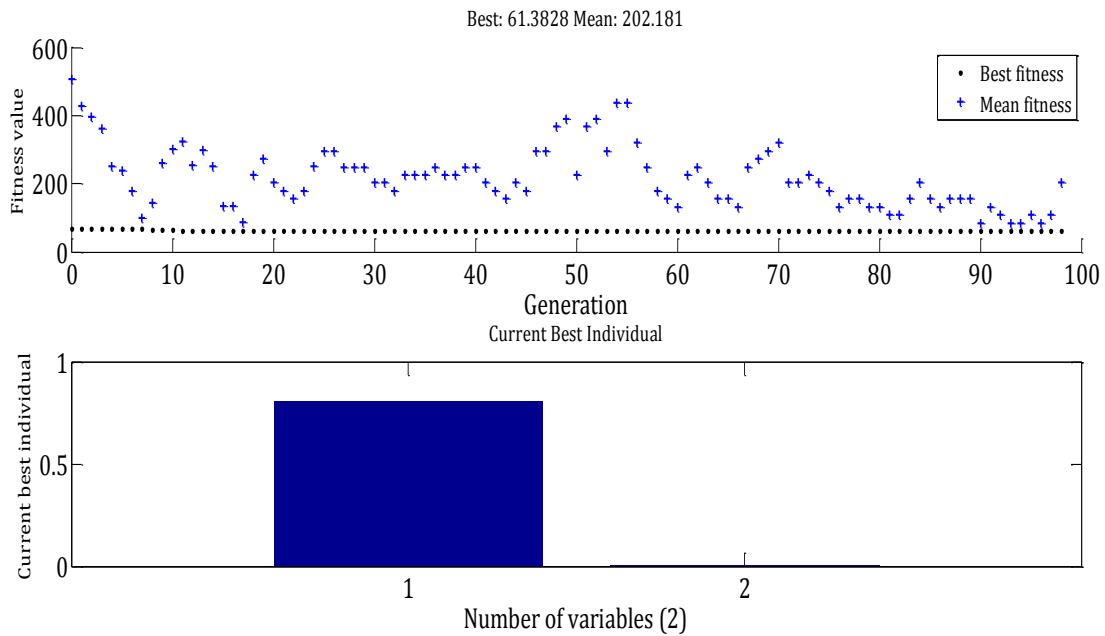


**Figure 3-17. Convergence history in GA for case of linear spring (with preload),  $v_0 = 3 \text{ m/s}$ ,  $d_{max} = 16 \text{ cm}$**

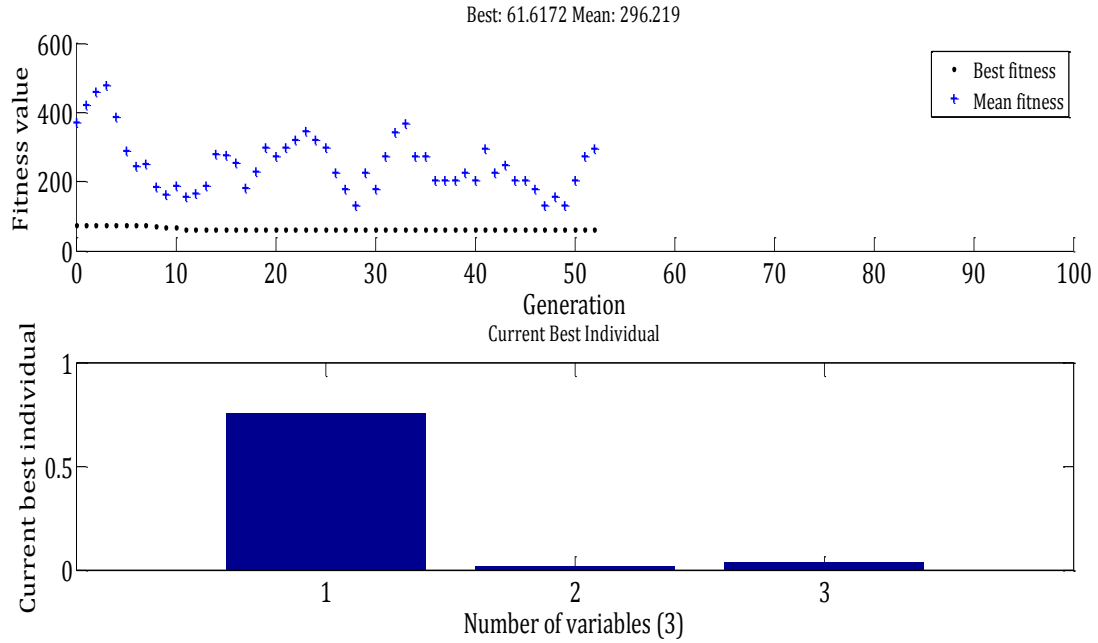


**Figure 3-18. Convergence history in GA for case of linear spring-damper (with preload),  $v_0 = 3 \text{ m/s}$ ,  $d_{max} = 16 \text{ cm}$**

**Table 3-2: Comparing optimum HIC scores for different combination of linear spring-damper with/without preload**

Impact Absorber	$F_{0_{opt}}$	$K_{opt}(\text{N/m})$	$C_{opt}(\text{N.s/m})$	$HIC_{opt}$
Linear spring (no Preload)	0	2000	0	344.16
Linear spring-damper (no preload)	0	660	55.4	66.45
Linear spring (with preload)	161.6	0	0	61.3
Linear spring-damper (with preload)	150.6	32	4.1	61.6

Table 3-2 indicates that, theoretically, the optimal impact attenuation can be achieved by using just one spring in its effective region. Interestingly, in case (d), where the combination of the spring and dashpot with preload is analyzed, the optimized solution has very small stiffness and damping to replicate what is obtained in case (c), where just a single spring with preload is used. However, the feasibility of having a spring with high preload and low stiffness is not very practical. Moreover, as seen in

case (b), for a spring-damper with no preload, the  $HIC_{opt}$  is very close to what is achieved with constant acceleration. For that case, in Figure 3-19 the reaction force contributed by damper and spring as well as the total force is plotted against displacement. As shown, the combination of optimized damping and spring results in a total force very close to  $f^*$ , which is desired for minimum HIC.

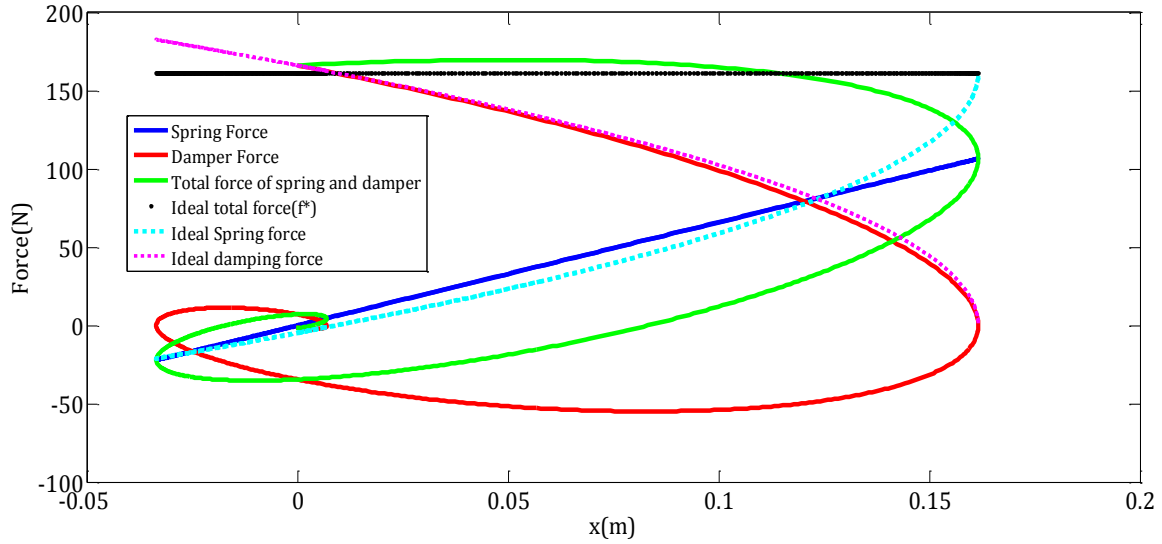


**Figure 3-19. Comparison of reactive force in spring and damper with the corresponding ideal forces,  $v_0 = 3 \text{ m/s}$ ,  $d_{max} = 16 \text{ cm}$**

Although the data in Table 3-2 indicate that using the ordinary spring and damper in parallel would result in the HIC value close to the hypothetical optimal value, the practical feasibility of this design should be taken into account. A search was therefore conducted for the closest spring and damper manufactured in the industry with relatively same design specifications for optimal damping and spring shown in Table 3-2. The design specifications for the damper and spring found online are given in Table 3-3 and Table 3-4, respectively.

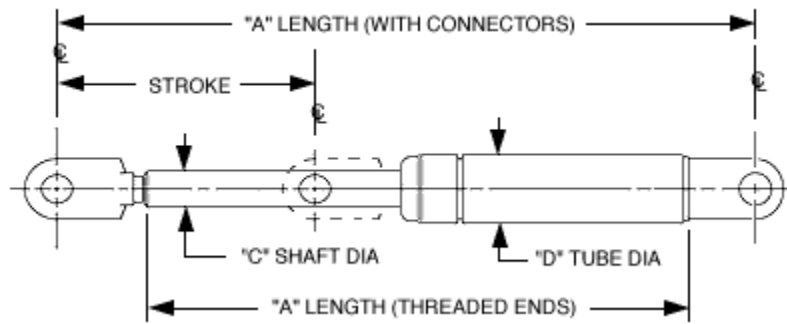


**Figure 3-20. Schematic of standard damper made by AVM manufacturer [37]**

**Table 3-3. Comparison of a standard damper dimensions for a specific stroke length [37]**

Part No.	Size "C" x "D"	Stroke	PS006 Connector "A" Length	PS12X* Connector "A" Length	PS130 Connector "A" Length	PS90 Connector "A" Length
SD200A	.251 x .591	2.00	6.74	7.89	7.89	8.13
SD300A		3.00	8.6	10.02	10.02	10.26
SD400A		4.00	11.08	12.5	12.5	12.74
SD500A	6 x 15	5.00	13.6	15.02	15.02	15.26
SD400V	.315 x .866	4.00	10.83	12.24	12.24	12.49
SD500V		5.00	13.07	14.49	14.49	14.73
SD600V	8 x 22	6.00	15.59	17.01	17.01	17.25
SD700V		7.00	18.23	19.65	19.65	19.89

**Table 3-4. Design specifications of a spring manufactured by Leespring [38]**

Specifications	
Product Category	Compression Springs
Coil Type	
Spring Pitch	Constant Pitch
Specifications	
Base Unit System	English Design
Outer Diameter	1.73 inch (43.99 mm)
Wire diameter	0.1970 inch (5 mm)
Free length	8.07 inch (205 mm)
Solid height	2.85 inch (72.49 mm)
Spring rate	6.61 N/mm (37.77 lbs/in)
Material	Stainless Steel
End Configuration	Ground ends; Closed (squared) ends

By comparing the compressed and extended length of each component, it is observed that the height of the spring having a stroke of about 130 mm should be close to 205 mm. However, for the damping to operate with the same stroke, the total extended length is almost 375 mm. Besides, the values given in Table 3-3 disregard the maximum force generated in damping under loading condition. Based on datasheets for dampers [37], the maximum force in the damper for the stroke considered here is much more than the optimal force of 160 N. By searching through different damper manufacturers ([37], [39], [40]), it was found that the extended length for existent dampers is nearly three times that of a certain stroke to be achieved. One might conclude, therefore, that the implementation of an optimum damper for the ideal impact isolation described in this chapter is strictly restricted to dimension specifications, such as stroke and extended length. Besides, there are miscellaneous variables in spring design including wire diameter, hole diameter, outside diameter, rod diameter, and spring materials that might aid in better adjusting desired spring specifications. Furthermore, the large variety of gas springs and air springs available in different dimension ranges makes the use of a spring more conceivable for effective energy management during an impact based on the *EOR* concept.

Finally, there is usually an unknown source of damping (such as friction, structural damping, etc.) in an impact absorber mechanism and thus, it is difficult to tune the damper to approximate the optimum value. In the following section, the ideal spring force in conjunction with a known value of damping in the system is examined.

#### **3.4.5. *Effective Operating Region of a Spring in a Mass-spring damper System***

When a spring is used in parallel with a dashpot, its effective operating region is different from that when there is no dashpot. In other words, the system's energy management in this case differs because the accumulative force of dashpot and spring should still be equal to  $f^*$  (for the ideal energy management). In fact, at the initial state of the impact, the velocity has its maximum value and therefore the spring force is minimal. As velocity decreases due to the deceleration applied, the dashpot force decreases and thus, the spring force should pick up to compensate for that until  $x = d_{max}$ , where



$f_{damping} = 0$ . Hence, the new force-displacement curve for the spring needs to be established as an ideal force trace in Equation (3-15). The spring force during impact should have the least variation from the new defined function in order to result in constant deceleration, because it was aimed originally to minimize HIC. To obtain the reference spring force, one can write,

$$\ddot{x} = -\frac{f^*}{m} \quad (3-21)$$

$$\dot{x} = -\frac{f^*}{m}t + v_0 \quad (3-22)$$

$$x = -\frac{f^*}{2m}t^2 + v_0t \quad (3-23)$$

$$t = \frac{v_0 - \sqrt{v_0^2 - \frac{2f^*x}{m}}}{f^*m} \quad (3-24)$$

$$f_d = c\dot{x} = c\sqrt{v_0^2 - \frac{2f^*x}{m}} \quad (3-25)$$

Therefore, the ideal force for the spring in conjunction with a damper is obtained as follows,

$$f_s^* = f^* - c\sqrt{v_0^2 - \frac{2f^*x}{m}} \quad (3-26)$$

Equation (3-26) can be further simplified using Taylor series for  $\sqrt{1+x}$ ,

$$\sqrt{1+x} = 1 + \frac{1}{2}x - \frac{1}{8}x^2 + \dots \text{ for } |x| \leq 1 \quad (3-27)$$

$$c \sqrt{v_0^2 - \frac{2f^*x}{m}} = cv_0 * \sqrt{1 - \frac{2f^*}{mv_0^2}x} = cv_0(1 - \frac{1}{2} \frac{2f^*}{mv_0^2}x) \quad (3-28)$$

Therefore, Equation (3-26) can be simplified as,

$$f_s^*(x) \sim (f^* - cv_0) + \frac{cf^*}{mv_0}x \quad (3-29)$$

Equation (3-29) reveals the important conclusion that when a small amount of damping is introduced, the spring needs only to have a constant stiffness with a prescribed preload in order for minimal HIC to be obtained. *This result demonstrates the functionality of one-stage energy absorption using a linear spring.* This eliminates any demand and possible difficulty related to the multi-stage energy removal from a system similar to what was shown in Figure 3-7.

To clarify the conclusion made here, the case study introduced in the section 3.4.3 and is studied again; however, in this study a damper with damping coefficient  $c=35\text{Ns/m}$  is utilized in the impact isolator. Optimum stiffness value for two cases with and without preload is obtained and summarized in Table 3-5.

**Table 3-5. Effect of preload on optimum HIC in existence of damping**

$C(\text{Ns/m})$	$F_0(\text{N})$	$K_{\text{opt}}(\text{N/m})$	$HIC$
35	63.8	360	64.028
35	0	1086	97.02

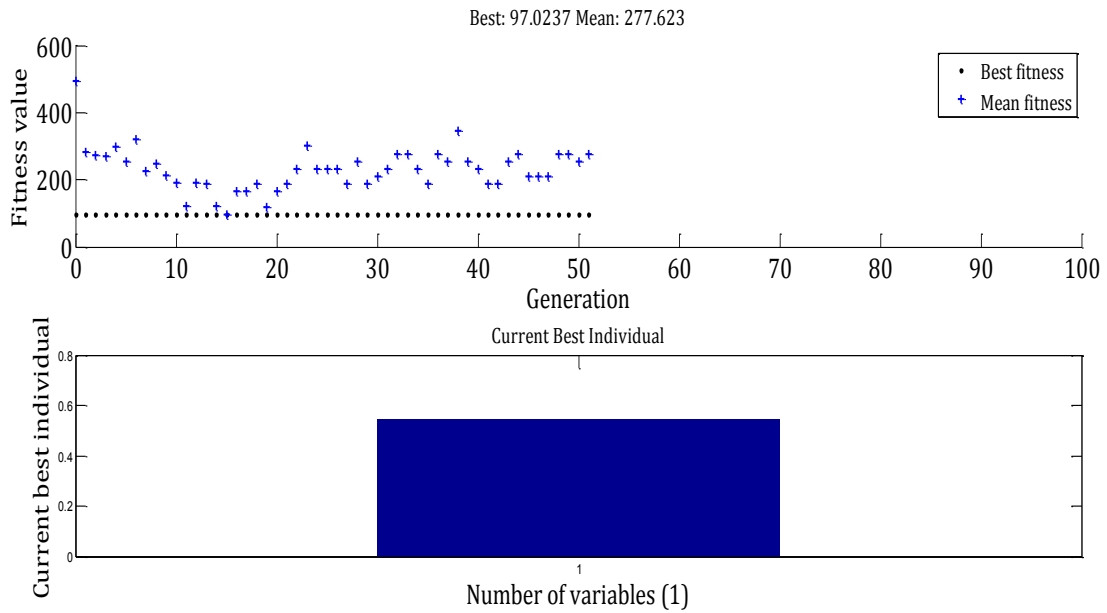


**Figure 3-21. Convergence history in GA for case of linear spring-damper (without preload)  $v_0 = 3 \text{ m/s}$ ,  $d_{max} = 16 \text{ cm}$ ,  $c = 35 \text{ N.s/m}$**

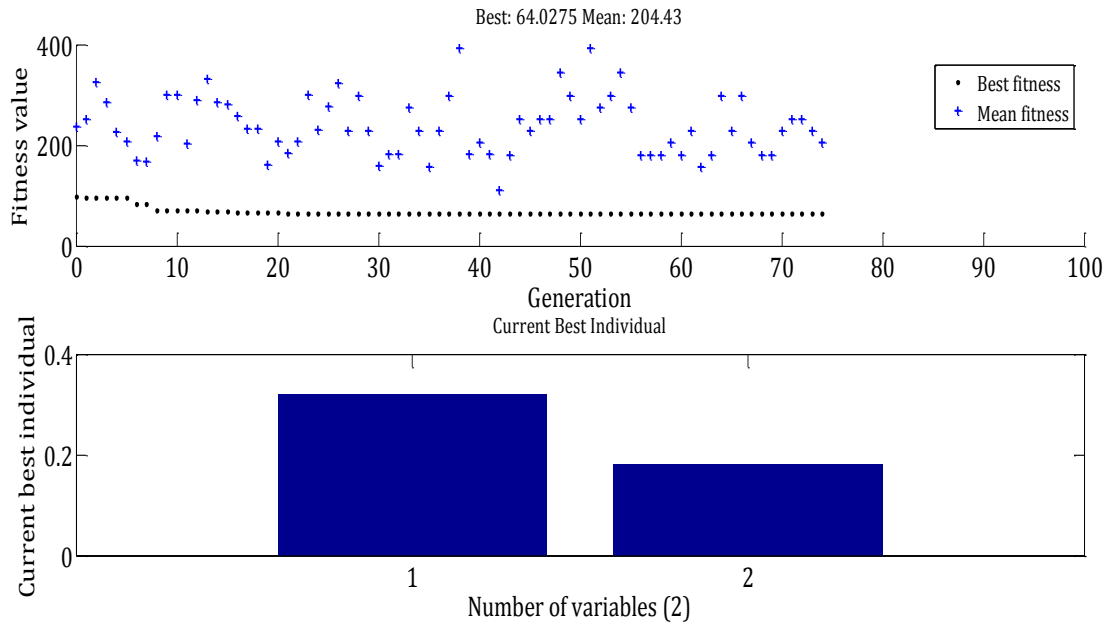


**Figure 3-22. Convergence history in GA for case of linear spring-damper (with preload)  $v_0 = 3 \text{ m/s}$ ,  $d_{max} = 16 \text{ cm}$ ,  $c = 35 \text{ N.s/m}$**

Also, from Figure 3-23, it is clear that in the case with preload, the total force trace is much closer to ideal force  $f^*$ .

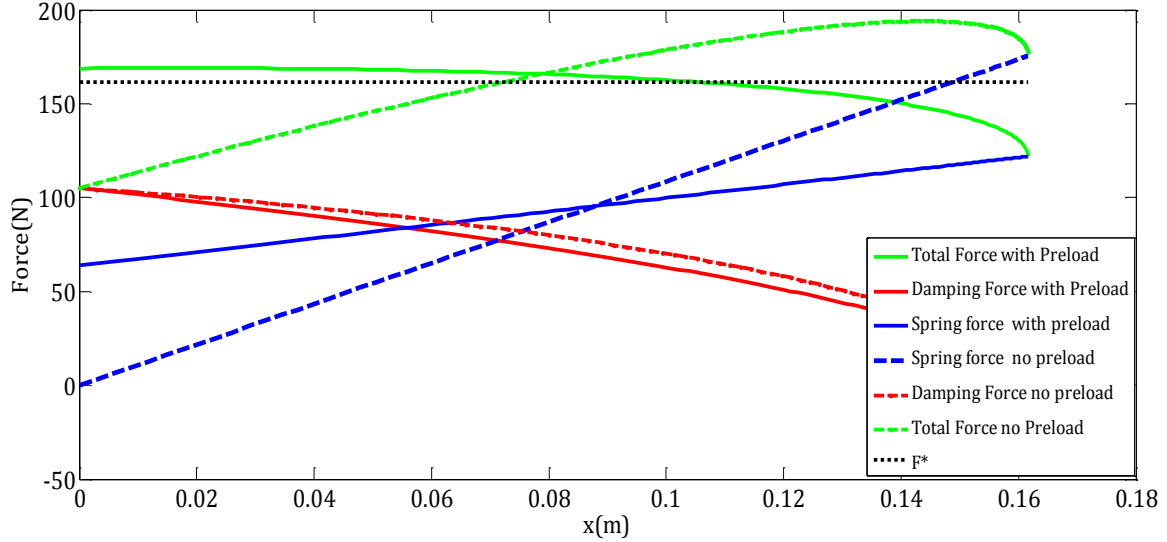


**Figure 3-23. Comparison of reactive forces in spring and damper with and without preload,  $v_0 = 3 \text{ m/s}$ ,  $d_{max} = 16 \text{ cm}$ ,  $c = 35 \text{ N.s/m}$**

### 3.5. Chapter Summary

In the first part of this chapter, square wave deceleration was shown to be the ideal control law for minimum HIC if peak acceleration is also considered as a constraint along with maximum permissible displacement. The efficiency of the square wave was then compared with that of other simple waveforms.

In the second part, the feasibility of generating a near-square wave form was assessed by introducing the new concept of “Effective Operating Region (EOR)” for a spring (potential) component. This conceptual design procedure was then illustrated through some examples and simulations for better clarifications. Moreover, the mathematical expressions for finding the effective operating region of spring with and without damper were established.

## **4. Venting Implementation into the Airbag with the Aim of Applying EOR Concept in Optimal Impact Energy Management**

### **4.1. Introduction**

As the most commonly recognized safety device, airbags have been commercially adopted in motor vehicles since 1980. The first generation of this device was incorporated into the steering wheel to provide driver protection, and soon it was extended to the front passenger side as well. Since it has achieved a major reduction in injuries and mortalities in car accidents, the manufacturers were inspired to use airbags for other areas of automobile interior to provide greater protection to passengers. Side airbags, rear airbags, and knee airbags are in line with this intention and have been implemented on a few modern cars. Moreover, recently a seatbelt-based airbag system has been developed and marketed for aircraft and road vehicles. In addition to automotive, airbags have also gained popularity in other vehicles, well-known examples being within the cabins of helicopters and motorcycles.



**Figure 4-1.** *Implementation of airbags in different locations interior of a vehicle*  
[\[http://www.whyhighend.com/airbags.html\]](http://www.whyhighend.com/airbags.html)



**Figure 4-2.** *Implementation of seatbelt based airbags in automotive and aircraft*  
[\[http://chrisescars.com/ford-designs-new-airbag-seatbelt/\]](http://chrisescars.com/ford-designs-new-airbag-seatbelt/)



**Figure 4-3.** *Implementation of airbag within the cabin of motorcycle and helicopter*  
[\[http://www.motorcycleinfo.co.uk\]](http://www.motorcycleinfo.co.uk),  
[\[http://tractors.wikia.com/wiki/Airbag\]](http://tractors.wikia.com/wiki/Airbag)

Airbag systems have been also implemented to the exterior of the cabin of vehicles. For example, Swedish auto company Volvo has produced the first automobile with an airbag installed on the exterior cabin to provide pedestrian's safety device, an innovation in line with European Union regulations on pedestrian safety. Boeing has developed a product called CST-100 which contains a cushioning airbag system incorporated beneath the spacecraft to lower the impact loads incurred during the landing. More recently, these types of airbags have been implemented into the undercarriage of helicopters to limit impact loads to the crew and damage to the airframe during crashes. As opposed to car airbags, these airbags are vented to facilitate load attenuation during impact.



**Figure 4-4.** *Implementation of airbag for CST-100 spacecraft designed and developed by Boeing [<http://eandt.theiet.org>]*



**Figure 4-5.** *Implementation of airbag exterior to the vehicle's cabin for pedestrian safety, developed by Volvo [<http://www.spiegel.de>]*

The overwhelming benefits of airbag use have motivated researchers to adopt them for other high-risk applications such as human airbags and inflatable hip protectors to prevent injuries. These airbags can cover a wide range of applications, from protective sporting equipment [41] to injury prevention for elderly [42]. Airbag systems have also found use in the workplace to protect construction workers from injuries caused by falling from altitude or against falling or thrown objects. The same concept has also formed the basis of other wearable-airbag products for use by elderly people who are susceptible to sudden and dangerous falls, as well as the airbag system designed to protect the wheelchair user's head and neck during wheelchair falls [42] (Figure 4-6).



**Figure 4-6. Implementation of human airbags a) protection against human fall, b) protection against wheelchair overturn [42]**

Upon reviewing various airbag systems, it was observed that venting has been introduced only to external airbags such as spacecraft and helicopters. This limited use might be due to the uncertain nature of an impact either in vehicular accidents or accidental falls by individuals as opposed to aircraft and spacecraft landing situations where time of impact is known beforehand. However, as discussed in this chapter, venting improves impact attenuation performance of airbags by removing energy from the system. In fact, an appropriate venting mechanism with minimal complexity added to the system is a practical example of "Effective Operating Region" that aims to enhance the personal airbag cushioning system.



## 4.2. Optimum HIC during Impact using Airbag with Venting Implementation

In this chapter, the modelling and performance evaluation of an airbag as an impact attenuation system is studied. This includes developing a mathematical model for describing the airbag's dynamic behavior during the impact and using the results in a *HIC* model to evaluate the effectiveness of the airbag design. Later in this chapter, computational results obtained from the developed dynamics model are validated by the experimental data obtained from the drop test setup, and finally, some observations and conclusions on venting effects on HIC optimization are made.

## 4.3. Airbag Impact Dynamics Modelling

Airbags attenuate impact loads by a series of energy conversion processes. First, the kinetic energy of the impacting payload must be transferred to the potential energy in the gas compression stage. When the internal pressure of the airbag reaches a preset value, the airbag vents open to exhaust the gas into the environment, thereby removing this potential energy from the system. Although this process may look straightforward, many detailed analyses including thermodynamics, fluid mechanics, and rigid-body dynamics, must be considered. In the following sections, airbag impact absorption is examined by taking into account the contribution of all the above-mentioned factors.

### 4.3.1. *Impact Attenuation from Standpoint of Thermodynamics*

Consider a system consisting of a solid mass dropped vertically from a fixed height onto the airbag with an in-built vent, as shown in Figure 4-7. In this system, before the impact initiates, the vent is closed (stage (a) in Figure 4-7). Thus, the overall energy content ( $E$ ) is the result of the combination of the kinetic energy ( $KE$ ) of the mass and the internal energy ( $U$ ) of the air within the airbag. The overall energy of the system, including mass and airbag at stage (a), can be represented mathematically by Equation (4-1).

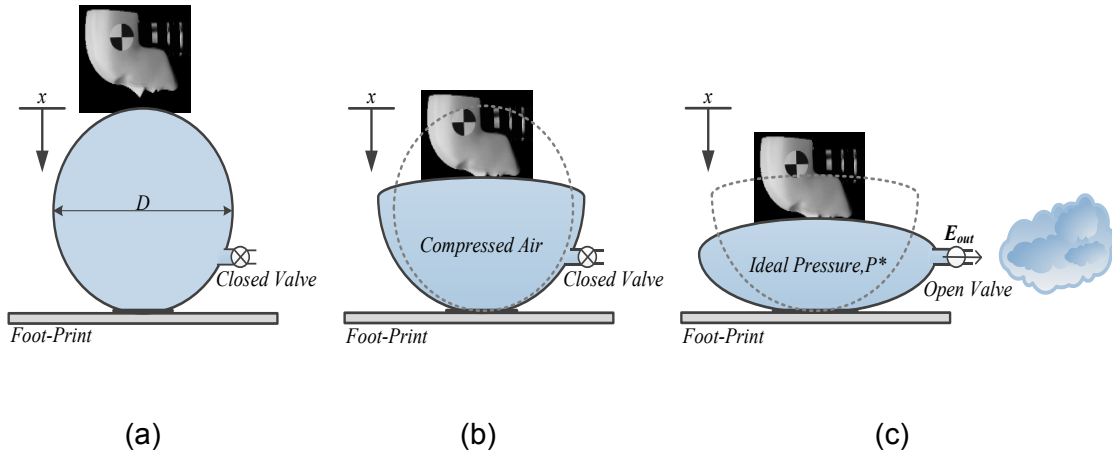


**Figure 4-7. Schematic display of different stages for airbag compression during impact**

$$E_{sys_a} = KE_{mass_a} + U_{gas_a} \quad (4-1)$$

In the period between initial contact and the time in which the internal pressure rises to the pre-set value, the mass does boundary work on the airbag as it becomes compressed (stage (b) in Figure 4-7). During this stage, the system still remains closed but is no longer isolated due to the work being done on it. This process can be represented by the first law of thermodynamics, which states that energy must be conserved. That is,

$$E_{in} - E_{out} = \Delta E_{gas} \quad (4-2)$$

Since the system is still closed, no energy is leaving the control volume and the only variation in compressed air energy is due to  $W_b$ , which denotes the boundary work being done on the airbag. The energy content of the air at the new state, denoted with subscript of  $b$ , can be rearranged as,

$$U_{gas_b} = U_{gas_a} + W_b \quad (4-3)$$

In effect, Equation (4-3) states that during the compression phase, the kinetic energy of the mass is being transferred to the internal air energy by means of boundary work. The boundary work for a small arbitrary displacement is defined by the force due to the system pressure  $P$  acting over its changing volume  $V$ . Therefore, the total work for the period of compression is expressed as,

$$W_b = \int_1^2 P dV \quad (4-4)$$

In equation (4-4), the dependency of work on pressure and volume implies boundary work is being achieved. Thus, the efficiency of the energy transfer between the mass and the gas within the airbag and the force counteracting on the mass is directly related to the gas pressure and, hence, the change in the geometry of the airbag as it compresses. By additional change in the airbag volume and the increase in internal pressure of gas, the force experienced by the mass is increased accordingly. Eventually, vents open immediately after it has reached its preset pressure (stage (c) in Figure 4-7). At this point, the system is open, and gas is allowed to leave the airbag. Similar to the previous phase, the energy content of the system can be determined by employing the first law of thermodynamics,

$$-m_{out}(h_{out} + KE_{out}) = U_{gas_c} - U_{gas_b} \quad (4-5)$$

where  $h$  denotes the specific enthalpy, and the subscript  $c$  denotes the state of the system after gas discharge. Since the enthalpy and kinetic energy of the exiting pressurized gas is very high, even a small amount of gas escaping might have a significant effect on the amount of energy dissipated from the system. Ideally, this venting stage is fast enough to ensure an immediate pressure drop inside the airbag and, therefore, more of kinetic energy of the mass can be absorbed at lower levels of

pressure (force) acting on the mass. In fact, the effectiveness of the energy transfer is determined by proper removal of gas energy at the right instant such that the mass can gradually and smoothly transfer all its kinetic energy without experiencing too much pressure from the compressed air. This energy management during impact is critical since improper quantity and quality of energy removed from the airbag results in either failure of the system in absorbing all the kinetic energy or high force transfer to the mass due to the high pressure of the internal gas remaining inside the bag.

In the following sections, the explicit modelling of the airbag geometry and pressure management is established for the vertical direction impact. The modelling framework explained there is based mainly on the dynamics model developed for the Mars pathfinder [43], which treats the impact absorption process from a fluid mechanics perspective. For simulating the behavior of an airbag during impact, the change in airbag geometry is calculated based on the position of the impacting mass at each time step. This is used to obtain the pressure, volume and the mass of the gas, information used in turn to determine conditions for venting of the airbag. Finally, knowing the thermodynamic state of gas, including its pressure, the dynamics of motion of the impacting mass is obtained and, therefore, its position for the next time step is calculated. Figure 4-8 presents a general overview of this strategy.

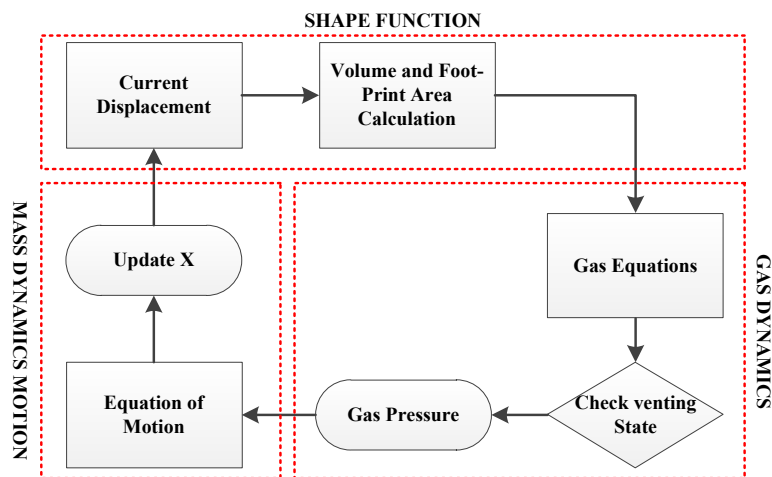


**Figure 4-8. Schematic diagram of integrated model of airbag accounting for the gas dynamics, head dynamics and changes in airbag shape**

The detailed interactions among all the physical phenomena mentioned above are expanded in the following sections.

### **4.3.2. System Dynamics Equation**

Consider the system of an airbag and impacting mass as a single degree of freedom shown in Figure 4-7. Performing a force equilibrium calculation between the mass acceleration, weight and the reaction force due to the internal pressure of gas, yields the following system dynamics equation,

$$m\ddot{x} + (P_{bag}(x) - P_{atm})A_c(x) = mg \quad (4-6)$$

As mentioned already, this equation forms the basis for determining the system dynamic state at each time step during the impact. In Equation (4-6),  $A_c$  represents the contact area of the airbag with the ground, and it varies during the impact. To predict the area and volume change of the airbag, the model presented by Esgar and Morgan [43] is adopted, and briefly explained in the following section.

#### **4.3.2.1. Change in Airbag Contact Area and Volume**

Since airbag geometry plays a key role in the dynamics of mass motion and, therefore, affects the efficiency of energy transfer between the mass and the airbag, it is important to find the proper shape function equations that depict the airbag geometry as accurately as possible. Here, for the simplicity, a cylindrical airbag geometry is chosen throughout this study as the closest geometry to the airbag used in experimental tests explained in Section 4.5.

Based on the analytical study performed in [43], the shape functions developed for a cylindrical airbag is obtained, assuming the axial length of the airbag remains constant during the impact process. These functions consider only the changes of the cross-section of the airbag from its initial circular shape, as shown in Figure 4-9.

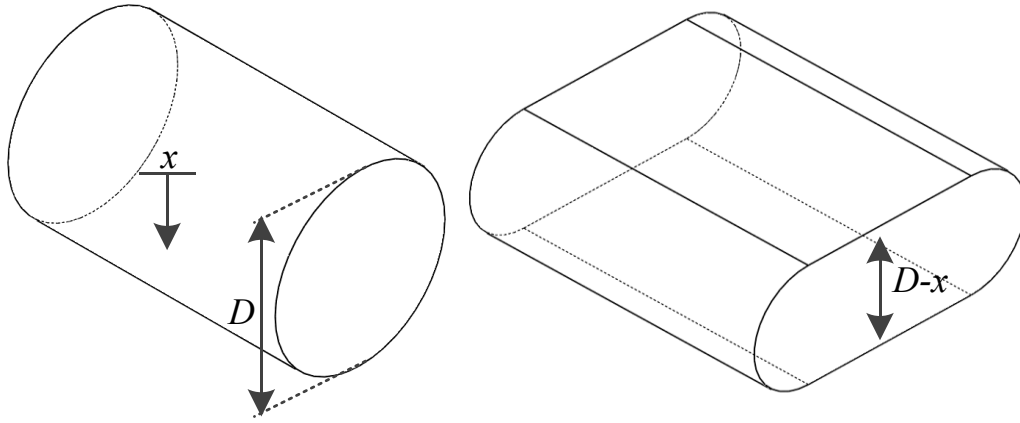


**Figure 4-9. Airbag shape alteration during the compression**

It is also assumed that the circumference of the airbag cross-section remains constant. Having these simple assumptions in mind, the airbag contact area and volume at any deflection  $x$  can be expressed as [43],

$$\text{Airbag Contact Area} = A_c(x) = L\pi x \quad (4-7)$$

$$\text{Airbag Volume} = V(x) = L(D - x)\left(\frac{\pi(D - x)}{4} + \pi x\right) \quad (4-8)$$

#### **4.3.2.2. Gas Dynamics Equations [44]**

After deriving the dynamic equations concerning impacting mass, the gas dynamics equation can be used to find effect of the thermodynamics state of the internal gas on the mass motion. It is assumed that the gas inside the bag acts as an ideal gas and that the process is adiabatic. Therefore, from the ideal gas law we have,

$$PV = wrT \quad (4-9)$$

where  $P$  is the pressure,  $V$  is the volume,  $w$  is the equivalent mass of the gas,  $r$  is the specific gas constant, and  $T$  is the operating temperature.

According to the adiabatic process,

$$\frac{T_2}{T_1} = \left(\frac{P_2}{P_1}\right)^{\frac{\gamma-1}{\gamma}} = \left(\frac{\rho_2}{\rho_1}\right)^{\gamma-1} \quad (4-10)$$

where the subscripts 1 and 2 indicate the state of the system at the beginning and at the end of a process, respectively,  $\rho$  is the gas density, and  $\gamma$  is the ratio of specific heats of the air (1.4 for the adiabatic process).

Also, the density equation is,

$$\rho = \frac{w}{V} \quad (4-11)$$

Given these sets of equations, the pressure of air can be determined during each time step, which subsequently allows for the opening condition of the airbag venting mechanism.

When the vent opens, the flow of gas can be modelled using the mass flow equation applied at the place of outlet valve (orifice) as,

$$\frac{dw}{dt} = C_D A_{orifice} \rho_{out} u_{out} \quad (4-12)$$

where the  $C_D$  is the discharge coefficient (a factor representing inefficiencies in the flow stream),  $A_{orifice}$  is the orifice area (outlet valve cross section area), and  $u_{out}$  is the flow velocity through the orifice, which can be represented in terms of only the pressure and temperature of the air inside the bag.

Cole and Waye [44] derive the flow rate equation through the orifice using a standard nozzle flow equation that is well known in advanced thermodynamic engineering textbooks [45]. In [44], the internal airbag pressure is defined as the upstream pressure, assuming the downstream pressure to be equal to the atmospheric pressure surrounding the airbag, as shown in

Figure 4-10.

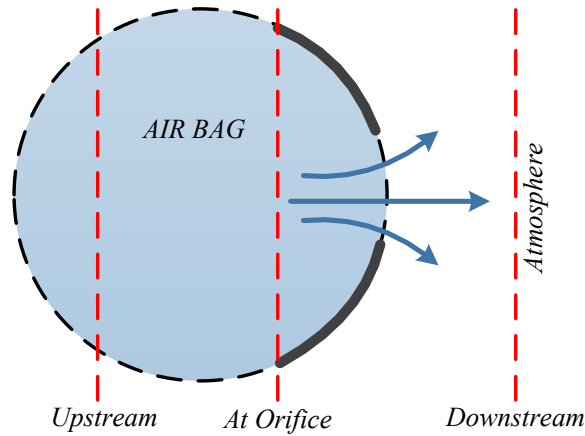


**Figure 4-10. Definition of upstream and downstream pressure for the airbag model**

After algebraically manipulating the equation of standard nozzle flow and applying the assumptions mentioned about upstream and downstream flow, the final form of the orifice flow is expressed as [44],

$$\frac{dw}{dt} = C_D A_{orifice} P_{atm} \left( \frac{1}{rT_1} \right)^{\frac{1}{2}} \left( \frac{2\gamma}{\gamma-1} \left( \frac{P_I}{P_{atm}} \right)^{\frac{\gamma-1}{\gamma}} \right)^{\frac{1}{2}} \left( \left( \frac{P_{bag}}{P_{atm}} \right)^{\frac{\gamma-1}{\gamma}} - 1 \right)^{\frac{1}{2}} \quad (4-13)$$

Equation (4-13) is valid for subsonic flows where the pressure ratio in orifice is adequately large ( $\frac{P_{bag}}{P_{atm}} > .528$ ). If the flow is sonic ( $\frac{P_{bag}}{P_{atm}} < .528$ ), then Equation (4-13) is expressed as,



$$\frac{dw}{dt} = C_D A_{orifice} P_I \left( \frac{1}{r T_1} \right)^{\frac{1}{2}} \left( \gamma \left( \frac{2}{\gamma + 1} \right)^{\frac{\gamma+1}{\gamma-1}} \right)^{\frac{1}{2}} \left( \left( \frac{P_{bag}}{P_I} \right)^{\frac{\gamma+1}{\gamma}} \right)^{\frac{1}{2}} \quad (4-14)$$

Here it can be observed that the sonic orifice flow equation is invariant of the pressure downstream of the orifice.

Finally, the imperfections inherent in orifice flow are captured by introducing the discharge coefficient  $C_D$  in Equations (4-13) and (4-14). In particular, this refers to the losses due to the frictional and viscous effects as the gas flows through the orifice. Here, data obtained experimentally in [44] are used to relate the pressure ratio to discharge coefficient.

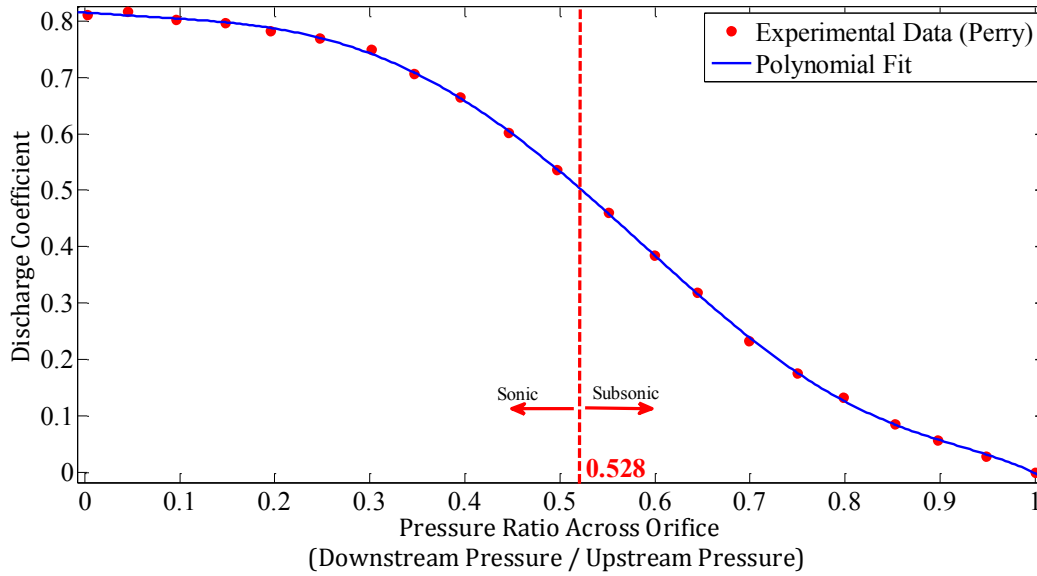


**Figure 4-11. Experimental data for calculating discharge coefficient  $C_d$  [44]**

#### **4.4. Integration of Gas-dynamics and System Dynamics for Airbag during Impact**

The governing equations from each of the previously discussed sections should be integrated to outline an iterative interaction between the gas dynamics and orifice (valve) flow components of the model with the dynamics of motion of the impacted mass. This is because the gas-flow requires pressure information from the gas dynamics state, which, in turn, requires information of the mass of gas remaining inside the airbag, which is dependent on orifice flow conditions. To resolve these dependencies, the pressure and gas mass values at each time step are solved by simultaneously satisfying Equations (4-9) to (4-14) for a given position and acceleration. When the solution for pressure is obtained for the corresponding position, its value is picked to calculate the acceleration experienced by the mass at that time step using Equation (4-6). This is then used to find the position and volume change for the next time step and the whole process is repeated to measure the mass acceleration for the impact interval. In this study, MATLAB is used for programming and the computational calculations discussed here (see appendix B).

#### **4.5. Test Apparatus**

Development of a test apparatus is essential to validate the results obtained from simulations based on governing equations discussed in Section 4.3. To meet this objective, the drop test setup shown in Figure 4-12 was designed and fabricated. This test apparatus consists of a payload mass (own-made headform) attached to a carriage that slides through a rail and an airbag mounted on the test bed's base which is fixed to the ground. An adjustable release mechanism is also designed to initiate the tests to acquire various drop heights (up to 1.5 m). Moreover, since the airbag model developed earlier assumes single degree of freedom in the vertical direction, the headform is always attached to the rail via the carriage to guide the motion in this direction. Also, the sensors mounted on the headform are protected from striking hard surfaces and getting damaged. In addition, rail friction is found negligible from the free-fall tests conducted

with the headform. The airbag component was chosen to be the real airbag material used in Hyundai automotive. A custom-made manifold was then fabricated to connect the airbag to the high-pressure air and the pressure transducer. Furthermore, to implement the venting mechanism, a model 58 series solenoid valve made by MacValves Inc, with outlet diameter (port size) of 1 inch, was purchased and mounted in series with an adjustable mechanical valve to provide a wider range of orifice cross-area. An accelerometer and a dynamic force sensor were also embedded inside the headform to capture and store the acceleration and force data for HIC calculation.

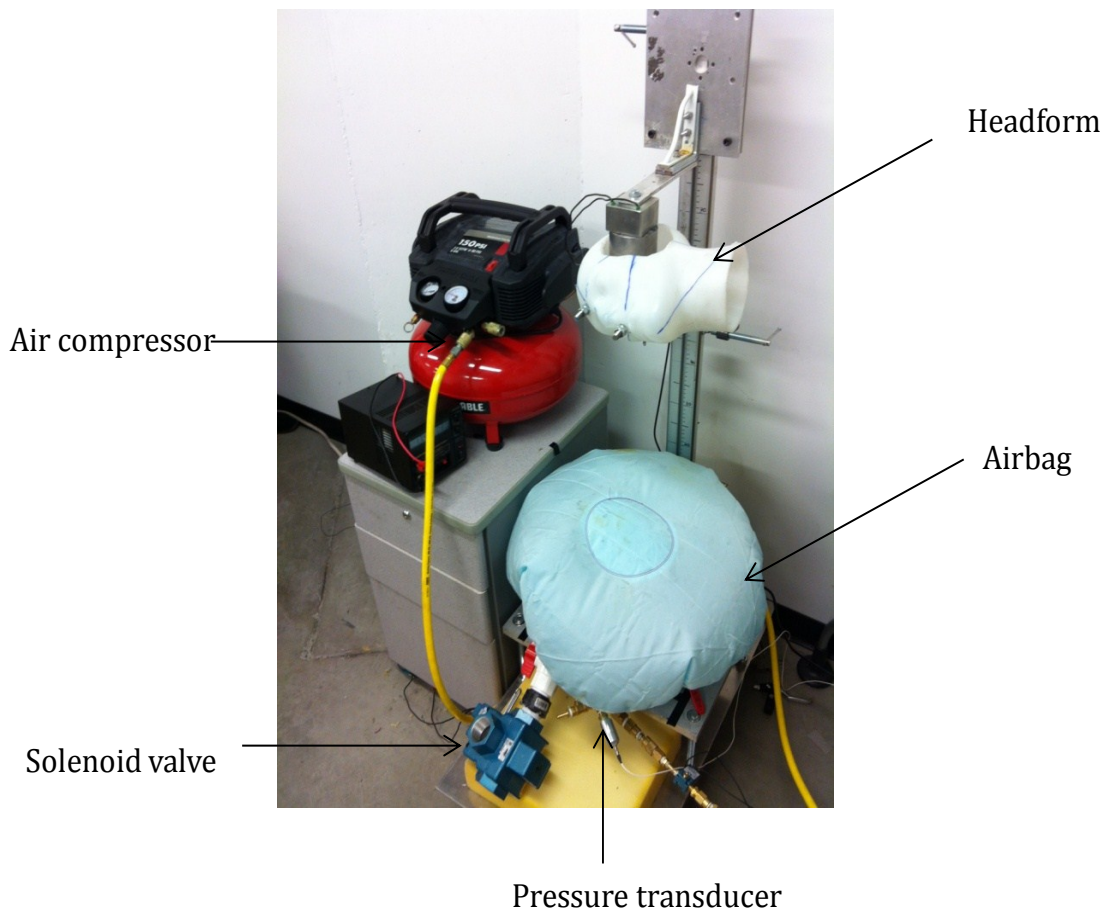


**Figure 4-12.** *Airbag test apparatus developed to measure the head acceleration during the impact*

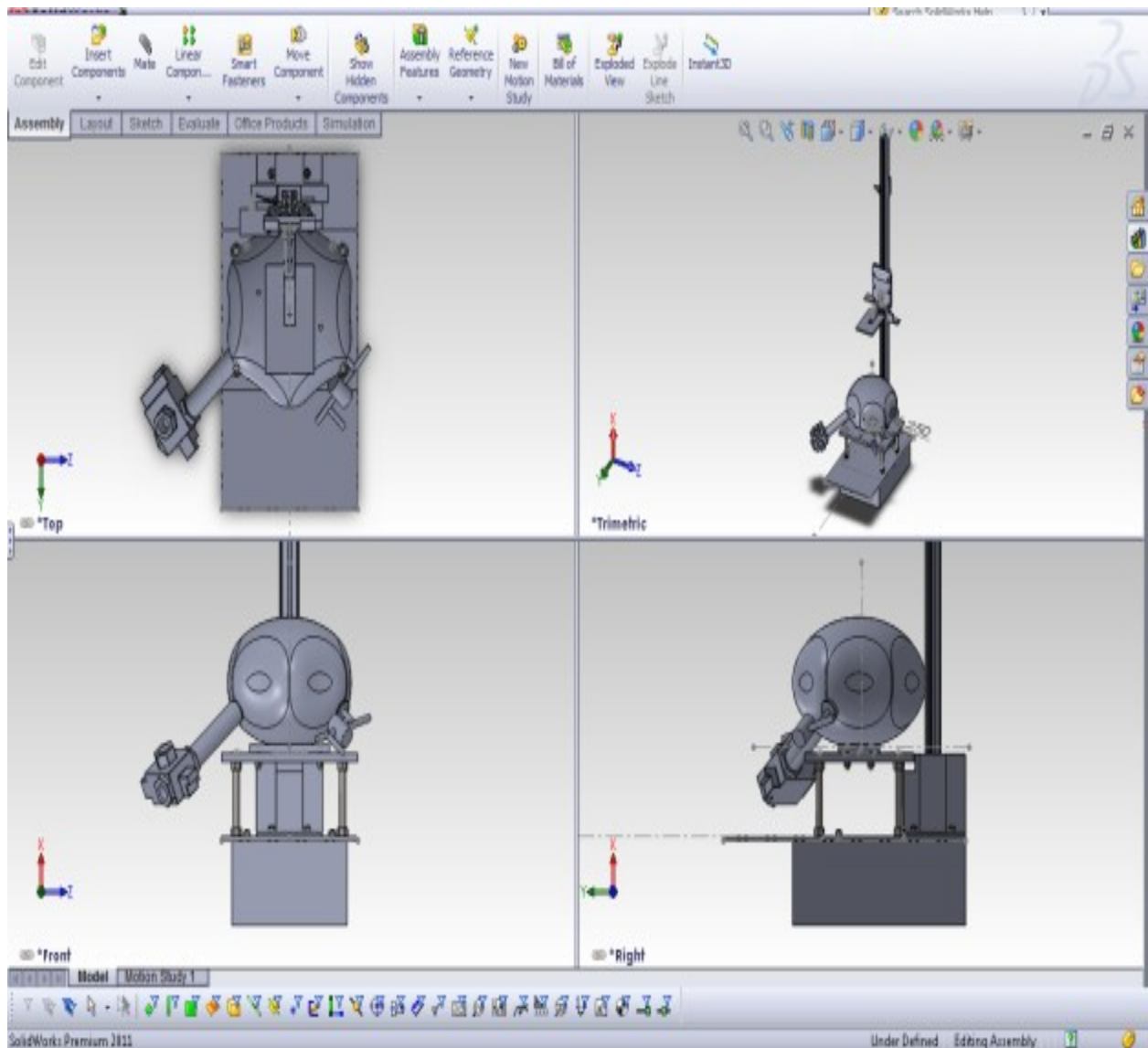


**Figure 4-13. Airbag test apparatus designed in Solidworks**

#### **4.5.1. Test Apparatus Trouble-Shooting**

After the first stage of test-setup preparation, unforeseen difficulties arose that had to be resolved. One difficulty related to the delay time in solenoid valve response, which is about 20 ms according to the device data sheet. This delay time is controlled by triggering the valve early enough before the impact. The second problem was the delicate porosity fabricated on the airbag material. The porosity caused the initial

pressure inside the airbag to drop immediately after the high-pressure line was disconnected before the impact. This is resolved by providing a control signal to disconnect the inflator just a moment before headform hits the airbag, ensuring the airbag holds the desired initial pressure at the very first moment of impact. Another difficulty was the extremely large sensors' noise such that the data captured by them was barely usable. The source of this additional noise was found to be the magnetic field generated in the solenoid valve upon its activation. This problem was solved by embedding the simple electrical circuit shown in Figure 4-14 in order to eliminate the magnetic field induced to the sensors, thus removing the noise [46].

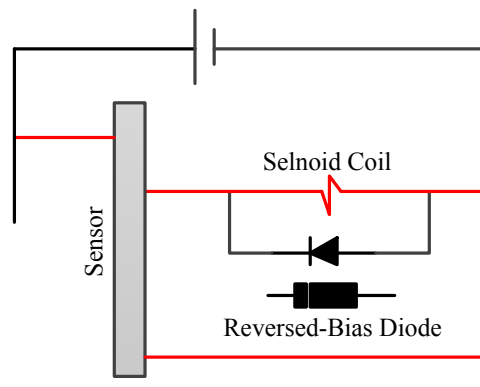


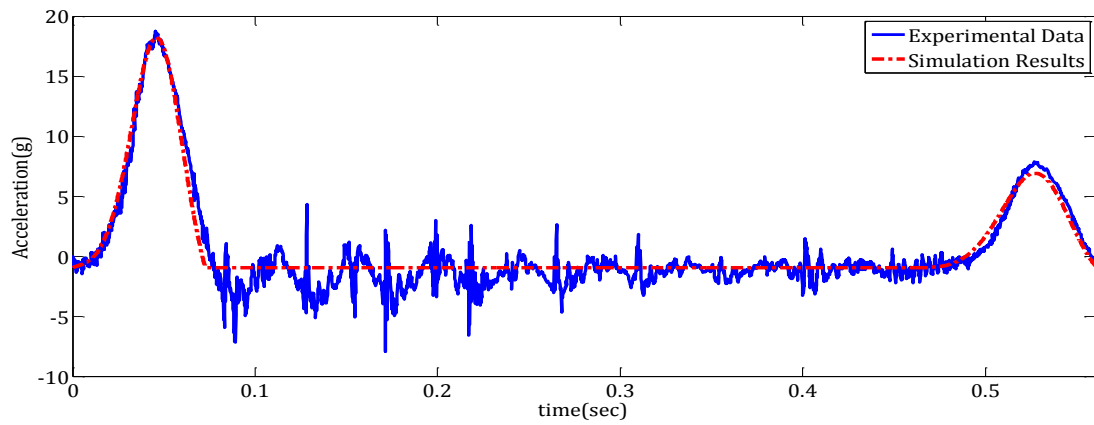
**Figure 4-14. Electric circuit used to suppress inductive noise due to voltage variations in solenoid coil**

In the circuit shown in Figure 4-14, the diode is connected in reverse-bias across the solenoid coil. In normal operation, the electric current cannot flow through the diode, so it flows through the solenoid coil. When voltage to the solenoid is switched off, a voltage with opposite polarization from that of the original applied voltage is generated by the collapsing magnetic field. This induced voltage creates a current flowing through the diode, cutting off the high-voltage spike [46].

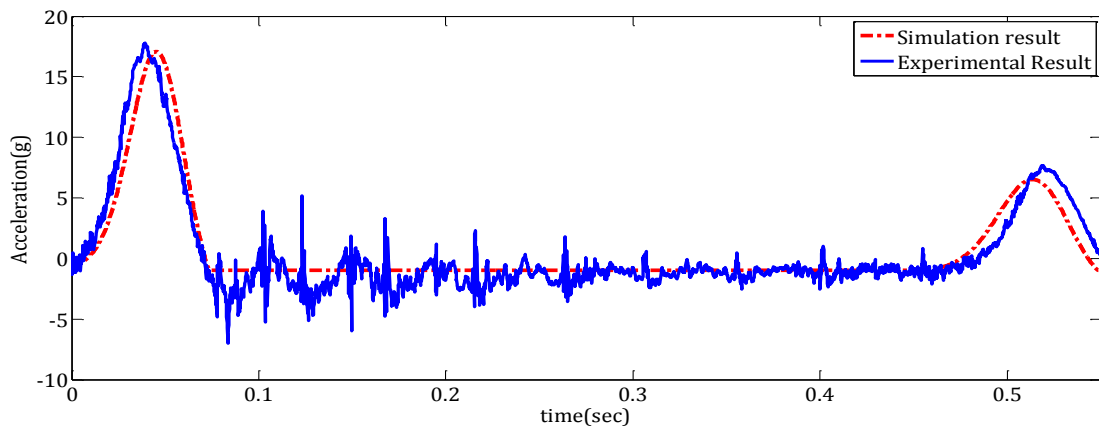
## 4.6. Comparing Experimental Results with Simulation Results

To evaluate the accuracy of the model, two sets of drop tests were conducted – one with fixed drop height at 70 cm and with varying initial pressure ranging from 101 *Kpa* to 130 *Kpa*, and the other with fixed initial pressure set to atmospheric pressure at various drop heights ranging from 10 cm to 100 cm. In these two datasets, the vent was set to be fully open and the varying parameters mentioned here were plugged to the MATLAB Code developed for the simulation purpose. The selected test results from each of the two test sets are shown in Figure 4-15 and Figure 4-16, part (a) through (c). As these figures clearly show, the acceleration obtained from the airbag impact model matches the experimental results. However, Figure 4-15(c) suggests that the simulation results deviate slightly from the experimental values when the initial pressure is increased, although it still follows the overall dynamic trends observed in all datasets.

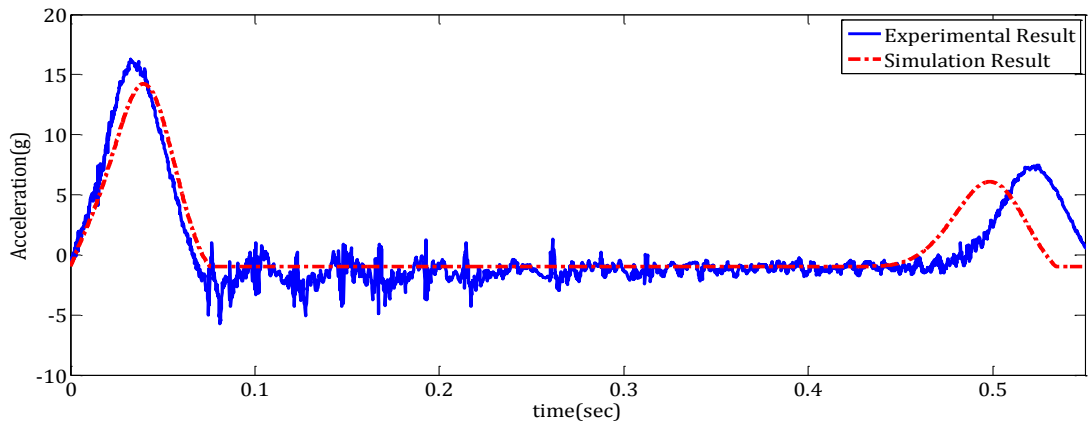
It should be noted that a slight refinement was made to the airbag model after experiments were performed, a refinement that was indeed necessary due to the geometry change approximation assumed through shape functions explained in Section 4.3.2.1. In fact, it is required that the volume and position of airbags be identified at the end of first stroke (where the headform loses contact with the airbag after bounce-back) as an initial state of the airbag for the next stroke. Also, it seems essential to include additional parts to the code in order to prevent the internal pressure of the airbag from dropping below atmospheric pressure.



(a)

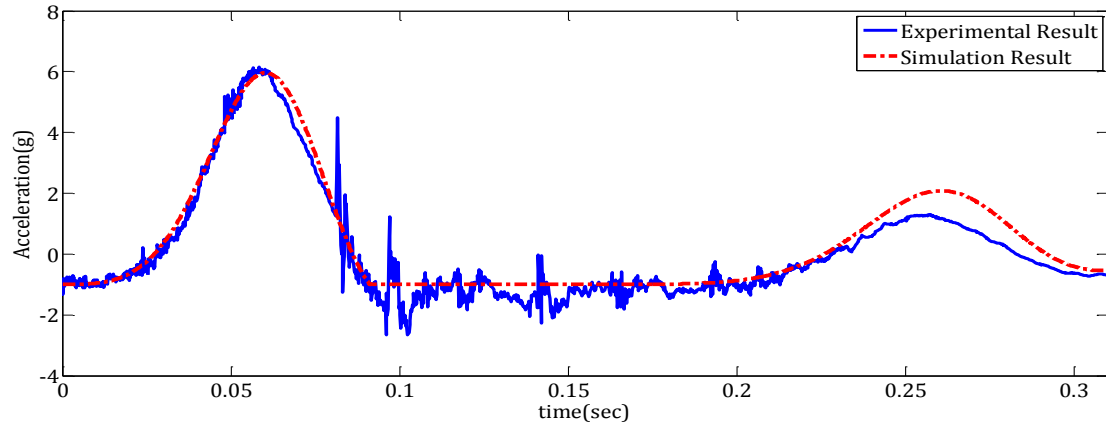


(b)

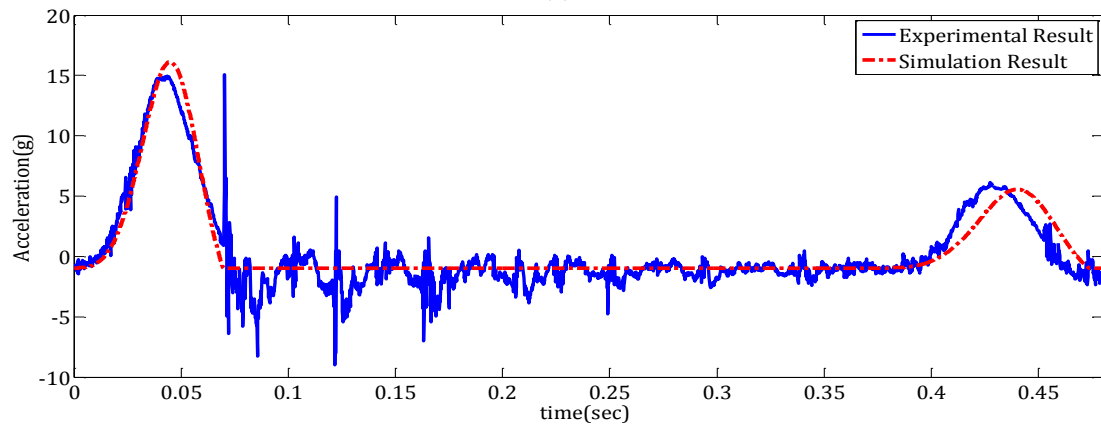


(c)

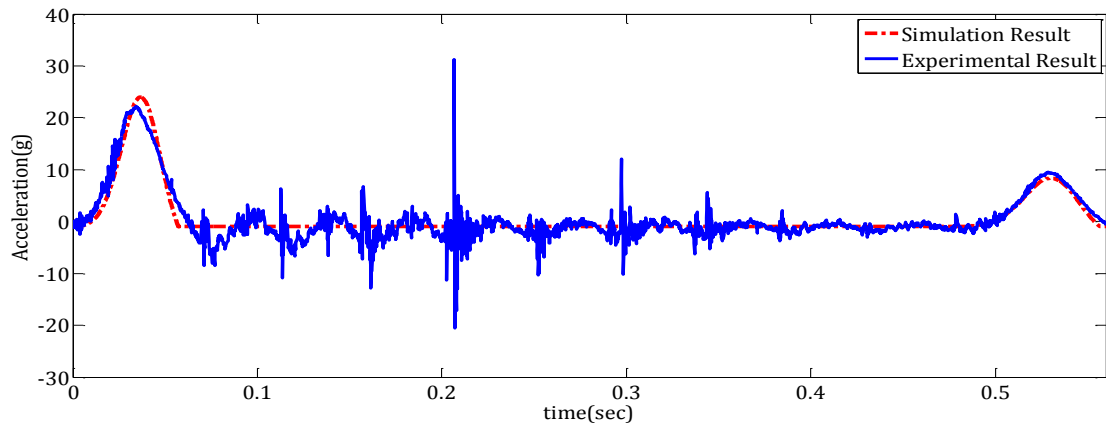
**Figure 4-15. Experimental results vs. Simulation results at  $h_0=70\text{cm}$ , a)  $P_0 = 101\text{Kpa}$ , b)  $P_0 = 103\text{Kpa}$ , c)  $P_0 = 115\text{Kpa}$**



(a)



(b)



(c)

**Figure 4-16. Experimental results vs. Simulation results at  $P_0 = 101\text{Kpa}$ ,  
a)  $h_0 = 10\text{cm}$ , b)  $h_0 = 48\text{cm}$ , c)  $h_0 = 80\text{cm}$**



- **Trend with Varying Height**

Figure 4-17 shows the effect of drop height and, hence, the impact velocity. As was expected, higher impact velocities result in higher peak acceleration in time response of the system. More obvious differences can also be noticed by comparing the location of the second peaks in each case, which are due to substantial change in impact velocity for the second stroke because the level of energy absorption in the first stroke in each case is substantially different.

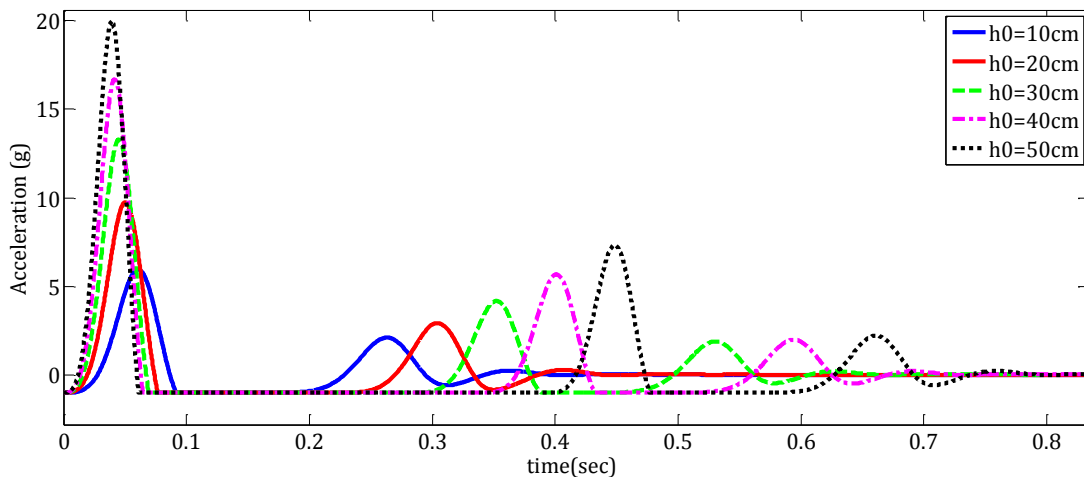


**Figure 4-17. Acceleration vs. Time, effect of dropping height**

- **Trend with Varying Mass**

The effect of payload mass on airbag performance is illustrated in Figure 4-18. Surprisingly, at the first glance, these results suggest that increasing the mass corresponds to decreasing peak acceleration. This unexpected result can be explained by the fact that a higher mass causes the airbag to hold sufficient pressure for a longer time while more pressurized air is forced to escape the airbag for a longer time as well. This observation is indeed in line with concepts explained in Chapter 3. In fact, this phenomenon guarantees an adequately large reaction force of the airbag to absorb the kinetic energy of the mass while removing excessive air from the airbag to keep that sufficient force continuously applied.

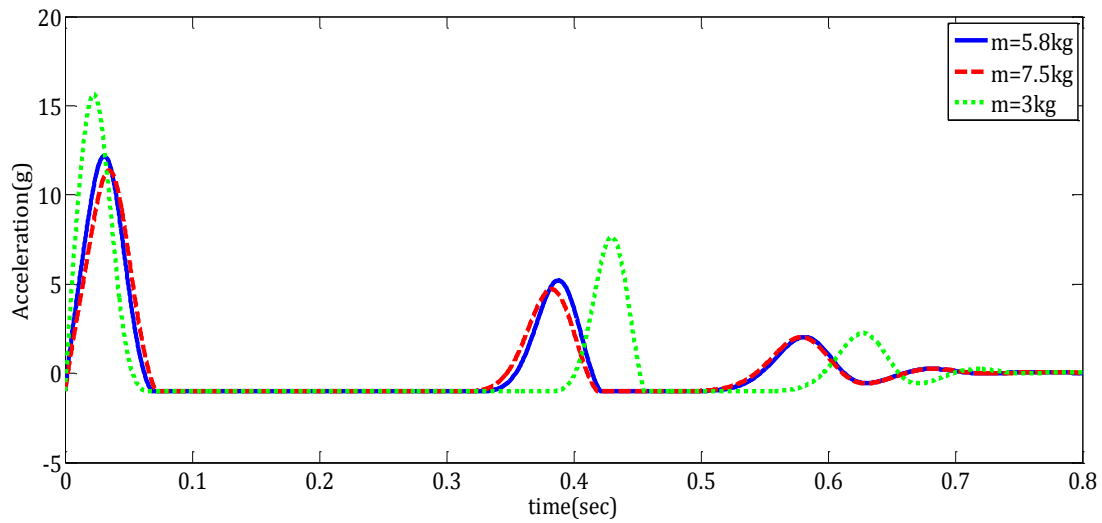


**Figure 4-18. Acceleration vs. Time, effect of impacting mass**

- **Trend with Constant Impact Energy**

Results shown in Figure 4-17 and Figure 4-18, lead to the conclusion that various impact events with the same impact energy can result in completely different airbag responses. This arises from the fact that the total impact energy is a function of both mass and impact velocity, and these two are shown to have contrasting effects on impact absorption. A fixed level of impact energy can be achieved by either increasing the mass and decreasing the impact velocity or decreasing mass weight and increasing impact velocity. In the former case, both parameters contribute to lower peak acceleration, and in the latter, both contribute to higher peak accelerations. As a direct conclusion of this observation, the identification of true mass weight and impact velocity values is found to be of crucial importance for precisely simulating impact condition tests for corresponding applications.

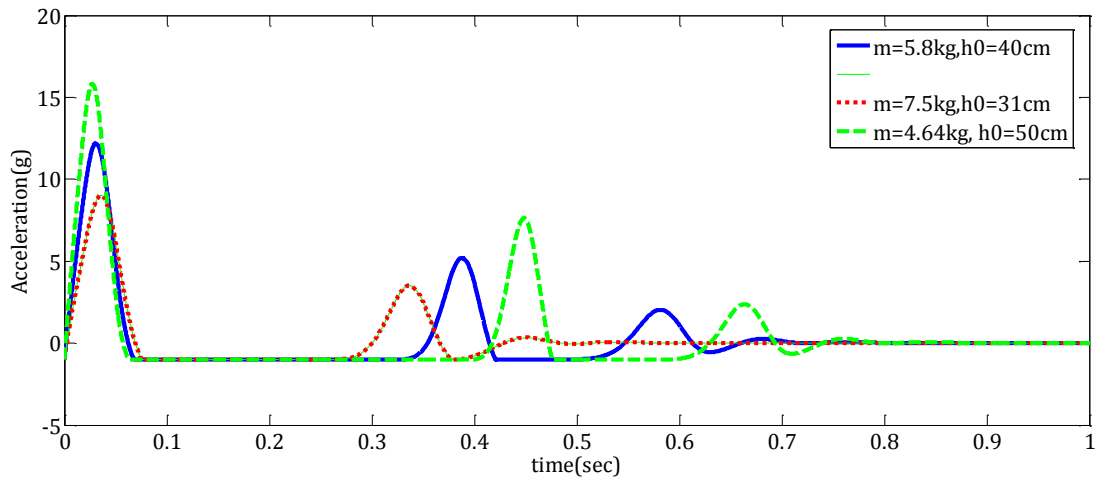


**Figure 4-19. Acceleration vs. Time, effect of initial impact energy**

- **$A_{max}/HIC$  against  $A_{orifice}$**

Here, the sensitivity of the system's performance with varying orifice area – the parameter assumed to be one of the key design variables in a venting mechanism – is investigated. In Figure 4-20 and Figure 4-21, the HIC and peak acceleration trends versus increasing orifice area are plotted. These graphs are obtained from the computational calculations for increasing orifice area corresponding to different heights.

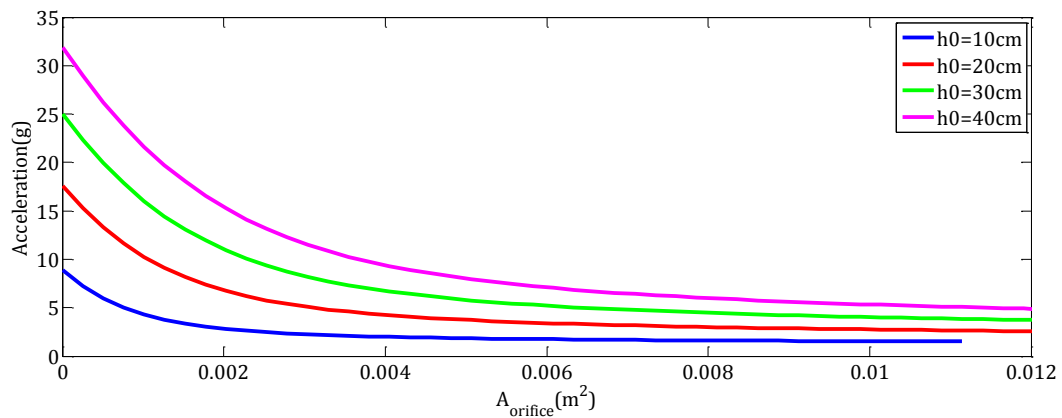


**Figure 4-20. Acceleration vs.  $A_{orifice}$  for different drop heights**

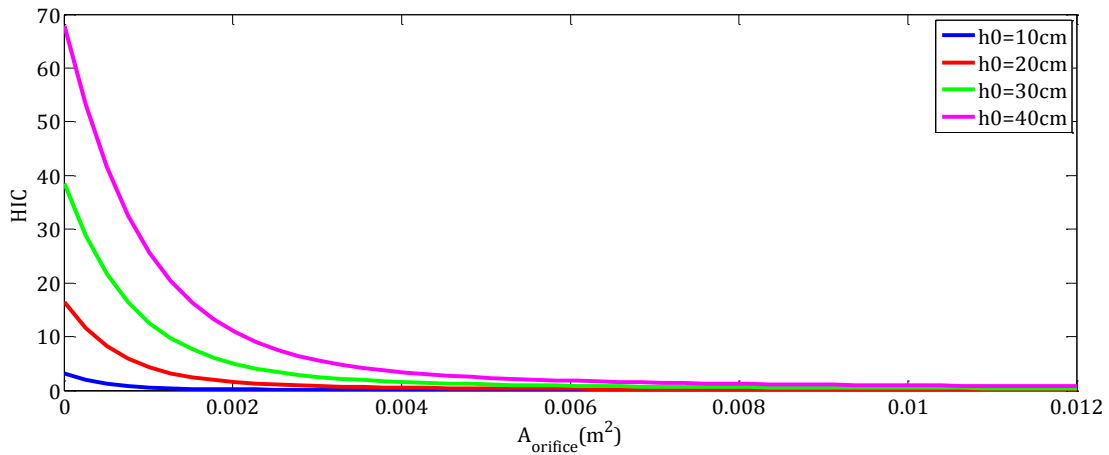


**Figure 4-21.  $HIC$  vs.  $A_{orifice}$  for different drop heights**

The  $HIC$  and peak acceleration values shown in these graphs are those experienced by payload mass due only to airbag force reaction. In most cases, the bottoming down phenomenon occurs, but the reactive force generated due to striking the hard surface (ground) is neglected. As a matter of fact, by excessively increasing the orifice area, there is a compromise in the quality of gas energy exiting the bag, resulting in the least contribution in absorbing the mass kinetic energy. This substantially defeats the key objective of  $HIC$  minimization. This issue might be resolved by calculating the mass impact velocity at the end of the stroke (before hitting the ground) and then taking this impact velocity into account for re-calculating  $HIC$  in the second phase. According to the analytical model proposed in [20] for  $HIC$  calculation in contact with hard surfaces, the  $HIC$  score is linearly proportional to the relative velocity of the head prior to impact. Having this in mind and using the experimental data obtained for  $HIC$  measured equal to 700 in [47] for a dummy test dropped from a height of 60 cm, the estimation of  $HIC$  at each level of impact velocity, after airbag bottoms out, can be determined. Finally, the maximum  $HIC$  in either phase is picked as a real  $HIC$  score considered for the efficiency of airbag performance during the impact process.

The headform velocity at the end of the airbag stroke and the modified  $HIC$  graph are plotted in Figure 4-22 and Figure 4-23 against the orifice area. The graphs better link the tradeoff observed in orifice area with the venting characteristics of the airbag. This

tradeoff highlights the importance of the balance between releasing sufficient energy and having massive gas flow from the airbag, which can lead to airbag bottom out.

In addition, the acceleration response versus time is plotted in Figure 4-24 for three venting areas close to  $.0015 \text{ m}^2$  at which the minimum  $HIC$  occurs. As seen in this figure, the acceleration in the case of minimum  $HIC$  rises to a finite maximum acceleration and then returns to zero acceleration more smoothly than those for smaller venting area.

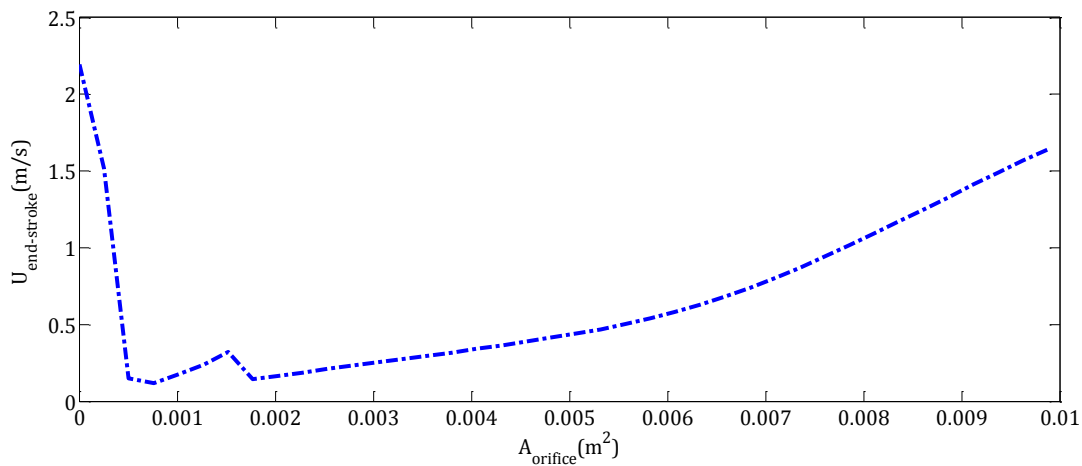


**Figure 4-22. Velocity of head at the end stroke of airbag vs.  $A_{\text{orifice}}$**

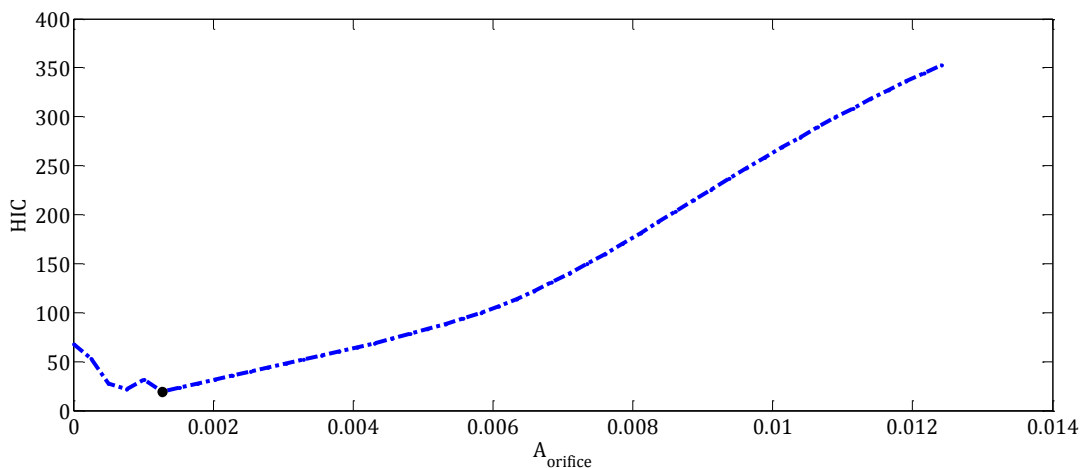


**Figure 4-23. Modified values of HIC vs.  $A_{\text{orifice}}$**

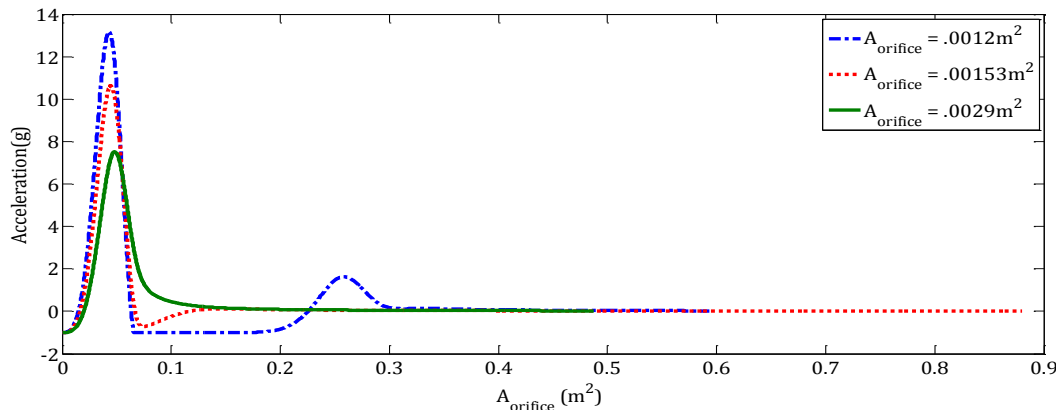


**Figure 4-24. Acceleration vs.  $A_{orifice}$  for values of orifice area section close to optimum value**

- **Effect of Initial Pressure on Airbag's Performance**

Figure 4-25 plots the  $HIC$  values versus venting area for different initial pressures. The simulations conducted here aim to find the effect of initial pressure on airbag performance. The results reveal a behavior that is highly insensitive to perturbations in initial pressure. A small reduction in  $HIC$  values associated with the higher pressure of 119 Kpa may be due to the changes in the characteristics of the flow released from the airbag at higher pressure. This insensitivity to initial pressure leads to a less stringent requirement for inflation pressure and mechanism.

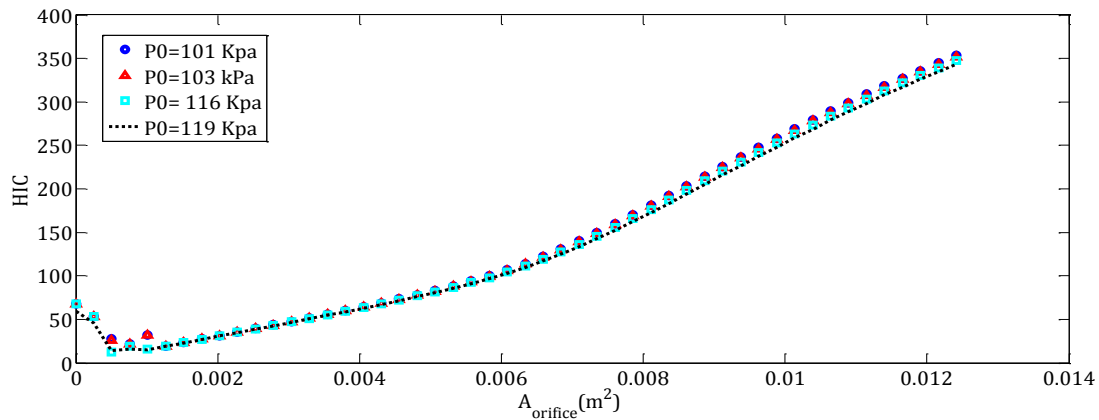
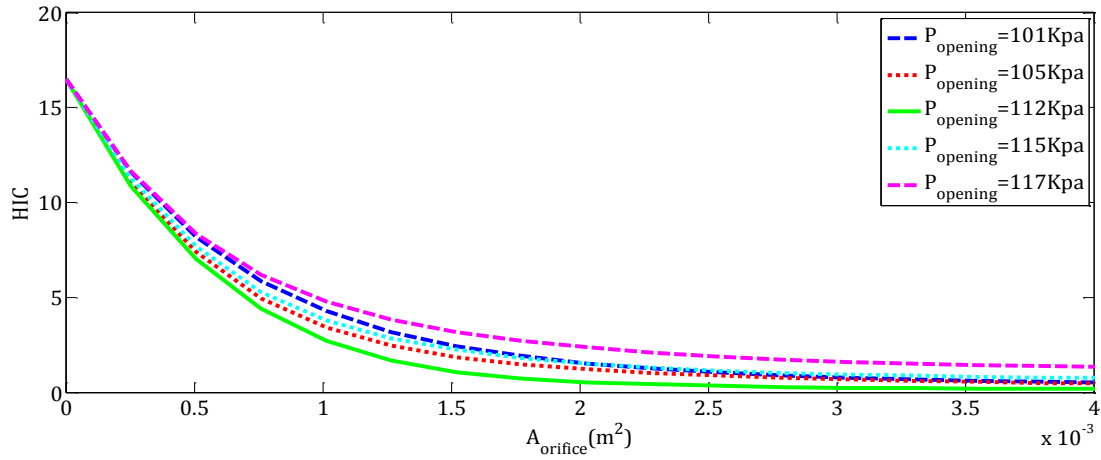


**Figure 4-25.  $HIC$  vs.  $A_{orifice}$  for different initial pressure in airbag,  $h_0 = 70$  cm**

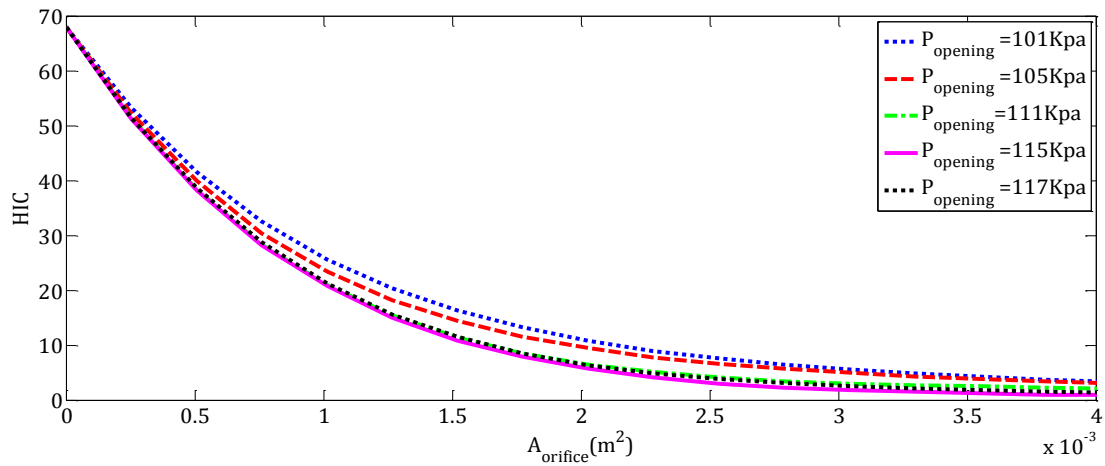
- **Effect of Different  $P_{opening}$**

In this section, the effect of opening pressure is considered in this section as the final contributing factor. The opening pressure terminology here is assigned to a desirable pressure at which the venting mechanism opens, which is usually the operational pressure level at which the most effective operating range of airbag in impact attenuation yields. The effect of this variable on  $HIC$  variation during the first peak of impact is plotted in Figure 4-26. This figure indicates that by increasing the opening pressure, the  $HIC$  values decrease due to higher quality energy released from the airbag to a point where any further increase in opening pressure results in higher  $HIC$ . In addition, Figure 4-26(b) indicates that the opening pressure, at which  $HIC$  values commence to raise, occurs at higher pressures, in line with intuitive expectations.

Finally, it should be noted that the solenoid valve used in our test equipment turned out to be too small to capture experimentally all the aspects of airbag performance. Moreover, the way that our experimental test equipment was designed was based on a one-time venting mechanism – that is, the valve remains open once it is opened. This mechanism, therefore, possibly does not allow for the “hold and release” approach to keep pressure close to its ideal level. One practical solution for this is to use pressure relief valves whose cracking pressure can be adjusted for different testing configurations; and since these are passive elements they have faster response times than electrically activated solenoid valves.



(a)



(b)

**Figure 4-26.  $HIC$  vs.  $A_{orifice}$  for different values of opening pressure; a)  $h_0 = 20$  cm, b)  $h_0 = 40$  cm**

## 4.7. Chapter Summary

Implementing an appropriate venting mechanism in the airbag is an effective way for  $HIC$  minimization as it fundamentally uses the design concept of “Effective Operating



Region.” In this chapter, the effect of venting area, opening pressure, and initial pressure as major venting characteristics of the airbag system were investigated. The tradesoff observed in the *HIC* and peak acceleration with respect to these variables indicates a balance between not venting sufficient energy through the orifice and releasing too much energy. In the former case, higher internal pressure (and therefore higher force) is the result, and in the latter case the possibility of bottoming-out during the impact is increased. The appropriate option for the opening pressure in a specific impact situation causes the airbag to maintain adequate pressure inside to absorb the impact energy before the orifice opens. Selecting the proper venting area, on the one hand, contributes to releasing excessive energy fast enough, enabling the airbag to operate at the desired maximum pressure. The initial pressure, on the other, contributes to the flow characteristics through the orifice and was shown to be less influential than the other factors.

## 5. Self-Inflator Foam Airbag

### 5.1. Introduction

Despite the overwhelming success of airbags in reducing accidental injuries in the automation industry, a number of deleterious effects of airbag deployment have been reported, including head and eye injuries [48], chemical injuries, and burns [49]. The conventional airbags incorporated into both automotive and recently-developed human airbags are expensive, heavy, complicated, and single-use. For example, the only commercialized version of human airbags for fall prevention, introduced by Japan, weighs 1.1 Kg and costs about \$1120 [25]. Moreover, the supreme complexity of body segments kinematics during a fall poses difficulty in differentiating between fall and daily activities [50]. This problem directly results inevitably in a great number of false deployments for human airbags, adding in turn to the overall cost since the airbag needs to be completely removed and the new airbag installed. These shortcomings are mainly due to the inflation technique (chemical reaction or compressed air). Having a simple, inexpensive, rechargeable airbag system can only be achieved by implementing a new inflation technique. To address this problem, a simple technique that uses compressed open cell foam as the self-inflator airbag is proposed. The idea is to put compressed (vacuum) foam inside an airbag and release it upon receiving a command signal (accident detection). The foam absorbs air for expansion and inflates the airbag.

In recent years, considerable interest has been focused on using fluid-filled, open-cell polymer foams as shock and vibration isolators due to their ability to dissipate a large amount of impact energy during the compression. This interest stems from the ease with which foam can be fashioned to different geometries and installed in place, the absence of maintenance requirements, and effective recovery ability of foams. They can be applied over a broad range of applications, for example, damping of vibrations of

machines, protection of sensitive goods against vibrations and impacts, and in casual shoes and mattresses. In fact, the polyurethane foam is considered a porous medium, and the significant feature of such a foam structure is its permeability to fluids.

As a highly porous medium, usually 70% to 90% of the volume of flexible polyurethane foam is filled with air. Hence, in the foam airbag proposed here, a flexible open cell foam can be compressed either by vacuum or by any type of compression mechanism. Besides, this volume of air within its structure, the airbag can greatly resemble the conventional airbags from standpoint of force reduction performance, particularly if the air can be effectively managed to be trapped inside the foam. During an accident, the impact sensor sends either an electrical or a mechanical signal to the release mechanism and the foam expands to its original volume in a short time. After all, because the foam may be compressed and released generally without any damage to the foam structure, the proposed airbag is multi-use and can be easily re-charged, possibly reducing substantially the overall cost of the airbag.

While the proposed idea is simple and promising, there are two key issues regarding its universal application: 1) foam airbag force attenuation performance, and 2) its expansion time. This chapter aims to address these two issues by designing foam to enhance its impact absorption performance as well as the expansion time. The analytical modelling of the dynamic behavior of such a foam during an impact is first studied. Innovative designs for enhanced performance of the foam are proposed and investigated experimentally. Also, the implication of “Effective Operating Region” in these designs is applied by conducting proper experimental tests.

## **5.2. Analytical Modelling of Open-Cell Foam**

Open-cell foams are low-density solid structures widely used in many applications – such as for energy absorption, cushion packaging, and insulation – because of their high specific mechanical properties, the effect of the fluid they are filled with, and being light-weight materials. However, flexible polyurethane foam is a highly nonlinear and viscoelastic material, a fact that complicates the modelling of its behavior

and parameter estimation. The nonlinear mechanical behavior of the foam includes two independent sources of contribution: time-dependent polymeric matrix response and gas entrapped in the cells. In order to construct fluid-filled, open-cell polymer foams with the desired damping or energy absorbing characteristics, one needs to understand how the matrix material, the fluid properties, and the cavity structure influence the damping and energy absorbing behavior. Therefore, in the past many investigations were conducted to accurately model the mechanical and dynamical behavior of flexible polyurethane foam to predict its impact energy absorption.

A simplified model of flexible foam comprising two reactive elements in parallel is described in [51], and is depicted in Figure 5-1. Although the model is simple, it provides valuable insights into foam behavior during compression. At low compressions, the compressive modulus of the cell walls, which defines the polymer matrix, dominates the reactive force, but it levels off as the cell structure experiences the critical buckling load. On the other hand, the pressure in the closed cells slowly rises at the beginning of foam compression and rapidly grows as the compression increases. The resultant compressive reactant force is therefore the sum of these two curves.

Dunger et al. [52] offer a simple microstructure model to describe fluid-filled open-cell foam. In its simplest form, the model consists of parallel elastic plates that define the solid structure, and gaps between them are filled with air (Figure 5-2). The constitutive equation is obtained by calculating the air pressure distribution when the uniaxial load is applied to the foam structure. They have also discussed the influence of different foam geometries, matrix materials, and fluid on the storage and loss modulus of open-cell foam.

Hilyard and Djiauw ( [53], [54] ) describe the viscoelastic behavior of flexible foams under large dynamic strains, such as those that may occur during the impact loading, by separating the viscoelastic behavior of the polymer matrix from the fluid's contribution. They also represent the flexible foam behavior by obtaining a lumped model for the foam (Figure 5-3). They develop mathematical equations to describe the foam structure, which can be used to predict the acceleration experienced by the striking mass, and the energy absorption.

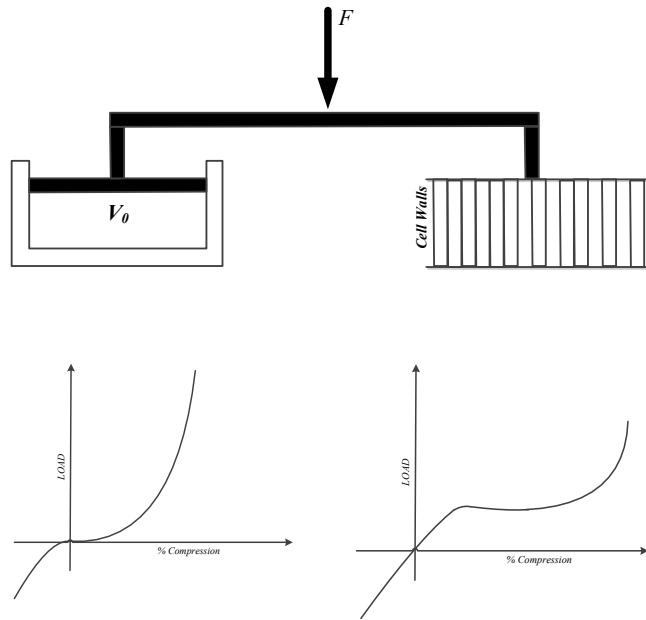


**Figure 5-1.** *The schematic display of the reactive elements in flexible foam during compression*

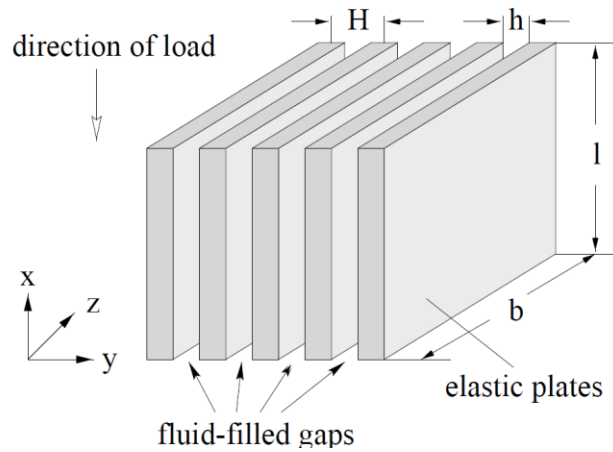


**Figure 5-2.** *Fluid-filled structure of open cell foam developed in [52]*

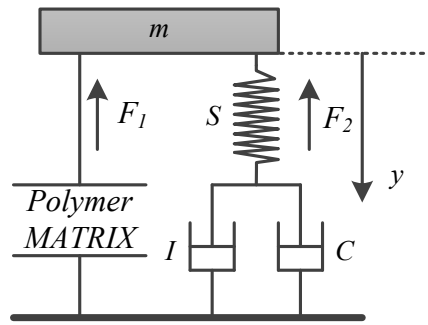


**Figure 5-3. A lumped model for open-cell foam [54]**

Moreover, a theoretical approach for pneumatic damping in foam is developed by Zwikker [55] using a simple mechanical model consisting of a piston, spring and tube (Figure 5-4) to represent the foam structure. Rusch [56] derive equations that consider the effects of the physical properties of the foam and the air on pneumatic damping. The resistance to airflow of the porous structure is a contributing factor in the damping. Consequently, permeability of foam has been studied by some researchers ([57], [58], [59]).

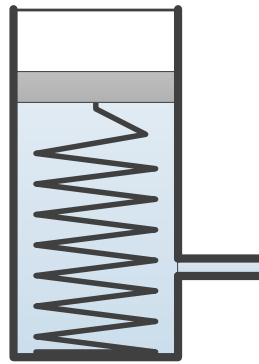
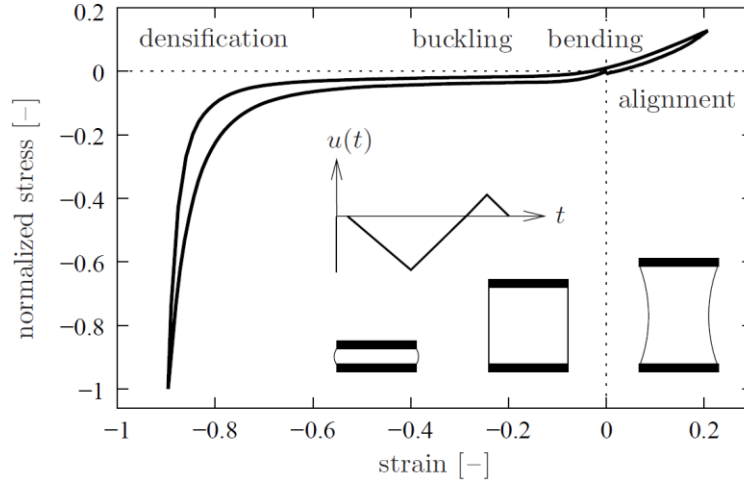


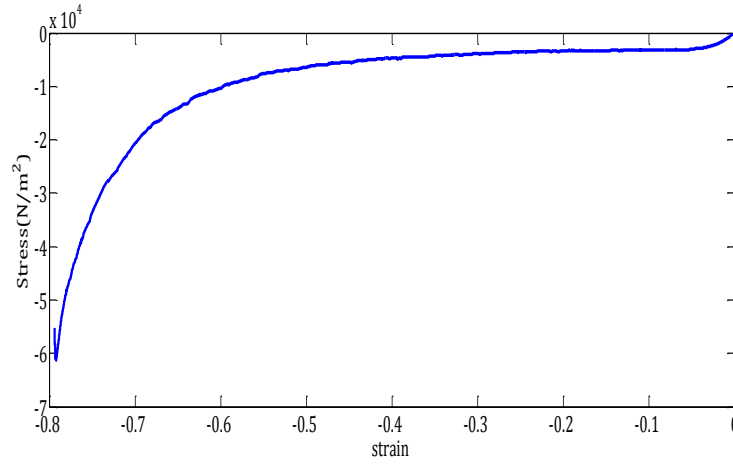
**Figure 5-4. A simple mechanical model for foam dynamic behaviour [55]**

Polymer matrix alone can be modelled as a Kelvin-Voigt model consisting of a pair of parallel spring and damper, in which the spring accounts for the foam matrix stiffness and the damper accounts for the intrinsic hysteresis behavior of the foam. In principle, the typical stress-strain curve from a uni-axial loading experiment on foam can be separated into three distinct regions, which can be explained in terms of deformation

mechanisms at the macroscopic level (Figure 5-5). In particular, the linear (elastic) stress response observed in the first region is associated with bending of cell walls in the foam structure. As the foam structure is further compressed, these cell walls buckle, resulting in a plateau-like stress region macroscopically. Under very large compressions, where the cells are almost collapsed and the cell walls are folded on each other, a densification region results and a rapid increase in compressive stress is observed.



(a)



(b)

**Figure 5-5. Typical Stress-strain curve for open-cell foam a) schematic display of different regimes of compression, b) experimental result**

Recently, many researchers have tried to model the system from a macroscopic point of view as the sum of a nonlinear elastic and linear viscoelastic response [60]. The model includes a polynomial type stiffness which concerns the force nonlinearities generated in foam associated with different levels of strain; the viscoelastic response is represented either by fractional derivatives [61] or relaxation kernel, which is assumed to be an exponential type [60]. White et al. [60] propose the combination of nonlinear elastic element and the relaxation kernel to represent the viscoelastic behavior of the open cell foam [Figure 5-6]. With the nonlinear and viscoelastic properties, the restoring force  $F_k$  in the material can be expressed as,

$$F_k = kx + \underbrace{k_3x^3 + k_5x^5 + c\dot{x}}_{\text{Non-linear elastic component}} - \underbrace{k \int_0^t \Gamma(t-\tau)x(\tau)d\tau}_{\text{Viscoelastic component}} \quad (5-1)$$

where the viscoelastic component can be expressed as the sum of exponential terms,

$$\Gamma(t-\tau) = \sum_{i=1}^n a_i e^{-\alpha_i(t-\tau)} \quad (5-2)$$

where  $a_i$  and  $\alpha_i$  are viscoelastic parameters to be estimated empirically.

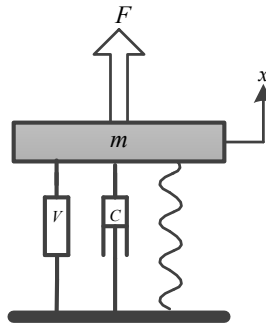


**Figure 5-6. A single-degree-of-freedom system with nonlinear viscoelastic elements [60]**



The proposed model has been a base for many further investigations since it is able to capture some of the foam behaviors such as “strain-rate dependency,” “hysteric,” and “creep-relaxation” in time domain, and “softening-hardening” in the frequency domain. The results of experiments performed to show the hysteric behaviour of foam mainly due to pneumatic damping and structural damping along with strain-rate dependency behaviour of foam are shown in Figure 5-7.

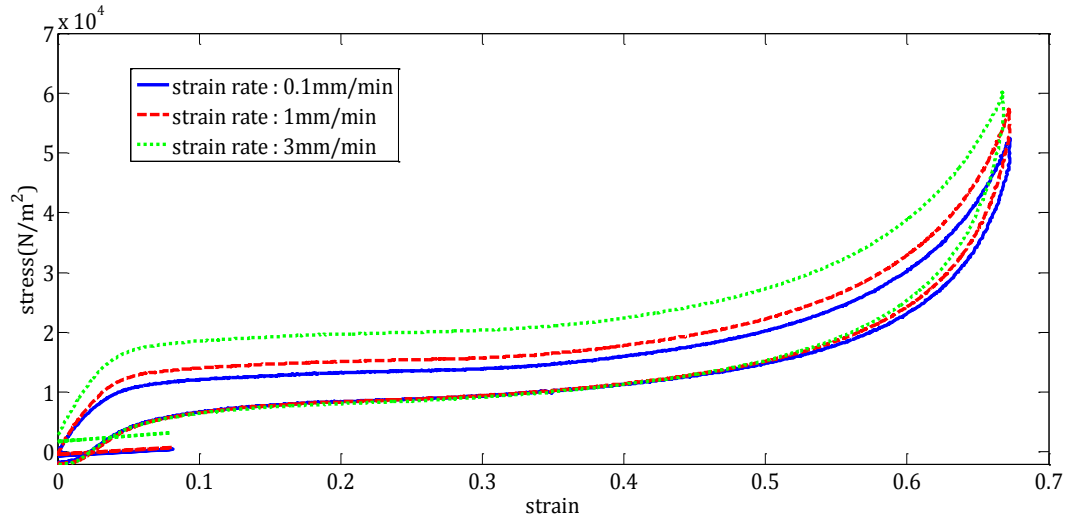


**Figure 5-7. Experimental results showing “hysteric” as well as “strain-rate dependency” behaviour of foam**

In particular, the softening-hardening phenomenon in foam can be clearly seen in the frequency domain. For this purpose, the experimental test setup shown in Figure 5-8 is used. To obtain dynamic response data, a 2” diameter cylindrical foam sample is placed between a base plate and a sliding top plate. This is guided by one vertical post, constraining the foam to vibrate in a single direction. Also, a low-friction linear bearing is used to minimize the effect of sliding contact between the top plate and the guide post. This setting is fixed on a shaker to achieve harmonic base excitation. During the tests, the acceleration of the base plate and the sliding top plate are measured with accelerometers. Here, the various input amplitudes in the range of .03 in to .33 in are applied to the base plate in the frequency range of 5 Hz to 18 Hz.

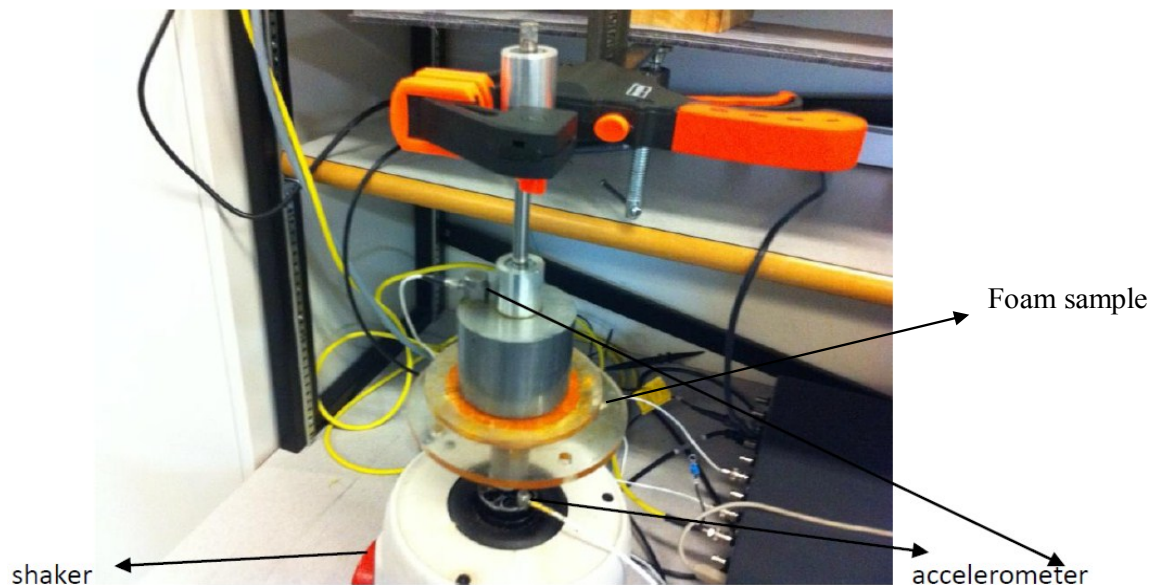


**Figure 5-8.** *Experimental test setup for measuring frequency response of open-cell foam*

As Figure 5-9 shows, there is initially a noticeable shift downward in the frequency of peak response and a corresponding increase in the amplitude of peak response. However, as the excitation amplitude is increased, the resonant frequency increases. The initial softening behavior is thus followed by a hardening effect as the excitation amplitude is increased. This behavior is also intuitively predictable from time-domain response as the force-deflection curve alters from plateau region (softening region) to densification regime (hardening region). Mathematically, this phenomenon is due to the opposite signs of  $k_3$  and  $k_5$  in Equation (5-1). For small values of displacement, the term  $x^3$  with negative coefficient is dominant; however, for higher displacement magnitudes the term  $x^5$  with positive sign is more dominant and, therefore, the hardening phenomenon occurs in lieu of softening.

Moreover, in Figure 5-10, the “frequency hysteresis” aspect of foam nonlinearity is observable in frequency response, where the frequency response of the nonlinear system depends on the direction of frequency changes (frequency increase or decrease). This figure also shows clearly for higher excitation amplitudes the well-known “jump phenomenon” as the major characteristic of nonlinear systems. This terminology

in nonlinear oscillation refers to a sudden jump in the amplitude of a system's response at resonant frequency as the frequency either increases or decreases from that point [62].

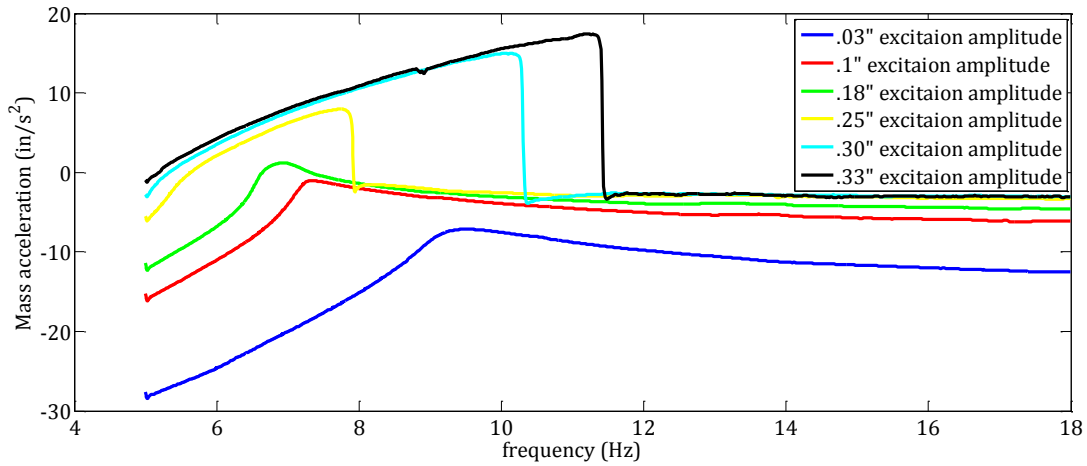


**Figure 5-9. Softening-hardening behaviour of foam in frequency response**

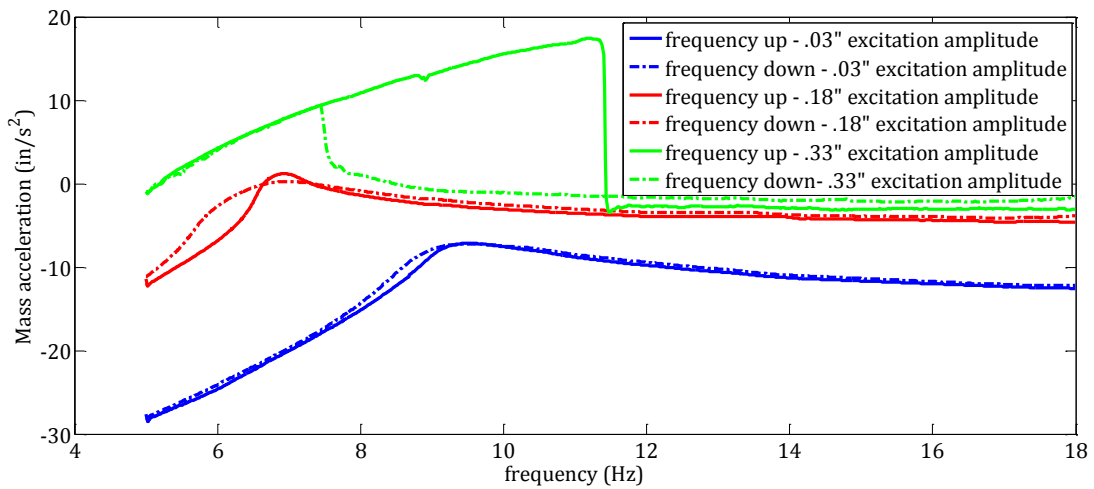


**Figure 5-10. Frequency hysteresis for nonlinear open cell foam**

### 5.3. Foam Airbag Deployment Time and Injury Protection

Understanding the fundamental aspects of foam's dynamic behavior helps in addressing the two challenges discussed in the introduction section regarding implementation of the foam airbag concept. One challenge is to investigate whether the foam can deploy fast enough before the actual impact and determine how this deployment time can be improved. The other challenge considers the injury protection of foam airbag. In the following, each of these key issues is discussed separately.

#### 5.3.1. *Expansion Time*

##### 5.3.1.1. *Testing Apparatus*

To measure the expansion time of foam samples, test equipment was designed and fabricated. The setup shown in Figure 5-11 allows the air to be vacuumed out of the bag via an opening connected to a vacuum positioned directly below the displacement sensor. The vacuumed bag compresses the foam sample. The vacuum is then shut off and the valve is re-opened, allowing air to flow into the bag and the foam sample. A LVDT (Linear Variable Differential Transformer) is connected to a computer via DAQ card.

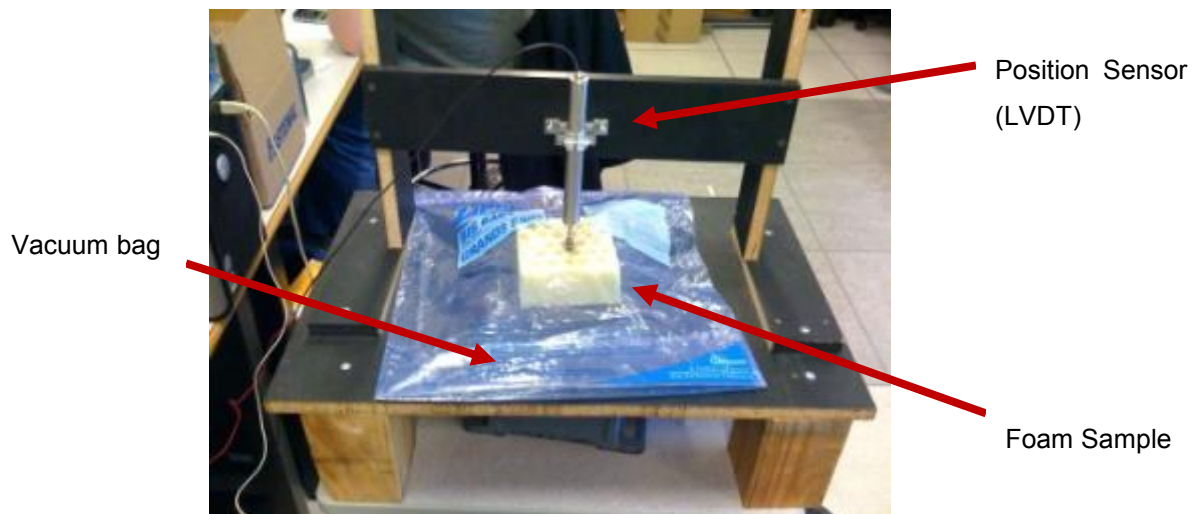


**Figure 5-11. Test apparatus for measuring expansion time of open-cell foam**

### 5.3.1.2. Simulation Results

Using the described Lumped model proposed by Hilyard [54] for dynamic behavior of flexible-foams, it is possible to predict theoretically the expansion time of a compressed foam. To determine the fluid contribution in viscous damping during foam deformation, they developed equations for an incompressible fluid, considering variation in permeability  $K$  with respect to foam deformation. The relation for calculation of permeability of foam under compression is given in Equation (5-3):

$$K(y) = K_0 \left( 1 - \delta \frac{y}{h} \right) \quad (5-3)$$

where  $K$  is foam permeability at any compression level  $y$ ,  $K_0$  is the permeability at no-compression state,  $h$  is the foam thickness, and  $\delta$  is a coefficient to be obtained experimentally.

Next, the velocity of fluid in the direction perpendicular to compression direction can be obtained from the following continuity equation for incompressible fluid (Figure 5-12):

$$v = \frac{x \dot{y}}{\phi \left( 1 - \frac{y}{h} \right)} \quad (5-4)$$

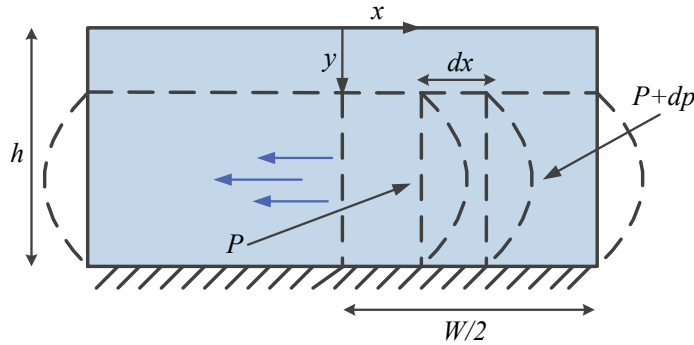


**Figure 5-12. Compression of fluid-filled block of open cell foam**

where  $\varphi$  is the volume fraction of open cells, and  $x$  is measured from the foam block centre in the direction perpendicular to foam compression. By relating fluid velocity to the pressure gradient within the foam, the force rising from air flow through the porous medium can be written as:

$$\frac{dp}{dx} = \frac{\mu}{K} v + \frac{\rho}{B} v^2 \quad (5-5)$$

$$F_f = C \dot{y}_f \pm I \dot{y}_f^2 \quad (5-6)$$

In Equations (5-5) and (5-6) above,  $\mu$  and  $\rho$  are dynamic viscosity and density of the fluid, respectively, and  $B$  is the fluid inertia representing the foam resistance to the fluid flowing through the foam. The viscosity coefficient  $C$  and inertia coefficient  $I$  are also given by:

$$C = \mu W^3 L / (24 \phi h K_0 (1 - \delta \frac{y}{h}) (1 - \frac{y}{h})) \quad (5-7)$$

$$I = \rho W^4 L / (64 \phi^2 h^2 B(y) (1 - \frac{y}{h})^2) \quad (5-8)$$

Since the air-flow velocity may be significant at the instant that the compressed foam is released, the term of fluid inertia in Equation (5-5) may not be negligible and, therefore, the parameter  $B$  similar to  $K$  is considered as a function of strain described by Equation (5-9):

$$B(y) = B_0 (1 - \frac{y}{h})^2 \quad (5-9)$$

Finally, we can find the total rise time of foam through the following equation:

$$C\dot{y} - I\dot{y}^2 + F_{matrix} = 0 \quad (5-10)$$

where  $C$  and  $I$  are defined in Equations (5-7) and (5-8), and  $F_{matrix}$  is due to the polymeric matrix stiffness. The polymeric stiffness is measured by means of the experimental test apparatus shown in Figure 5-13. In this setup, the controllable linear actuator is programmed to compress the foam at a low rate (1 mm/min) and the installed force sensor and LVDT are meant to measure the force and displacement, respectively, at any instant over the compression cycles. The stress-strain curve obtained for the polyurethane foam used in experimental and simulation tests is shown in Figure 5-5(b).

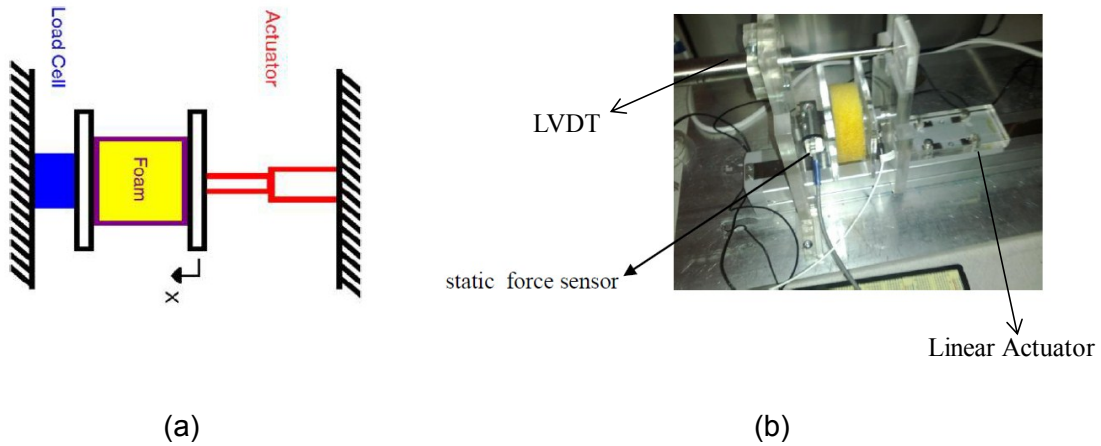


**Figure 5-13. Schematic of the experimental test setup for measuring foam stiffness, b) experimental test setup**

To perform the simulation tests, the non-linear equations of the system were solved in Simulink-MATLAB. The results of both experiment and simulation tests are illustrated in Figure 5-14, showing good agreement between the two curves. In addition, the foam sample characteristics used in experiment and simulation tests are listed in Table 5-1.

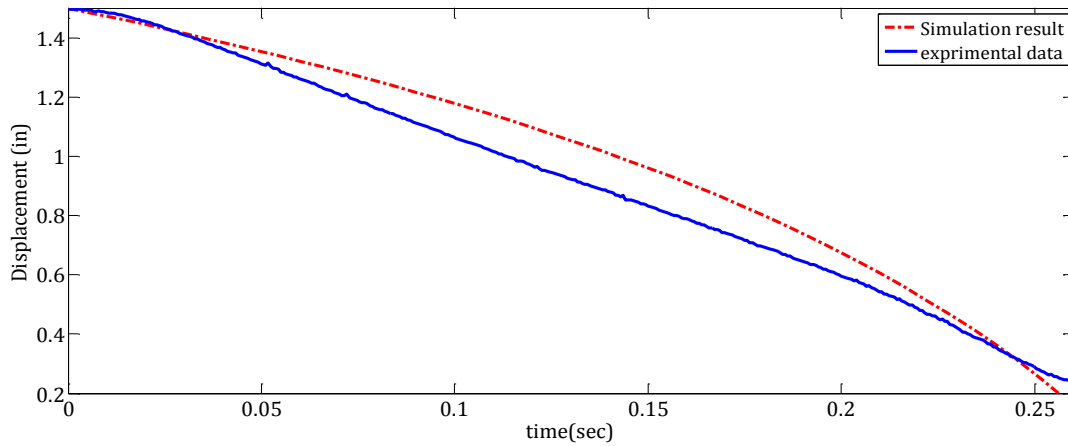


**Figure 5-14. Expansion time of square shape foam sample given in Table 5-1**

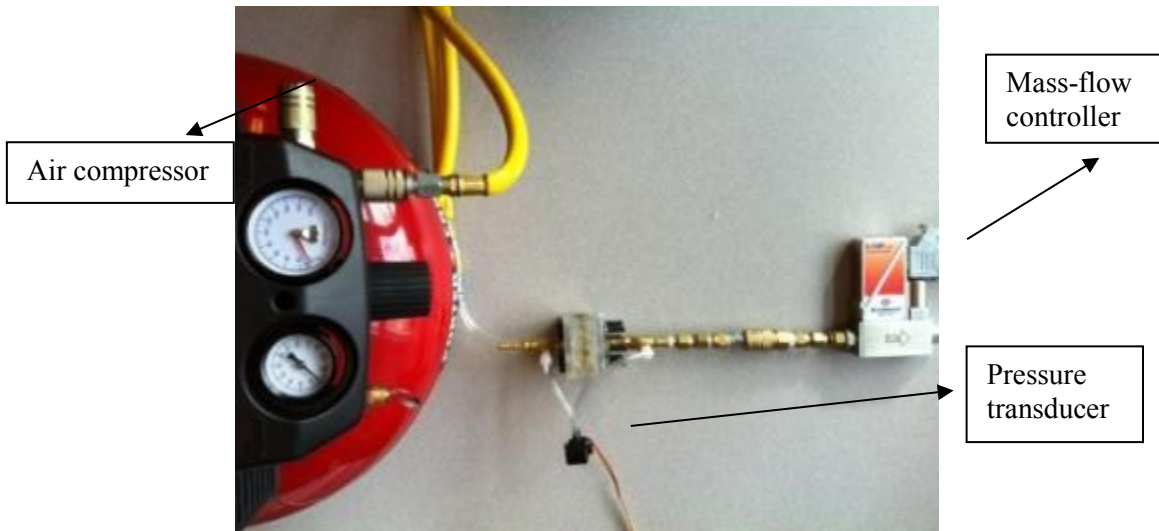
**Table 5-1. Physical parameters of open cell foam sample used**

Parameters	Description	Value
W	Width of the sample (in)	4.5
L	Length of the sample (in)	4.5
h	Height of the sample (in)	2
$\epsilon$	Porosity	.95
$K_0$	Permeability at zero strain ( $\text{in}^2$ )	$5\text{e-}6$
$B_0$	Inertia Coefficient at zero strain (in)	$1\text{e-}7$
$Y_0$	The maximum compression at time $t=0$ (in)	1.5

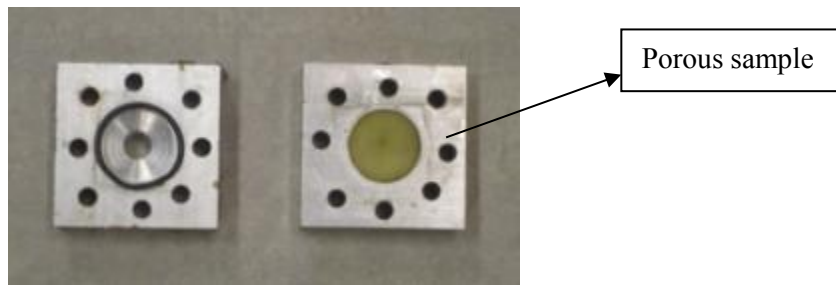
In Table 5-1, parameters  $K_0$  and  $B_0$  for the foam sample used in experiment and simulation were empirically obtained using the experimental test setup shown in Figure 5-15. A one inch diameter foam sample of Figure 5-15 (c) was placed between two plates which form an isolated chamber. Air with different flow rates is pushed through the porous medium. Different flow rates adjustment as well as their measurement was achievable using a mass-flow controller, model EI-Flow F-201CV, shown in Figure 5-15. At each flow rate, the pressure drop at positions before and after the foam sample was



measured by means of a differential pressure transducer, model PX137-005DV. Finally, a curve using Darcy equation (Equation (5-5)) was fitted to the empirical data plotted in Figure 5-16 and, therefore, parameters  $K_0$  and  $B_0$  were extracted.



(a)



(b)

**Figure 5-15. Test setup for measuring foam permeability and inertial coefficient, a) Experimental setup, b) a sealed isolated chamber containing the porous sample**

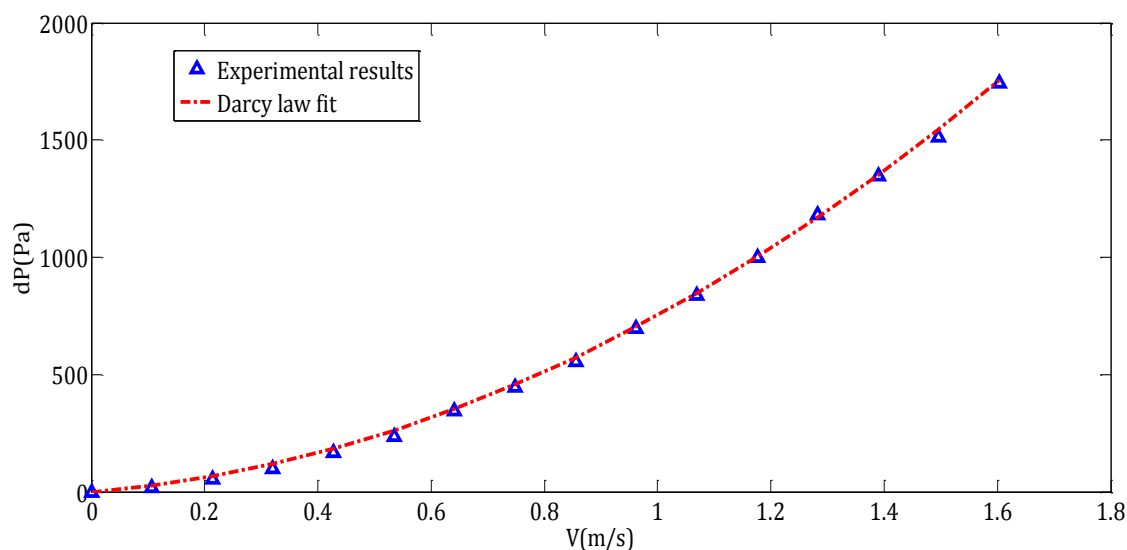


**Figure 5-16. Measurement of permeability and inertia coefficient of open cell foam**

### 5.3.1.3. Deployment Time Improvement

Although many factors such as polymeric foam stiffness, foam density, cell geometry, cell size porosity, and suitability of catalyst [63] may affect the expansion time significantly, physical modification such as the effect of air-duct channels cut out of the foam is the focus of this section. An attempt was made therefore to improve airflow inside the foam by cutting out channels that directed air throughout the foam sample. Several different air duct shapes were proposed and cut out of the foams by the laser cutter (Figure 5-17).

For consistency in data, each sample was tested three times using the experimental test setup described in Section 5.3.1.1. For better comparison of the different samples, the volume of the foam used remains the same, so the only factor affecting the rise times is the shape of the channels. In each case, the polymeric matrix stiffness is different because the cutting pattern varies (Figure 5-18 (a)); however, the reactant force due to internal friction between air and matrix is reduced during deployment (lower damping, that is, lower  $C$  and  $I$  values). The experimental results (Figure 5-18 (b)) indicate that a proper channel shape can significantly improve the

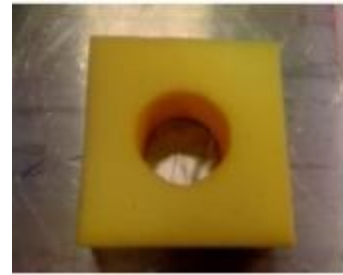
response time. The best result is obtained from a branching pattern that reduces the rise time from 290 ms to 120 ms.



(a)



(b)



(c)



(d)

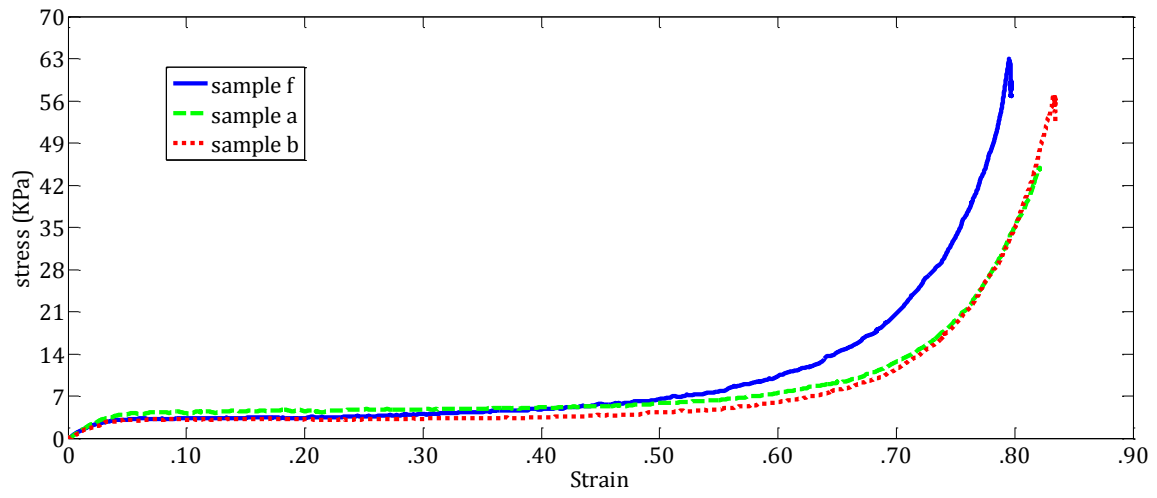


(e)

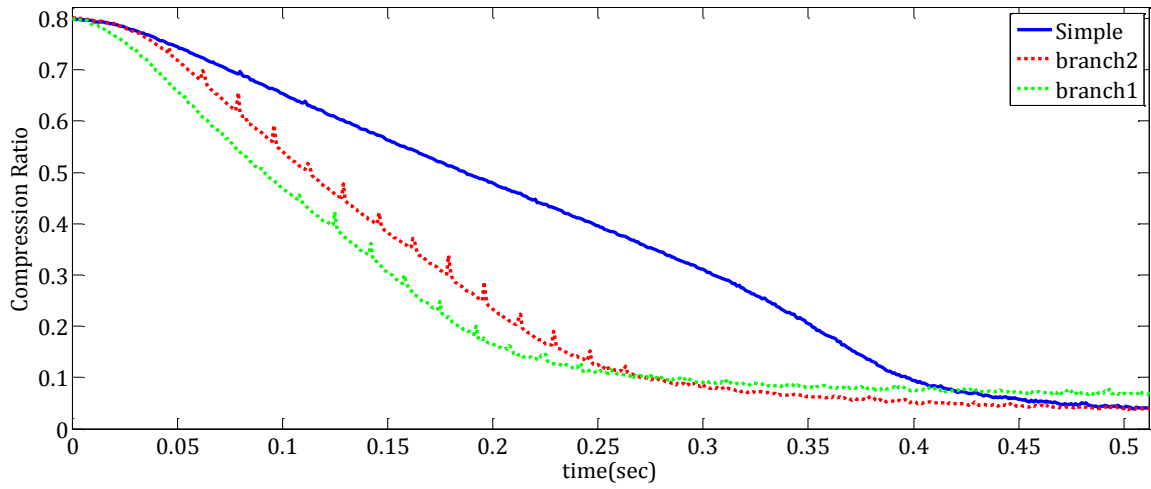


(f)

**Figure 5-17. Different foam sample patterns for improved expansion time**



(a)



(b)

**Figure 5-18. a) Stiffness of foam samples a, b and f in Figure 5-17, b) Expansion time of each sample**

### 5.3.2. *Impact Attenuation of Foam Airbag*

As previously stated and also intuitively found from contributing reaction forces within the foam, one might conclude that for high-rate foam compression like impact loading, the major source of foam reaction force comes possibly from the air inside the foam. It is crucial therefore that the proposed foam airbag be capable of holding sufficient air inside during the impact interval. To accomplish this, a cavity containing air can be made inside the foam and then sealed to ensure that air is adequately trapped inside the foam airbag during impact. The facts that support impact behavior of the novel foam airbag are very similar to those of the traditional airbag studied in Chapter 4. To briefly provide basic insights on foam airbag impact behavior, here a more simplified dynamics equation for air spring [35] is adopted for the foam airbag. For any airbag system similar to that shown in Figure 5-19, the reaction force on the impacted object can be obtained by this equation,

$$F_a = (P_A - P_{at})(A + A_z z) - (P_0 - P_{at})A \quad (5-11)$$

where  $A$  is the effective area of impact,  $A_z$  is the effective rate of change of  $A$ ,  $P_0$  is the internal pressure of the airbag,  $P_A$  is the dynamic pressure inside the airbag during the impact,  $P_{at}$  is the atmospheric pressure, and  $z$  is the vertical displacement of the impact object. Equation (5-11) should be modified for the foam airbag by replacing the initial pressure  $P_0$  with  $P_{at}$ . This is because the air pressure inside the cavity after deployment is atmospheric due to the underlying nature of the inflator system. Therefore, the equations can be modified as,

$$F_a = (P_A - P_{at})(A + A_z z) \quad (5-12)$$

Although a foam airbag might be sealed in order to trap air inside, it allows for some air escape during the impact. Assuming a polytropic process during the impact, the dynamic pressure inside the foam airbag can be expressed by,

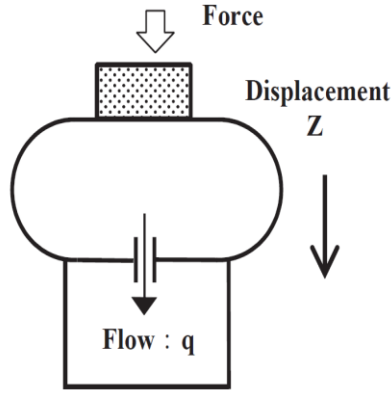


**Figure 5-19. Schematic model of an air spring**

$$P_A = P_0 \left\{ \frac{\rho_0 V_A - q}{\rho_0 (V_A - A_v z)} \right\}^{\kappa} \approx P_0 \left\{ 1 + \kappa \frac{\rho_0 A_v z - q}{\rho_0 V_A} \right\} \quad (5-13)$$

$$P_A = P_{at} \left\{ 1 + \kappa \frac{\rho_0 A_v z - q}{\rho_0 V_A} \right\} \quad (5-14)$$

where  $V_A$  is initial volume of foam airbag,  $\rho_0$  is the initial density of air,  $A_v$  is the rate of change in the volume of foam airbag during the impact,  $q$  is the airflow passing through the airbag system to the outer environment, and  $\kappa$  is the polytropic index. By substituting  $P_A$  in Equation (5-12), we have,

$$F_a = P_0 A k \left( \frac{\rho_0 A_v z - q}{\rho_0 V_A} \right) + (P_0 - P_{at}) A_z z \quad (5-15)$$

$$F_a = \frac{P_{at} \kappa A A_v}{V_A} z - \frac{P_{at} \kappa A}{\rho_0 V_A} q \quad (5-16)$$

Also, the linear relationship between the pressure inside the foam airbag and the rate of air escape can be expressed as,

$$R\dot{q} = P_A - P_{at} \quad (5-17)$$

where  $R$  is the resistance of the airbag system against airflow during the impact. This resistance in turn causes impact energy dissipation and reaction force reduction.

At the beginning of this investigation, a single cavity design as shown in Figure 5-20 was prepared. The main disadvantage of the single cavity design is that the air inside the cavity at atmospheric pressure can be easily compressed and, as a result, the airbag will not be stiff enough to prevent the object hitting the ground. Moreover, removing more foam to achieve a larger air cavity is to our disadvantage, since the thin foam can also easily bulge (larger  $A_v$ ), further contributing to the lack of pressure increase inside the bag. Therefore, bottoming out is a predictable phenomenon for the impacting object in this circumstance.

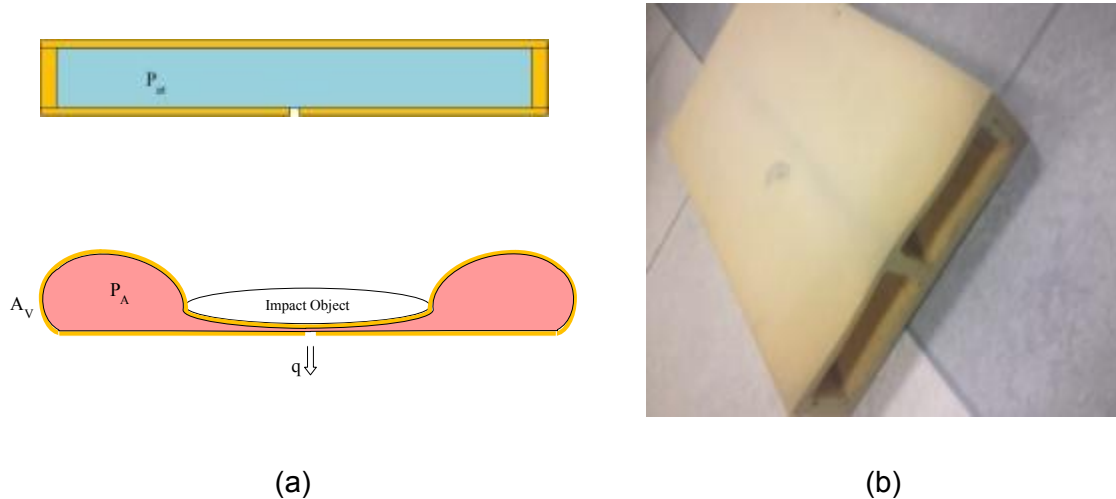


**Figure 5-20. A foam airbag with single cavity, a) schematic display, b) the fabricated foam airbag**

To address this problem, the implementation of a sectional design was proposed. As Figure 5-21 shows, the single cavity of Figure 5-20 is now divided into multiple sections all separated and sealed from each other. This new design solves the problem of air compressibility by localizing air compression in smaller volumes, and as a result,

the air pressure will quickly increase after the impact in each of the sections. This pressure will produce enough stiffness to avoid body organs hitting the ground. Moreover, the sectional configuration will mitigate the bulging problem by maintaining the pressurized air inside the neighboring sections to apply (approximately) equal push on the adjacent walls (bulging constraints) during impact. The ideal case occurs when the bulging of adjacent walls are negligible ( $A_v \approx 0$ ). In that case, the sections are similar to small pistons and act as parallel springs.

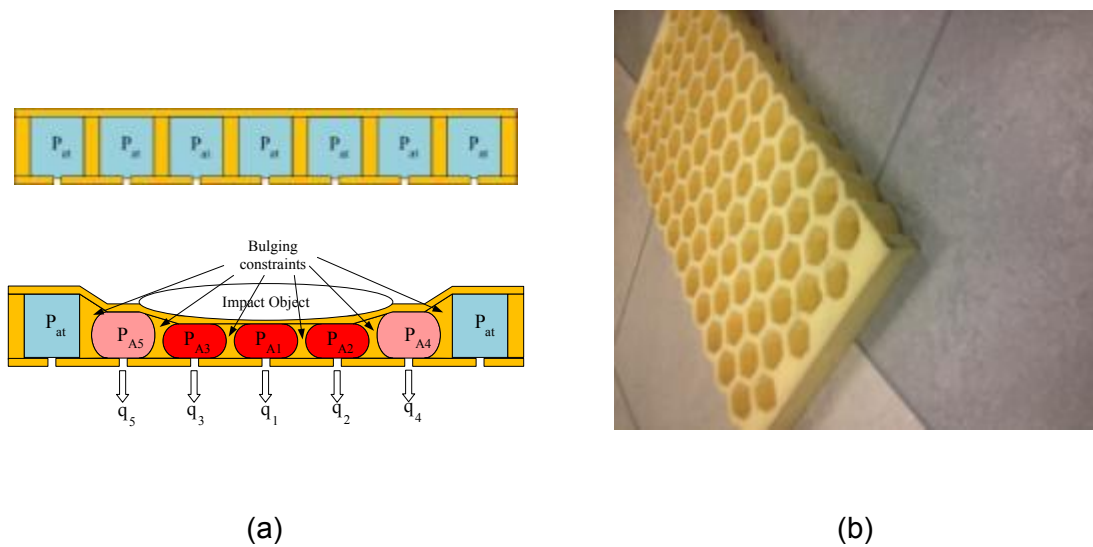


**Figure 5-21. A foam airbag with sectional cavity, a) schematic display, b) the fabricated foam airbag**

### 5.3.2.1. Experimental Results

To find the viability of the hypothesized sectional design, it was decided to perform the first series of experimental tests on a smaller scale version of the foam airbag in order to minimize material use as well as make fabrication and design easier. The pattern of the sections was first cut into the foam using a laser cutter and the walls of the sections were air-sealed by painting them with liquid latex (used for making facial cosmetic masks), which, after drying left a thin, flexible skin on the foam with minimal effect on foam compressibility [56]. A schematic exploded view of a four section-two Mylar ribs is shown in Figure 5-22 (a). In this design, the legs of the foam airbag are attached to the seats of the bottom and top foam plate, leaving sufficient gap for the air



to flow inside the sections (during rebound). When the airbag is struck by an impact, the excessive force pushes the plates on the foam airbag and closes gaps, so the air inside the sections becomes trapped, creating the airbag. This automatic foam based on the passive air flow management system makes it independent of the use of valves. To further explore the foam bulging problem and attain better force reductions, Mylar sheets, acting as ribs, were incorporated; these pose a physical restriction on the side walls, further reducing bulging and significantly contributing to the strength of the foam structure.

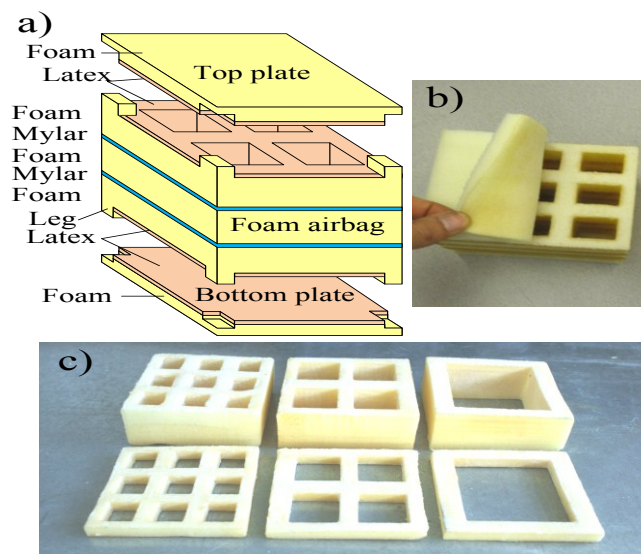


**Figure 5-22. a) foam airbag structure, b) a complete 9 section air cavity sample, c) 1, 4 and 9 section samples of  $\frac{1}{2}$  and 3 inch height**

To produce samples, we used low-density open-cell polyurethane foam with a density of  $2 \frac{lb}{ft^3}$  and porosity of 0.75. Samples of size 4"×3.5" (L×W) were made, and the effect of various design parameters including thickness, number of the Mylar layers, and number of sections on the performance (transmitted force and acceleration reduction) was investigated. The tests were conducted at various impact intensities using a 9-lb weight (close to adult human head weight) in a conventional drop test article similar to what was used for airbag impact testing described in Chapter 4. This test apparatus is

also shown in Figure 5-23. The experimental results and effects of a few design parameters mentioned above are briefly discussed in the following sections.

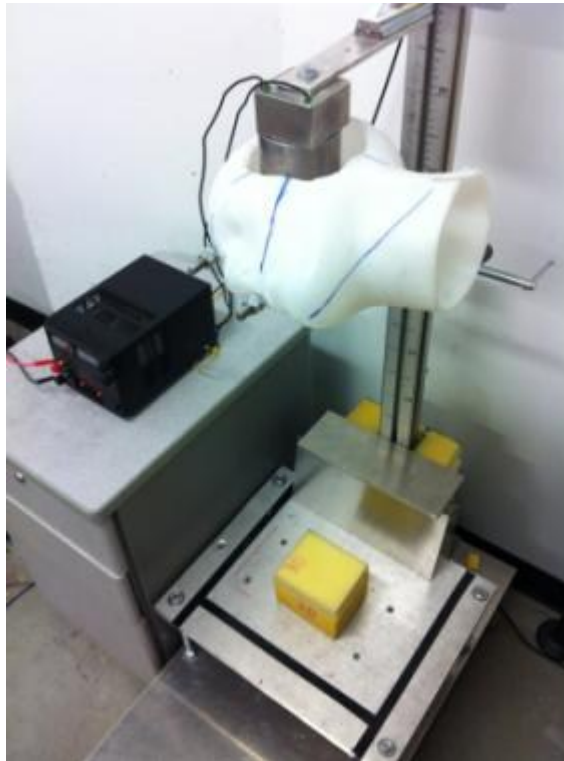


**Figure 5-23. A drop test setup for measuring impact isolation performance of foam airbag samples**

- **Effect of Mylar Rib**

As previously stated, the primary goal of a Mylar rib is to pose a restriction on the foam airbag walls so as to reduce the bulging of the airbag during the impact. However, it should be noted that the bulging phenomenon described here is due mainly to the compressed air pushing the walls outward to reduce the internal pressure by increasing the container volume. The force data from impact tests on both sealed and non-sealed samples are plotted in Figure 5-24. As observed in this figure, by adding a Mylar rib to nine-section samples with the internal walls sealed, a reduction of 45% in impact force is achieved. On the other hand, however, adding a Mylar rib to a simple foam sample (not sealed) contributes only a 10% force reduction. Indeed, in a simple foam sample, air can

easily escape through the porous medium because foam is compressed and, thus, there is no push against the wall, so no bulging occurs. Clearly in this case, the Mylar rib has minimal effect on holding air in the airbag.

Furthermore, by comparing force values for simple foam samples during the impact with those associated with a sealed foam sample as shown in Figure 5-24, one easily finds a promising role of air trapped inside the foam in impact attenuation. In fact, force for a simple foam sample during the impact is very similar to force for a typical foam compression shown in Figure 5-5, which indicates that the solid foam structure just by itself cannot be sufficiently effective in force attenuation.

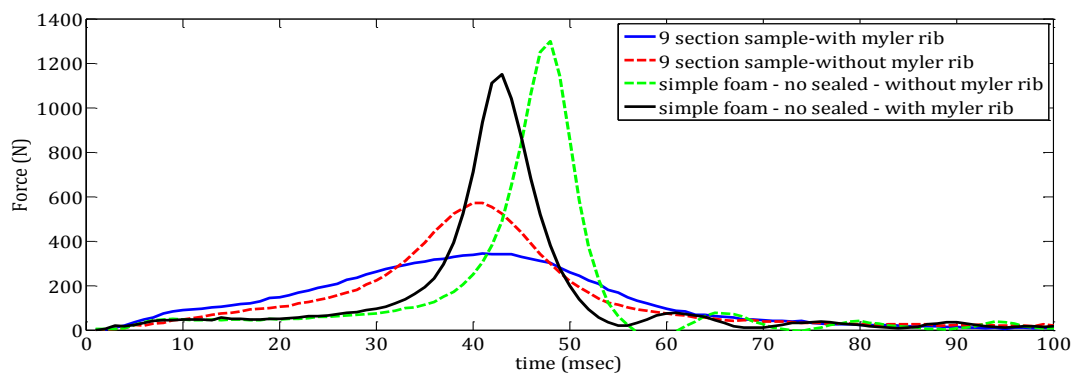


**Figure 5-24. Comparison of Mylar effect on a sealed foam airbag with a simple foam sample,  $h_0 = 30\text{cm}$**

- **Effect of Sectional Configuration**

Each isolated section incorporated in a foam structure is hypothesized to have two effects on improving force reduction: 1) localizing the air compression in smaller volumes so as to further increase the internal pressure, and 2) reducing the bulging effect as compressed air in two adjacent sections applies equal push to the common wall; ideally, therefore, the wall can be considered a rigid frame. However, the number of sections in this configuration can be optimized based on the impact intensity for greatest force reduction, a point better illustrated in Figure 5-25, where the force results for different sectional configurations (one section, four sections and nine sections) are plotted for three drop heights. As this figure shows, for lower drop height (lower impact

intensity), force results associated with three samples are in approximately the same range. As the drop height increases, the one-section design reveals better impact attenuation than the other two configurations. In fact, for this specific impact energy, the one-section design has the chance to keep the internal pressure at lower levels through the bulging happening yet is stiff enough for absorption of sufficient energy. On the other hand, in four-section and nine-section designs, the air trapped inside becomes unnecessarily pressurized and, therefore, more force transmitted to the mass can be expected. As the drop height further increases, however, the one-section design is no longer capable of holding inside enough pressurized air to absorb the entire mass impact energy within the foam thickness, and, therefore, it partly bottoms down. This in turn leads to a higher peak force than that corresponding to the other two sectional patterns.

Finally, the experimental results obtained for different thicknesses of foam, simple foam without sealing, and fully sealed foam are compared in Figure 5-26. The force attenuation performance associated with a 3 inch foam sample with a one-section configuration reveals a promising result, one completely in line with our findings in Chapter 3 regarding the “Effective Operating Region” concept. As a matter of fact, in this case the near square-wave impact impulse can be observed, which is mainly occurring because this design is capable of releasing excessive pressurized air so as to avoid experiencing higher internal pressures. This concept is also highlighted by observing the results corresponding to a fully sealed sample that has no chance of releasing compressed air properly, and thus, higher forces are anticipated. It should be noted, however, that if impact intensity increases considerably, the one-section pattern may not be optimum, because in that case, the chance of bottoming down greatly increases compared with a firmer design such as a fully sealed sample. *Therefore the impact intensity is of primary importance in optimum design configuration, that is, a design which assures the absorption of the total impact energy within its working space while it keeps the internal pressure (force) minimal.* After all, Figure 5-26 shows a promising 80% reduction in impact force (from 1480 N to 320 N) for a 15-j impact energy, implementing an appropriate foam airbag design. The reductions would be even more

pronounced if they were compared with results from unpadded impact tests (such tests were not performed, due to potential damage to our test setup).

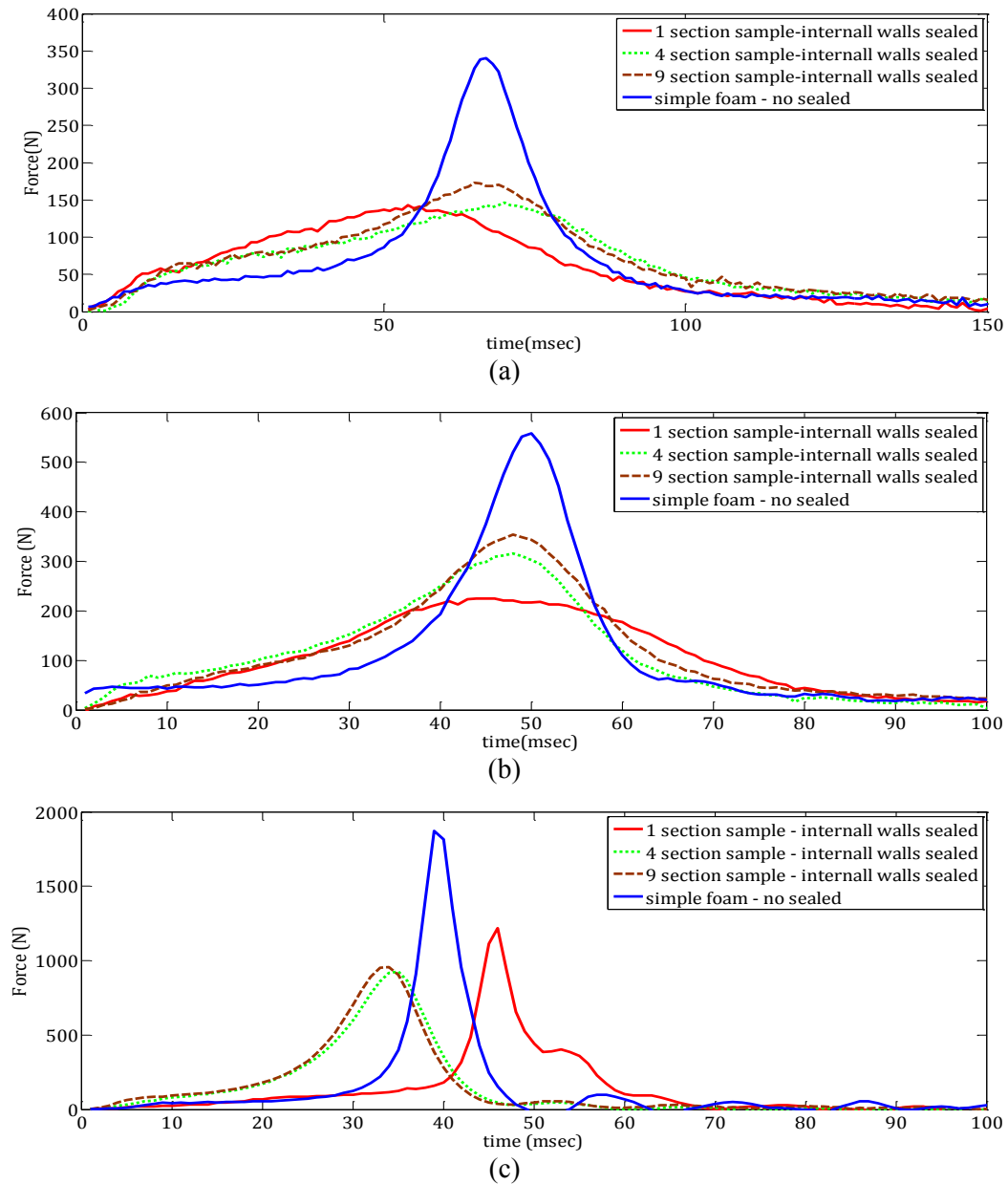


**Figure 5-25. Effect of sectional design for foam airbags with 3" thickness, a)  $h_0 = 10 \text{ cm}$ , b)  $h_0 = 30 \text{ cm}$ , c)  $h_0 = 40 \text{ cm}$**

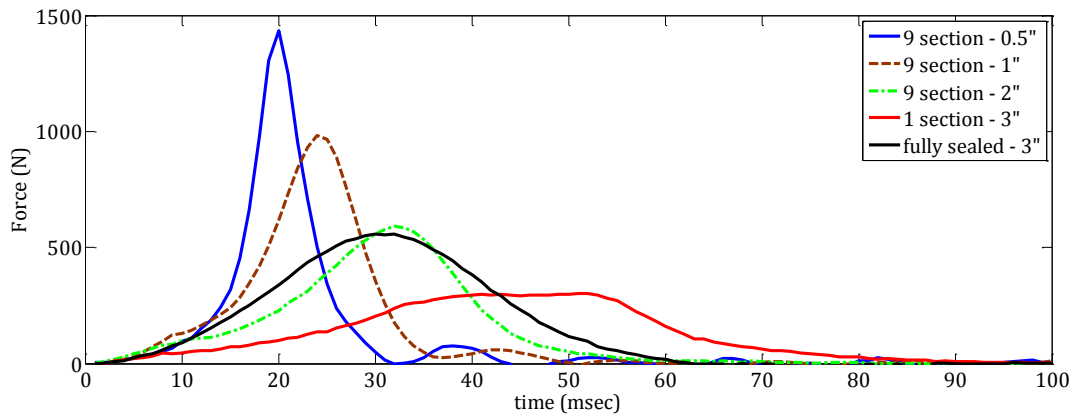


**Figure 5-26.** Comparison of foam reduction in foam samples with different thicknesses,  $h_0 = 30\text{cm}$

## 5.4. Chapter Summary

A simple technique that uses compressed open-cell foam as the self-inflator airbag is proposed in this chapter. In this novel airbag, foam absorbs air for expansion and inflates the airbag. Analytical dynamic modelling of open-cell foam was investigated through previous works and validated by experimental tests. In addition, two major challenges with the proposed airbag including deployment time and impact attenuation were addressed. Innovative designs for enhanced performance of the foam are proposed and investigated experimentally. Also, the implication of “Effective Operating Region” in these designs is clearly observed through the experimental results and is proved to be attainable and significantly influential in impact attenuation.

## 6. Conclusion and Future Work

The work described in this thesis can be considered an important step toward achieving effective impact attenuation in human impact-induced injuries through introducing and establishing optimal conceptual designs. The resulting conceptual designs were put into practice by designing two different airbags with enhanced performance in order to validate the viability of the fundamental concepts in effective energy management during impact absorption.

In the second chapter, three simplified and fundamental airbag models were considered, and, in each case, the physical parameters of the system were represented in terms of natural frequency and damping coefficient as the main design variables. The design charts for each case were then developed, providing the primary and fundamental design considerations for effective injury prevention. It was shown that the lower Head Injury Criterion (HIC) values are achievable simply by permitting higher deflections of the isolator mechanisms considered there.

In the third chapter, the hypothetical “ideal isolator” was first explored, and the feasibility of using such a design was then investigated by introducing and establishing the concept of “Effective Operating Region.” This concept concerns mainly effective energy management during the impact, which can be simply achieved through appropriate potential energy release from the system. By applying this conceptual design to the isolators discussed mainly in Chapter 2, considerable improvement in impact attenuation was attainable. The introduced concept was mathematically formulated, and some simple yet practical case studies were analyzed by using this concept.

In Chapter 4, the more complicated modelling of airbags from the standpoint of fluid mechanics was developed based on works of previous researchers. Moreover, the

venting arrangement was implemented to the airbag in order to employ the effective operating region concept for the existent airbags. This was experimentally tested, and the effect of different parameters such as orifice cross area, initial pressure and opening pressure on the performance of this airbag design was analyzed by means of basic concepts developed in Chapter 3.

Finally, in Chapter 5, an innovative self-inflator foam airbag was introduced, which proposes a novel solution against all deleterious effects associated with conventional airbags. A simplified model of the foam airbag is mathematically established, and the challenges and risks arising with this novel foam airbag are addressed. These challenges are associated mainly with the deployment time and the force attenuation performance of the airbag. Detailed investigations of each aspect are provided through mathematical modelling as well as properly designed experiments. As results obtained from the conducted experiments reveal, the promising implication of “Effective Operating region” is easily observed in foam airbag performance.

In future work, however, some of the obstacles encountered during this research will be overcome. The more sophisticated test apparatus needs to be developed in to achieve minimal error affecting the impact results. For instance, to truly evaluate the head injury criterion associated with fall-induced injury and isolator performance assessment, the perfect free fall without any contact with the surrounding environment needs to be arranged. Besides, materials and mechanical properties of headform, close to human head should be considered in both experimental and simulation tests for more reliable results. Furthermore, the conceptual design configuration explained in Chapter 3 for multi-stage energy release should be built to show the simplicity, yet viability, of the proposed design based on an effective operating region concept. In addition, a large-scale prototype of a foam airbag needs to be made to demonstrate the practicality of the proposed airbag in real-case situations as an alternative to conventional airbags, where they cannot be used due mainly to difficulties stemming from their inflation mechanism.



## References

- [1] L. Krantz, *What The Odds Are*. New York: Harper Perennial, 1992.
- [2] C. Baudoin, P. Fardellone, K. Bean, A. Ostertag-Ezembe, and F. Hervy, "Clinical outcomes and mortality after hip fracture: a 2-year follow-up study.," *Bone*, vol. 18, no. 3 Suppl, p. 149S–157S, Mar. 1996.
- [3] M. E. Tinetti, M. Speechley, and S. F. Ginter, "Risk factors for falls among elderly persons living in the community.," *The New England journal of medicine*, vol. 319, no. 26, pp. 1701–7, Dec. 1988.
- [4] V. Scott, L. Wagar, and S. Elliott, "Falls & Related Injuries among Older Canadians: Fall- related Hospitalizations & Intervention Initiatives," 2010.
- [5] J. J. Hindmarsh and E. H. Estes, "Falls in older persons. Causes and interventions.," *Archives of internal medicine*, vol. 149, no. 10, pp. 2217–22, Oct. 1989.
- [6] "WorkSafeBC Statistics," 2011.
- [7] H. Xiang, A.-M. Chany, and G. A. Smith, "Wheelchair related injuries treated in US emergency departments.," *Injury prevention : journal of the International Society for Child and Adolescent Injury Prevention*, vol. 12, no. 1, pp. 8–11, Feb. 2006.
- [8] "National Electronic Injury Surveillance System (NEISS) On-line." [Online]. Available: <http://www.cpsc.gov/library/neiss.html>. [Accessed: 01-Nov-2012].
- [9] "National Highway Traffic Safety Administration (NHTSA)." [Online]. Available: <http://www.nhtsa.gov/>. [Accessed: 01-Nov-2012].
- [10] R. L. Kirby and S. A. Ackroyd-Stolarz, "Wheelchair safety--adverse reports to the United States Food and Drug Administration.," *American journal of physical medicine & rehabilitation / Association of Academic Physiatrists*, vol. 74, no. 4, pp. 308–12, 1995.
- [11] S. H. Advani, A. K. Ommaya, W.-J. Yang, R. COLLINS, K. Kivity, D. Kalliers, R. Mathern, G. Schmidt, D. Mohan, D. G. Kingn, W. Johnson, A. G. Mamalis, S. R. Reid, N. Perrone, K. V. Frolov, B. A. Potemkin, E. Rohl, H. Wolff, A. BHATTACHARYA, D. N. Ghista, and D. P. Garg, *Human Body Dynamics:*

*IMPACT, OCCUPATIONAL AND ATHLETIC ASPECTS*. OXFORD UNIVERSITY PRESS, 1982, pp. 3–37.

- [12] E. S. Gurdjian, V. L. Roberts, and L. M. Thomas, "Tolerance curves of acceleration and intracranial pressure and protective index in experimental head injury.," *The Journal of trauma*, vol. 6, no. 5, pp. 600–4, Sep. 1966.
- [13] E. S. Gurdjian, H. R. Lissner, F. R. Latimer, B. F. Haddad, and J. E. Webster, "Quantitative determination of acceleration and intracranial pressure in experimental head injury," *Neurology*, vol. 3, no. 6, pp. 417–23, Jun. 1953.
- [14] E. S. Gurdjian, V. R. Hodgson, W. G. Hardy, L. M. Patrick, and H. R. Lissner, "Evaluation of the Protective Characteristics of Helmets in Sports," *The Journal of trauma*, vol. 4, pp. 273–286, May 1964.
- [15] J. Versace, "A review of the severity index," *SAE Technical Paper 710881*, 1971.
- [16] J. Hutchinson, M. J. Kaiser, and H. M. Lankarani, "The Head Injury Criterion (HIC) functional," *Applied Mathematics and Computation*, vol. 96, no. 1, pp. 1–16, Oct. 1998.
- [17] D. R. Lemmon and R. L. Huston, "Automobile hood/fender design optimization for improved pedestrian head impact protection," in *20th Design Automation Conference Proceedings 69 (2)*, 1994, pp. 569–577.
- [18] J. Wu and B. Beaudet, "Optimization of Head Impact Waveform to Minimize HIC," in *SAE International 2007 World Congress*, 2007.
- [19] P. G. Young, "An analytical model to predict the response of fluid-filled shells to impact—a model for blunt head impacts," *Journal of Sound and Vibration*, vol. 267, no. 5, pp. 1107–1126, Nov. 2003.
- [20] M. Heydari and S. Jani, "An ellipsoidal model for studying response of head impacts.," *Acta of bioengineering and biomechanics*, vol. 12, no. 1, pp. 47–53, Jan. 2010.
- [21] C. Deck, R. Willinger, and D. Baumgartner, "Helmet optimisation based on head-helmet modelling," in *Proceed of OPTI Conf. Detroit*, 2003.
- [22] T. D. Proctor and F. J. Rowland, "Development of Standards for Industrial Safety Helmets - The State of The Art," *Journal of Occupational Accidents*, vol. 8, pp. 181–191, 1986.
- [23] C. M. Vieira, H. A. Almeida, I. S. Ferreira, J. O. Vasco, P. J. Bártoło, B. Ruben, and S. P. Santos, "Development of an Impact Absorber for Roadside Barriers," Leiria, Portugal, 2008.

- [24] M. R. Shorten and C. Creager, "Optimisation of the shock attenuating properties of playground surfaces," in *Proc XVII Congress ISB*, 1999, p. 541.
- [25] T. Tamura, T. Yoshimura, M. Sekine, M. Uchida, and O. Tanaka, "A wearable airbag to prevent fall injuries.," *IEEE transactions on information technology in biomedicine: a publication of the IEEE Engineering in Medicine and Biology Society*, vol. 13, no. 6, pp. 910–4, Nov. 2009.
- [26] M. N. Nyan, F. E. H. Tay, and E. Murugasu, "A wearable system for pre-impact fall detection.," *Journal of biomechanics*, vol. 41, no. 16, pp. 3475–81, Dec. 2008.
- [27] W. D. Pilkey, D. V. Balandin, and N. N. Bolotnik, *Injury Biomechanics and Control: Optimal Protection from Impact*. Wiley, 2009, p. 304.
- [28] D. A. Peters, "Optimum Spring-Damper Design For Mass Impact," *SIAM Review*, vol. 39, no. 1, pp. 118–122, Jan. 1997.
- [29] N. Oda and S. Nishimura, "Vibration of Air Suspension Bogies and Their Design," *Bulletin of JSME*, vol. 13, no. 55, pp. 43–50, Jan. 1970.
- [30] S. E. Arjmand Boroujeni, "Inflatable Hip Protectors," Simon Fraser University, 2012.
- [31] R. Alkhatib, G. Nakhaie Jazar, and M. . Golnaraghi, "Optimal design of passive linear suspension using genetic algorithm," *Journal of Sound and Vibration*, vol. 275, no. 3–5, pp. 665–691, Aug. 2004.
- [32] N. Baldanzini, D. Caprioli, and M. Pierini, "Designing the Dynamic Behavior of an Engine Suspension System Through Genetic Algorithms," *Journal of Vibration and Acoustics*, vol. 123, no. 4, p. 480, 2001.
- [33] S. N. Robinovitch, W. C. Hayes, and T. A. McMahon, "Distribution of contact force during impact to the hip," *Annals of Biomedical Engineering*, vol. 25, no. 3, pp. 499–508, May 1997.
- [34] N. Eslaminasab, "Development of a Semi-active Intelligent Suspension System for Heavy Vehicles," University of Waterloo, Ontario, Canada, 2008.
- [35] K. Shimosawa and T. Tohtake, "An Air Spring Model with Non-Linear Damping for Vertical Motion," *QR of RTRI*, vol. 49, no. 4, pp. 209–214, 2008.
- [36] J. Arora, *Introduction to Optimum Design*. Academic Press, 2004, p. 728.
- [37] "AVM Industries Gas Springs and Lift Supports Provider." [Online]. Available: [http://www.avmind.com/std\\_dampers.asp](http://www.avmind.com/std_dampers.asp). [Accessed: 01-Nov-2012].

- [38] "Compression Springs | Stainless Steel Springs | Lee Spring." [Online]. Available: [http://www.leespring.com/compression\\_spec.asp?springType=C&forWhat=Search](http://www.leespring.com/compression_spec.asp?springType=C&forWhat=Search). [Accessed: 01-Nov-2012].
- [39] "Dictator Technik GmbH - Oil dampers, door dampers, closing springs, special doorclosers." .
- [40] "Shock Absorbers, Fluid Dampers, Liquid Springs, Crane Bumpers." .
- [41] L. Lamb and T. B. Hoshizaki, "Deformation mechanisms and impact attenuation characteristics of thin-walled collapsible air chambers used in head protection.," *Proceedings of the Institution of Mechanical Engineers. Part H, Journal of engineering in medicine*, vol. 223, no. 8, pp. 1021–31, Nov. 2009.
- [42] K. Fukaya and M. Uchida, "Protection against impact with the ground using wearable airbags.," *Industrial health*, vol. 46, no. 1, pp. 59–65, Jan. 2008.
- [43] J. B. Esgar and W. C. Morgan, *Analytical study of soft landings on gas-filled bags*. Washington, D.C. :: National Aeronautics and Space Administration ;, 1960.
- [44] J. K. Cole and D. E. Wayne, "BAG: A code for predicting the performance of a gas bag impact attenuation system for the Pathfinder lander," *NASA STI/Recon Technical Report*, Nov. 1993.
- [45] K. Annamalai, I. K. Puri, and M. A. Jog, *Advanced Thermodynamics Engineering (Computational Mechanics and Applied Analysis)*. CRC Press, 2001, p. 439.
- [46] F. Petruzella, *Programmable Logic Controllers*, 4th Editio. McGraw-Hill Publications, 2011.
- [47] D. E. Raymond, R. D. Catena, and T. R. Vaughan, "Biomechanics and injury risk assessment of falls onto protective floor mats.," *Rehabilitation nursing: the official journal of the Association of Rehabilitation Nurses*, vol. 36, no. 6, pp. 248–54.
- [48] J. A. Pearlman, K. G. Au Eong, F. Kuhn, and D. J. Pieramici, "Airbags and eye injuries: epidemiology, spectrum of injury, and analysis of risk factors.," *Survey of ophthalmology*, vol. 46, no. 3, pp. 234–42.
- [49] I. Hendrikx, "Burn injury secondary to air bag deployment," *Journal of the American Academy of Dermatology*, vol. 46, no. 2, pp. S25–S26, Feb. 2002.
- [50] G. Wu, "Distinguishing fall activities from normal activities by velocity characteristics.," *Journal of biomechanics*, vol. 33, no. 11, pp. 1497–500, Nov. 2000.

- [51] R. E. Skochdopole and L. C. Rubens, "Physical Property Modifications of Low-Density Polyethylene Foams," *Journal of Cellular Plastics*, vol. 1, no. 1, pp. 91–96, Jan. 1965.
- [52] U. Dunger, H. Weber, and H. Buggisch, "A Simple Model for a Fluid-Filled Open-Cell Foam," *Transport in Porous Media*, vol. 34, pp. 269–284, 1999.
- [53] N. C. Hilyard and L. K. Djiauw, "Observations on the Impact Behaviour of Polyurethane Foams; I. The Polymer Matrix," *Journal of Cellular Plastics*, vol. 7, no. 1, pp. 33–42, Jan. 1971.
- [54] N. C. Hilyard, "Observations on the Impact Behaviour of Polyurethane Foams :II. The Effect of Fluid Flow," *Journal of Cellular Plastics*, vol. 7, no. 2, pp. 84–90, Jan. 1971.
- [55] C. W. Kosten and C. Zwikker, "Properties of Sponge Rubber as a Material for Damping Vibration and Shock," *Rubber Chemistry and Technology*, vol. 12, no. 1, pp. 105–111, Mar. 1939.
- [56] K. C. Rusch, "Dynamic Behavior of Flexible Open-cell Foams," The University of Akron, 1965.
- [57] C. Fitzgerald, I. Lyn, and N. J. Mills, "Airflow through Polyurethane Foams with Near-Circular Cell-Face Holes," *Journal of Cellular Plastics*, vol. 40, no. 2, pp. 89–110, Mar. 2004.
- [58] M. a. Dawson, J. T. Germaine, and L. J. Gibson, "Permeability of open-cell foams under compressive strain," *International Journal of Solids and Structures*, vol. 44, no. 16, pp. 5133–5145, Aug. 2007.
- [59] J. T. Gostick, M. W. Fowler, M. D. Pritzker, M. a. Ioannidis, and L. M. Behra, "In-plane and through-plane gas permeability of carbon fiber electrode backing layers," *Journal of Power Sources*, vol. 162, no. 1, pp. 228–238, Nov. 2006.
- [60] S. W. White, S. K. Kim, A. K. Bajaj, and P. Davies, "Experimental Techniques and Identification of Nonlinear and Viscoelastic Properties of Flexible Polyurethane Foam," *Nonlinear Dynamics*, vol. 22, pp. 281–313, 2000.
- [61] R. Deng, P. Davies, and a. K. Bajaj, "A nonlinear fractional derivative model for large uni-axial deformation behavior of polyurethane foam," *Signal Processing*, vol. 86, no. 10, pp. 2728–2743, Oct. 2006.
- [62] A. H. Nayfeh and D. T. Mook, *Nonlinear Oscillations*. JOHN WILEY & SONS, INC., 1995.

- [63] R. E. Jones and G. Fesman, "Air Flow Measurement and Its Relations to Cell Structure, Physical Properties, and Processability for Flexible Urethane Foam," *Journal of Cellular Plastics*, vol. 1, no. 1, pp. 200–216, Jan. 1965.

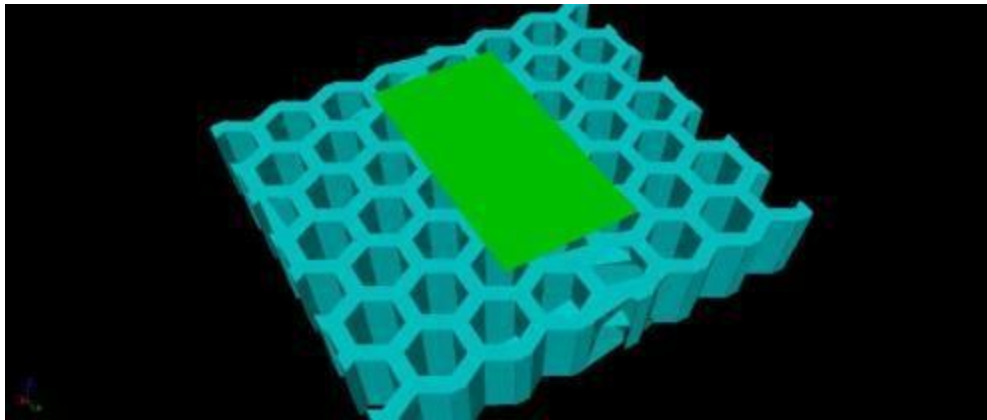
## **Appendices**

## Appendix A.

### MADYMO Simulations

Applying injury protection simulations will assist to identify the performance of the airbag before making a full size prototype of it. This will save significant time and money which is required for fabricating and testing full size prototype of the foam airbag system. Computer simulations using MADYMO software have been used in the past for generating real-life accidents that lead to injuries, including head injury. MADYMO is a powerful simulation package which has been used extensively for automotive crash simulations and has been validated experimentally. The software has also the pre-built anthropomorphic test dummy (ATD) model. The ATDs in MADYMO are constructed of ellipsoids, which can simulate the contact surfaces during impact more accurately.

In this study it was tried to use MADYMO to simulate larger scale of foam airbag and measure the force transmitted to the head during the impact. To do simulations, a compatible model of the airbag was imported in the MADYMO environment. To this end, a 3D model of 9" \*9"\*3" foam airbag with hexagonal sections in Solidworks was designed and then a finite element modelling of that was created using Hypermesh software. The created FE model along with the stress-strain function obtained in Figure 5-5(b) were imported to the MADYMO. The imported FE-model in MADYMO is shown in **Error! Reference source not found..** The main reason underlying the choice of hexagonal sections is due to the significantly better compressibility attained via this design.

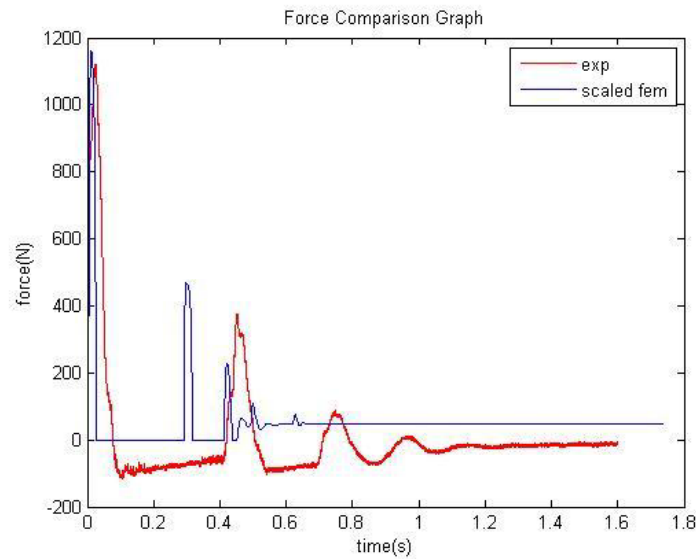


**The FE model of foam airbag imported in MADYMO**

In the MADYMO program, the foam airbag was hit by a 5 kg ellipsoid representing the headform used in experiments floating 50 cm above the finite element foam model. To simplify the simulation, the foam was constrained at the bottom in all degrees of freedom to minimize error in contact between the aluminium plate and foam model. To compare to the force sensor data, MADYMO is able to output contact forces between two surfaces, including multi body and finite elements. Another required parameter to run the simulation was the damping coefficient for foam modelling. This coefficient was simply estimated and changed to best fit experimental result



conducted in accordance with this foam sample. The results obtained from MADYMO and those from experimental test are compared in figure below.



#### **Comparison of MADYMO simulation results with experimental results of measured force for foam airbag**

Although, the simulation result to a good extent can follow the dynamic trend observed in force experienced by the head in experimental test, However further improvement for modelling foam airbag in MADYMO deems essential. This is mainly because here the stress-strain curve inputted to the software as the load function, has obtained in quasi-static situation and it does not account for air entrapped inside the foam. In fact, the key role of air which is hypothesized to be the major contributing factor in impact attenuation of foam airbag is largely ignored. Therefore, for improved results, the air component as the major contributing source in force reaction of foam airbag shall be modelled via CFD based softwares and incorporated into the model for more accurate results.

## Appendix B.

### MATLAB Code for Airbag Impact Response

```
clear all
clc

%% Problem Parameters

g=9.8;
m=5.8; % Head mass
A_orifice_base=5.0671e-4*1; % valve sectional area installed on the airbag
D=.3; % Cylindrical airbag diameter
L=.3; % Cylindrical airbag length
P0_base=(101)*1000;
dt=.0001;
t_final=1.5;
P_burst_base=101e3-1;
h0_base=.1;

Nu_A_orifice=50; % Number of valve sectional areas
Nu_h0=4; % Number of drop heights
Nu_P_burst=100; % Number of opening pressures
Nu_P0=10; % Number of initial pressures

P0=P0_base;
P_burst=P_burst_base;
h0=h0_base+0;

%% Impact Response Calculation
for ii=1:1:Nu_P0
    P0(ii)=P0_base+2e3*(ii-1);

    for jj=1:1:Nu_h0
        jj
        tic
        h0(jj)=h0_base+.2*(jj-1);

        for ll=1:1:Nu_P_burst(ii)
            P_burst=P0(ii)+1e3*(ll-1)-1;
            for kk=1:1:Nu_A_orifice
                clear T
                clear X
                clear U
                clear A
                clear P
                clear T_desired
                clear X_desired
                clear U_desired
                clear A_desired
```

```

kk;
A_orifice(kk,ll,jj,ii)=0+(kk-1)*.5*A_orifice_base;

out=Newton_iteration_function(A_orifice(kk,ll,jj,ii),P0(ii),P_burst,h0(jj),m,t_
final,dt);

T=out(1,:); % Time vector from impact response
X=out(2,:); % Position vector from impact response
U=out(3,:); % Velocity vector from impact response
A=out(4,:); % Acceleration vector from impact response
P=out(5,:); % Pressure vector from impact response

clear U_fb
clear T_fb
clear X_fb
clear T_first_bounce_desired
FB(kk,ll,jj,ii)=0; %matrix to save cases that firs_bounce
                    happens

    impact_number=1;
    for i=1:1:length(T)-1
        if (abs(A(i+1)*g+g)<.1)
            if ((-A(i+1)+A(i))*g)>.001
                U_fb(impact_number)=U(i+1);

                X_fb(impact_number)=X(i+1);

                if U_fb(impact_number)<0
                    T_fb(impact_number)=(i-1)*dt;
                    impact_number=impact_number+1;

                    FB(kk,ll,jj,ii)=1;
                end
            end
        end
    end

    if FB(kk,ll,jj,ii)==1
        T_first_bounce_desired=0:dt:T_fb(1);
        nn=length(T_first_bounce_desired);
        X_first_bounce_desired=X(1:1:nn);
        X_max_FB(kk,ll,jj,ii)=max(X_first_bounce_desired);
        U_FB(kk,ll,jj,ii)=U_fb(1);
    else
        X_max_FB(kk,ll,jj,ii)=max(X);
        U_FB(kk,ll,jj,ii)=-1; % It means no bounce back
                               happens
    end
end

if A_orifice(kk,ll,jj,ii)==0
    T_desired=T_first_bounce_desired;
    nn=length(T_first_bounce_desired);

```

```

        X_desired=X(1:1:nn);
        U_desired=U(1:1:nn);
        A_desired=A(1:1:nn);
    else
        T_desired=T;
        X_desired=X;
        U_desired=U;
        A_desired=A;
    end

%% HIC Calculation
n=length(T_desired);
v = cumtrapz(T,A);
hic = -inf;
for it = 1:n-1
    for jt = it+1:n
        if (T_desired(jt)-T_desired(it))<(.015) %
            h = (T_desired(jt)-T_desired(it))*((v(jt)-
                v(it))/(T_desired(jt)-T_desired(it)))^2.5;
            if h > hic
                hic = h;
            end
        end
    end
end

HIC(kk,ll,jj,ii)=hic; % HIC value
A_max(kk,ll,jj,ii)=max(A_desired); % Peak acceleration
U_end(kk,ll,jj,ii)=U(end); % Velocity of head at end stroke
if(U(end)>=U(1))
    break;
end

end
toc
end

function out = Newton_iteration_function( A_th,P0,P_burst,h0,m,t_final,dt)

clc
clear x
clear u
clear P
clear a
clear V
clear Afp
clear ro
clear w
clear u_fb
clear t_fb
clear first_bounce
clear t

```

```

g=9.8;

m=5.8;
A_th=5.0671e-4*5;
P0=(101)*1000;
dt=2e-4;
t_final=1.5;
a_opening_th=-1.01*g;
P_burst=101e3-1;
h0=.4;
D0=.3;
L=.3;

ro=1.3; % Air density (kg/m^3)
V_bag0=pi*(D0/2)^2*L; % Airbag initial volume
T0=20+273; % Initial tempreature (K)

P_atm=101e3;
DP=(P0-P_atm);

r_air=286; % Gas constant for air
gama=1.4;

%%Initial Conditions

uI=sqrt(2*g*h0);
aI=g;
xI=0;
VI=V_bag0;
PI=P0;
TI=T0;
wI=PI*VI/(r_air*TI);
roI=wI/VI;
AfpI=0;

mass_gas_cte1=P_atm*(1/(r_air*TI))^.5*(2*gama/(gama-1)*(PI/P_atm)^((gama-1)/gama))^.5;
mass_gas_cte2=PI*(1/(r_air*TI))^.5*(gama*(2/(gama+1))^((gama+1)/(gama-1)))^.5;

u(1)=uI; % Impact velocity
a(1)=aI;
x(1)=xI; % Initial position
V(1)=VI; % Initial airbag volume
P(1)=PI; % Initial airbag pressure
w(1)=wI; % Initial gas mass
ro(1)=roI; % Initial air density
Afp(1)=AfpI; % Initial contact area
valve=0;
first_bounce=0;
count=1;

impact_number=1;

PI(1)=PI;

```

```

roI(1)=roI;
x_base(1)=xI;
D(1)=D0;
VI(1)=VI;
for i=1:1:t_final/dt+1

    if (x(i)>(D-.01))
        display('Bottom Down')
        break;
    end

    x(i+1)=x(i)+u(i)*dt;
    if (x(i+1)-x_base(impact_number))<0
        Afp(i+1)=0;
        V(i+1)=V(i);
        P(i+1)=P_atm;
        w(i+1)=w(i);
    else
        Afp(i+1)=(pi*L*(x(i+1)-x_base(impact_number)));
        V(i+1)=VI(impact_number)-L*pi*((x(i+1)-x_base(impact_number))^2)/4;
    end
    Afp_avg=(Afp(i)+Afp(i+1))/2;
    dV=V(i)-V(i+1);
    if (x(i+1)-x_base(impact_number))>0
        P_old=P(i);
        w_old=w(i);
        ro_old=ro(i);

        ro_new(1)=w(i)/V(i+1);
        P_new(1)=PI(impact_number)*(ro_new(1)/roI(impact_number))^gama;

        if P_new(1)<P_atm
            P_new(1)=P_atm;
        end

        if P_new(1)>P_burst
            valve=1;
        end

        C_subsonic=A_th*P_atm*(1/(r_air*TI))^0.5*(2*gama/(gama-1)*(PI(impact_number)/P_atm)^((gama-1)/gama))^0.5;

        C_sonic=A_th*PI(impact_number)*(1/(r_air*TI))^0.5*(gama*(2/(gama+1))^((gama+1)/(gama-1)))^0.5;

        n=1;
        while(1)
            P_ratio=P_atm/P_new(n);
            C_d=-3.8399*P_ratio^6+9.4363*P_ratio^5-7.2326*P_ratio^4+1.6972*P_ratio^3-.2908*P_ratio^2-.013*P_ratio+.8426;

            dC_d=1/P_atm*((-3.8399)*(-6)*(P_ratio)^7+(9.4363)*(-5)*(P_ratio)^6+(-7.2326)*(-4)*(P_ratio)^5+(1.6972)*(-3)*(P_ratio)^4+(-.2908)*(-2)*(P_ratio)^3+(-.013)*(-1)*(P_ratio)^2);

            dwss=dt*C_d*A_th*mass_gas_ctel*((P_new(n)/P_atm)^((gama-1)/gama)-

```

```

1)^.5;

dws=dt*C_d*A_th*mass_gas_cte2*((P_new(n)/PI(impact_number))^( (gama
+1)/gama))^ .5;
Hss=((w_old-dwss)/(ro_old*V(i+1)));
Hs=((w_old-dws)/(ro_old*V(i+1)));
dHs=-
dt*(1/(ro_old*V(i+1)))*C_sonic*(dC_d*((P_new(n)/PI(impact_number))
^( (gama+1)/gama))^ .5+.5*C_d*((P_new(n)/PI(impact_number))^( (gama+1
)/gama))^ (-
.5)*(gama+1)/(gama*PI(impact_number))*(P_new(n)/PI(impact_number))
^(1/gama));
dHss=-
dt*(1/(ro_old*V(i+1)))*C_subsonic*(dC_d*((P_new(n)/P_atm)^( (gama-
1)/gama)-1)^ .5+.5*C_d*((P_new(n)/P_atm)^( (gama-1)/gama)-1)^ (-
.5)*( (gama-1)/gama*(P_new(n)/P_atm)^ (-1/gama)*1/P_atm));

Fs=P_old*(Hs)^gama-P_new(n);
Fss=P_old*(Hss)^gama-P_new(n);
dFs=P_old*gama*(Hs)^(gama-1)*dHs-1;
dFss=P_old*gama*(Hss)^(gama-1)*dHss-1;

if valve==1
    if ((P_ratio>.5283) && (P_ratio<1)) % subsonic
        P_new(n+1)=P_new(n)-Fss/dFss;
        if P_new(n+1)<P_atm
            P_new(n+1)=P_atm;
        end

        w(i+1)=w(i)-dwss;
    end
    if P_ratio<.5283 % sonic
        P_new(n+1)=P_new(n)-Fs/dFs;
        if P_new(n+1)<P_atm
            P_new(n+1)=P_atm;
        end

        w(i+1)=w(i)-dws;
    end
    if P_ratio==1
        if dV>0
            dwfree=ro_new(1)*dV;
        else
            dwfree=0;
        end

        w(i+1)=w(i)-dwfree;
    end
else
    P_new(n+1)=P_new(n);
    w(i+1)=w(i);
end
if (abs(P_new(n+1)-P_new(n))<100)
    P(i+1)=P_new(n);
    if (P(i+1)<P_atm)
        P(i+1)=P_atm;
    end
end

```

```

        break;
    end
    n=n+1;

end
end
P_avg=(P(i+1)+P(i))/2;
du=(g-Afp_avg*P_atm/m*((P_avg/P_atm)-1))*dt;
u(i+1)=u(i)+du;
u_avg=u(i)+du/2;
x(i+1)=x(i)+u_avg*dt;
if (x(i+1)-x_base(impact_number))<0
    Afp(i+1)=0;
    V(i+1)=V(i);
else
    Afp(i+1)=(L*pi*(x(i+1)-x_base(impact_number)));
    Afp_avg=(Afp(i)+Afp(i+1))/2;
    V(i+1)=VI(impact_number)-L*pi*((x(i+1)-x_base(impact_number))^2)/4;
end
ro(i+1)=w(i+1)/V(i+1);
a(i+1)=(g-Afp_avg*P_atm/m*((P_avg/P_atm)-1));

if (abs(-a(i+1)+g)<.1)
    if (a(i+1)-a(i))>.001
        u_fb(impact_number)=u(i+1);
        t_fb(impact_number)=(i-1)*dt;
        x_fb=x(i+1);

        if u_fb(impact_number)<0
            impact_number=impact_number+1;
            x_base(impact_number)=x_fb;
            PI(impact_number)=P_atm;
            VI(impact_number)=V(i+1);
            roI(impact_number)=ro(i+1);
            D(impact_number)=D(impact_number-1)-x_base(impact_number);
            first_bounce=1;
        end
    end
    hh(count)=i;
    count=count+1;

end

end

t=0:dt:(i-1)*dt;
if i==t_final/dt+1
    P(i+1)='';
    u(i+1)='';
    x(i+1)='';
    a(i+1)='';
    V(i+1)='';
    w(i+1)='';
    ro(i+1)='';
    Afp(i+1)='';
end

if first_bounce==0

```



```
        display('No Bounce')
end

plot(t, (-a/g), 'k')

kd=(P-P_atm).*Afp./x;      % Dynamic stiffness
```

## **Appendix C.**

### **Further Refinements to Drop-test Apparatus**

Some of modifications that can be applied to experimental methodology conducted for conventional airbag for enhanced future study are listed as following:

- The attachment of the headform to the rail, although guarantees single degree of freedom motion, as assumed during model development, however it imposes additional friction between carriage and rail during the impact as the moments acting on the carriage during the impact increases the normal force and hence the friction. This problem can be resolved by the improved test campaign configuration where the headform is disattached from the carriage a bit atop the airbag by deactivating an electromagnet in order to experience a free fall motion.
- Opting for other venting mechanisms such as passive relief valves, rather than active solenoid valve, seems better fit in this approach. In fact, choice of pressure relief valve provides the opportunity for multiple energy-release stages which aids in maintaining the ideal pressure level for longer period of impact. Besides, being a passive element as well as having negligible response time as opposed to solenoid valve, it adds to the feasibility of venting implementation to human airbags.
- Development of more accurate shape function for airbag geometry approximation during the impact, seems essential for improved simulations as the system response, reveals high sensitivity to the airbag sizing and the manner it is changed during the impact. Furthermore, choice of smaller airbag for impact applications in the range of human fall is of more rationale as the smaller airbag can maintain the specific higher pressure inside for longer time.
- Optimum venting area obtained for optimal HIC, can be implemented into the airbag as a series of smaller holes with same overall venting area in order to explore any possible damping contribution in more realizable energy management during the impact.